Plasmon Enhanced Photocurrent Generation and Water Splitting on Photoanode of Gold Nanoparticles Loaded Gallium Oxide

Thesis by

Yaguang Wang

In Partial Fulfillment of the Requirements

For the Degree of

Doctor of Philosophy

GRADUATE SCHOOL OF INFORMATION SCIENCE AND TECHNOLOGY

HOKKAIDO UNIVERSITY

SAPPORO, JAPAN

2023

Table of Contents

Acknowledgement

Upon finishing this thesis, it's my great honor to take this opportunity to express my special thanks to all those who have supported me sincere assistance during the past years.

My deepest gratitude goes first and foremost to Professor Hiroaki Misawa, my supervisor, for his patient guidance to the research work and paper writing in my doctoral course period. He offered me the position to pursue the Ph.D. degree in his team that owns a very high research level. Importantly, he taught me what real research and science are during the doctoral period. Thanks to the topics full of challenges and novelty, I learned how to be a real researcher. I would like to thank Prof. Kosei Ueno for giving me a lot of suggestions so that I could grasp the basic knowledge of my research topics when I was new here. My sincere thanks also go to Prof. Tomoya Oshikiri who supported me with a lot of assistance in the research discussion and paper revising. He was always patient when I met some problems and ask him for help on the experiment. Furthermore, I would like to express my heartfelt gratitude to Prof. Quan Sun. Without your help in daily life, I would not adapt to the life in Japan so smoothly and quickly. Also, I owe my thanks to Prof. Xu Shi who gave me a lot of advice and shared knowledge on the experiment that was beneficial to resolving the questions that confused me. Thank you very much for your patience during the discussion and analysis of the experiment results.

I also express my appreciation to previous members in our laboratory, Guo-san, Nakamura-san, Furuya-san, Jo-san, Shimizu-san, Yamada-san, Onishi-san, Takakura-san and Y Cao-san who assisted me in the daily life and experiment. Especially, Takakura-san as my supporter instructed and helped me a lot in the first month when I came to Japan. I am also deeply indebted to all the current members in this team, Liu-san, Suganami-san, Araki-san and Ishihara-san for their direct help to

me in past years. Besides, my heartfelt thanks would go to Hattori-san for his encouragement. It was a really nice and happy memory with him, although he has been here for only one year in our team. I wish to extend my deep gratitude to Fan-san, Zang-san and En Cao-san for the support with each other at the moment when I was under high pressure. The special thanks would go to En Cao-san for your comfort and understanding when I was at the rocket bottom. I will remember the life in Hokkaido with you when we enjoyed the game, traveling and other nice things together in Japan.

Additionally, I owe a sincere gratitude to all the friends in Japan and China. Your support really gave me the confidence and courage so that I could overcome the difficulties met in past years.

Finally, I want to say thank you to my family, my warm parents. Your concern and support, endless and selfless love are the faith and strength for me to continue pursuing my goal and future.

Abstract

Gallium (III) oxide (Ga_2O_3) is a wide bandgap semiconductor (~4.8 eV) with a very negative conduction band (CB) potential, making it applicable not only for the reduction of water but also for the reduction of CO_2 and other substances requiring negative reduction potentials. However, the large bandgap of Ga_2O_3 has made it difficult to use visible light. To resolve this problem, in this thesis, the photocurrent generation and water splitting under the visible irradiation using a plasmonic photoanode based on gold nanoparticles (Au-NPs)/Ga_2O_3 were mainly studied.

To harvest visible light, Au-NPs with different sizes were loaded on each single crystal Ga_2O_3 (SC-Ga_2O_3) substrate by annealing of deposited Au-films on the substrates with different thicknesses. As a result, generation of photocurrent by visible light irradiation was observed in Au-NPs loaded SC-Ga_2O_3 substrate as the photoanode due to hot carrier generation based on localized surface plasmon resonance (LSPR) of Au-NPs. In addition, the 15 nm-sized Au-NPs loaded SC-Ga_2O_3 substrate exhibited the largest incident photon to current conversion efficiency (IPCE) (Chapter 2).

To further enhance the IPCE of Au-NPs/SC-Ga_2O_3 as a photoanode, an attempt was made to deposit a thin TiO_2 layer at the Au-NPs/SC-Ga_2O_3 interface because it is known that TiO_2 is effective in trapping hot holes. First, it was found that depositing a TiO_2 thin layer between the Au-NPs and the Ga_2O_3 substrate suppresses hot electron injection from the Au-NPs to Ga_2O_3, resulting in a decrease in IPCE. On the other hand, when the Au-NPs on the Ga_2O_3 substrate were partially embedded by TiO_2, the hole-trapping ability was enhanced and IPCE was found to increase obviously. Furthermore, the thickness dependence of the TiO_2 layer on IPCE was also revealed

that 2 nm TiO_2-modified Au-NPs/SC-Ga_2O_3 exhibited the highest IPCE, 1.5 times higher than that of Au-NPs/SC-Ga_2O_3 (Chapter 3).

To further improve the light harvesting and water oxidation reaction efficiency, a structure of TiO_2/Au-NPs/Ga_2O_3/TiN/Au-film (TAGA) to achieve modal strong coupling between the LSPR of Au-NPs and the Fabry-Pérot nanocavity was employed. In the TAGA, TiN acted as a protection layer for Au-film and that Ga_2O_3 film, which exhibited excellent semiconductor properties, was deposited on the TiN/Au-film reflective mirror. The TiN/Au-film exhibited satisfactory electrochemical properties and served as a reflective mirror for the nanocavity. The modal strong coupling was constructed by overlapping the resonance wavelength of the nanocavity with the LSPR wavelength of the Au-NPs partially embedded in the TiO_2 layer. Under the modal strong coupling condition, the optical absorption increased dramatically and the IPCE was enhanced. In this structure, the Au-NPs partially embedded in the TiO_2 layer showed an important role in enhancing the strength of the modal strong coupling and hole-trapping ability. The use of the TAGA with very negative CB potential led to successful water splitting at zero bias potential under visible light irradiation (Chapter 4).

In summary, it was demonstrated that hot electrons generated by the LSPR of Au-NPs were injected into the CB of Ga_2O_3, and hot holes could further induce water oxidation, generating a photocurrent under visible irradiation. In addition, partial embedding of Au-NPs in a TiO_2 layer, which had a higher hole-capturing ability than Ga_2O_3, improved the efficiency of charge separation of hot carriers generated in the Au-NPs, resulting in improved IPCE. Furthermore, it was found that modal strong coupling between the LSPR of Au-NPs and the nanocavity was expressed in the TAGA photoanodes improved their visible light-harvesting ability and effectively

increased IPCE. Finally, visible light-driven water splitting at zero bias potential was also achieved using the TAGA photoanodes.

Chapter 1

Introduction

1.1 Background

With the development of modern society and population explosion, energy resource consumption is dramatically increasing recent decades, especially since globalization all over the world.[1] Although globalization has a huge contribution to economic development and improvement of living quality,[2] on the other hand, the world would face an energy crisis in the future due to the non-renewable property of fossil fuel and the steady growth of energy consumption.[3-4] Furthermore, the heavy use of fossil fuels leads to severe climate risk and environmental pollution, such as the global warming problem originated from massive carbon emissions.[5-7] During the past 130 years, the global temperature has been rose by 0.85 ^{o}C (Figure 1.1), which would cause many terrible problems.[8-9] Therefore, lots of countries have focused on the way to resolve this problem, and many strategies have been applied to prevent the situation worse, such as limiting carbon emission and searching for renewable and clean energy resource.[10-11]

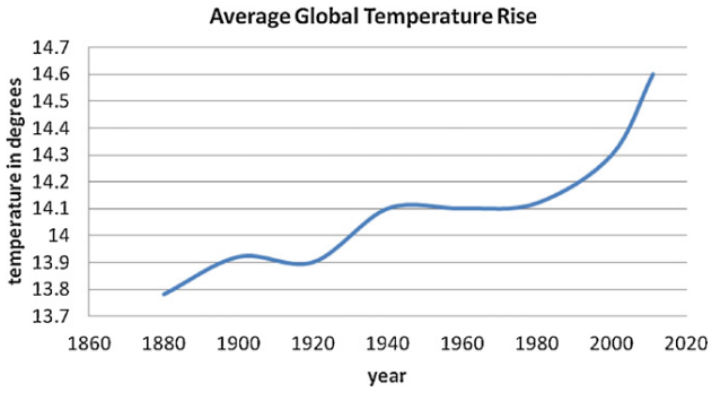

Figure 1.1 The graph of average global temperature rise.[9]

Up to now, solar energy, nuclear energy and wind energy have been widely investigated as renewable or clean energy.[12-14] Although nuclear energy owns a very

high energy density, nuclear leakage is a non-negligible risk during its application.[15] It is understandable the disadvantages of strict location demand and non-consistent energy generation also limit the wide application of wind energy in the world. Compared with the other two kinds of new energy sources, solar energy is considered more abundant, eco-friendly and promising in the future.[16] As we know, solar energy is almost exhaustible with various forms (light, heat) when it reaches our planet. The earth could intercept around 1.8×10^{14} kW from the energy emitted by the sun (3.8×10^{23} kW) even if it undergoes the loss from the scattering and reflection.[17] Most importantly, unlike nuclear energy, solar energy is much cleaner and safer. Photovoltaic (PV) is one of the main applications among the solar energy conversion fields.[18] Si-based solar cell still domains the global PV market,[19-20] with a record energy conversion efficiency of 26.7% for mono-crystallinity silicon solar cells.[21] Meanwhile, in the industrial area, large-area Si solar cell with an efficiency of 24.5% has been widely applied.[22] On the other hand, many research teams and companies also pay more attention to inorganic thin film solar cells, such as Cu-based thin film solar cells (CIGS and CZTS) due to their abundant elements, direct bandgap, high efficiency (26.4%) and non-toxic properties.[23-24] Perovskite is a new kind of absorption material for solar cells, which owns excellent advantages including simple fabrication, cost-effective and high efficiency.[25] It will show a huge prospect in the solar energy application if the perovskite could overcome the instability in the air due to the water.[26]

On the other hand, photocatalysis is another mainly investigated topic that the mechanism is the transfer from solar energy to chemical energy. It is expected to achieve artificial photosynthesis using solar energy to simulate the series of reactions occurring in plants, such as the electrochemical CO_2 reduction to fuels and chemicals (CO, CH_4, HCOOH, etc.) that could efficiently release the CO_2 emission problem.[27-28] H_2 evolution from water splitting is also an extremely important application in photocatalysis.[29] H_2 is considered as a promising green energy source in the future which could take place of traditional fossil fuels based on the advantages of zero CO_2

and other pollutants emission after combustion and very simple raw material of water.[30]

1.2 Ga_2O_3 Properties and Application

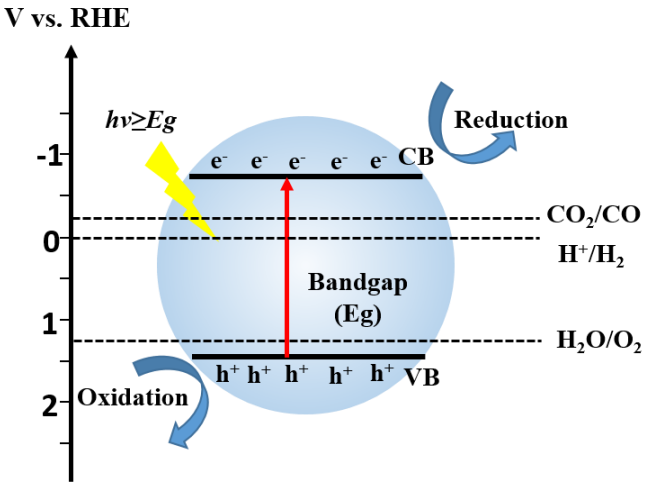

Figure 1.2 Schematics of photocatalytic water splitting and CO_2 reduction in semiconductors.[32]

In the case of water splitting, various technologies and materials have been developed to achieve hydrogen and oxygen evolution.[31] To achieve the overall water splitting, the bottom of the conduction band (CB) of the semiconductor should be much more negative than the reduction potential of H^+/H_2, while the top valence band (VB) potential should be more positive than the oxidation potential of H_2O/O_2.[32] The photon energy larger than the bandgap of semiconductor could excite the electrons and holes taking parting in reduction and oxidation reactions on the surface of semiconductors or external circuit as shown in Figure 1.2. However, in the case of CO_2 reduction, compared with H_2 evolution, more negative reduction potential is required to convert CO_2 into CO and CH_4. Besides the requirement of energy band position, thermal and chemical stability are also vital factors that should be considered. Although some semiconductors fit the demand on band energy and show good properties in photo energy conversion, such as CdS, the unstable properties in oxidation reactions resulting in degradation limit their application.[33]

Recently, metal oxide semiconductors (MOSs) with wide bandgaps have drawn much attention in the photocatalysis field which showed suitable band structure and excellent chemical stability, such as TiO_2.[34] TiO_2 with large bandgap (about 3.2 eV) has been widely studied in water splitting since the Honda-Fujishima effect was discovered in 1972.[35] Despite TiO_2 with various structures has drawn much attention and been reported in water splitting because of its low cost, safety and high chemical stability in aqueous condition.[36] However, the CB potential of TiO_2 is very close to the H_2/H^+,[37] making it difficult to achieve the CO_2 reduction and other substances reduction that required more negative reduction potential. In addition, to achieve more efficient water splitting using TiO_2, a bias potential was always required. As a result, researchers have turned their directions to some semiconductors which own much more negative CB potential. Ga_2O_3 is reported to be one kind of semiconductor whose CB potential is about -1.0 to -1.5 V vs. RHE.[38-39] As a result, this band structure indicates the photo-excited electrons own strong reduction ability that makes the water splitting at zero bias possible and show a large prospect in CO_2 reduction.

1.2.1 Overview of the fundamental properties of Ga_2O_3

Ga_2O_3 is a natural ultra-wide bandgap semiconductor with a direct bandgap of 4.5-5.0 eV.[40-41] As a deep ultraviolet transparent conductive oxide, Ga_2O_3 owns a high breakdown electric field and decent electron mobility.[42-43] The dielectric constant of Ga_2O_3 is 10, which is suitable for power device figure of merit.[44] The Ga_2O_3 also shows good thermal and chemical stability which could stand some extreme conditions including the high temperature and radiation.[45-46] Based on the advantages mentioned above, recently it has become a hot topic in power electronics, optoelectronics and sensing areas, such as field-effect transistors (FETs), Schottky barrier diodes, UV photodetectors and gas sensors.[47-50] As shown in Figure 1.3, there are mainly six kinds of crystal structures for Ga_2O_3, α-Ga_2O_3, β-Ga_2O_3, γ-Ga_2O_3, δ-Ga_2O_3, ε-Ga_2O_3 and κ-Ga_2O_3.[51]

Lattice parameters of Ga_2O_3 polymorphs.

Polymorph	System	Space group	Lattice parameters
α	Hexagonal	$R\bar{3}c$	$a = b = 4.98$ Å, $c = 13.43$ Å, $\alpha = \beta = 90°$, $\gamma = 120°$
β	Monoclinic	$C2/m$	$a = 12.23$ Å, $b = 3.04$ Å, $c = 5.80$ Å, $\alpha = \gamma = 90°$, $\beta = 103.8°$
γ	Cubic	$Fd\bar{3}m$	$a = b = c = 8.24$ Å, $\alpha = \beta = \gamma = 90°$
δ	Cubic	$Ia3$	$a = b = c = 9.52$ Å, $\alpha = \beta = \gamma = 90°$
ε	Hexagonal	$P63mc$	$a = b = 2.90$ Å, $c = 9.26$ Å, $\alpha = \beta = 90°$, $\gamma = 120°$
κ	Orthorhombic	$Pna2_1$	$a = 5.05$ Å, $b = 8.70$ Å, $c = 9.28$ Å, $\alpha = \beta = \gamma = 90°$

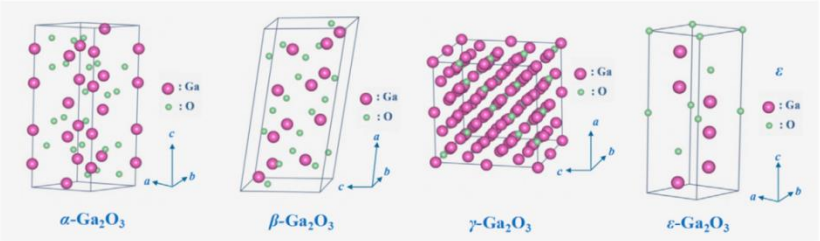

Figure 1.3 Crystal structures of polymorphs of Ga_2O_3.[51]

α-Ga_2O_3 is a metastable phase with an R3c group.[52] The function engineering by alloying α-Ga_2O_3 with transition-metal oxides such as Cr_2O_3 and Al_2O_3 shows great potential in magnetization hysteresis due to the same crystal structure. α-Ga_2O_3 shows a better potential as a candidate in power electronics than β-Ga_2O_3.[53] Several methods including mist chemical vapor deposition, hydrothermal method and laser molecular beam epitaxy on the substrate of sapphire (α-Al_2O_3) have been studied to synthesis α-Ga_2O_3.

γ-Ga_2O and ε-Ga_2O_3 are also the metastable phases which own space group of Fd3m (cubic spinel-type structure) and P63mc, respectively.[54] Due to the room temperature ferromagnetism in Mn-doped γ-Ga_2O_3, it was expected to be promising in spintronic material.[55] In the case of ε-Ga_2O_3, some teams have reported that high-density 2DEG could be obtained by ε-Ga_2O_3 as conducting channels in FETs.[56]

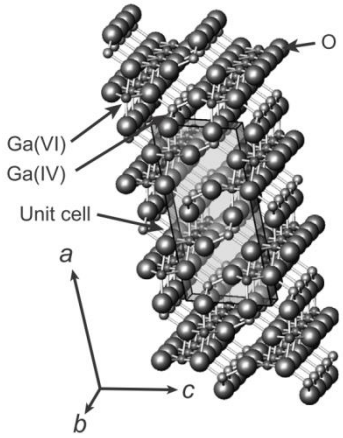

Figure 1.4 The crystal structure of polymorphs of β-Ga_2O_3.[57]

As the most chemically and thermally stable phase, β-Ga_2O_3 is the most widely studied structure.[58] As the formation energy is much lower than the other structures, some metastable phases could transform to β-Ga_2O_3 under high temperatures.[59] As shown in Figure 1.4, it owns a monoclinic system in a space group of C2/m whose lattice parameter of a, b, c is 1.22 nm, 0.3 nm and 0.58 nm with the β value of 103.8º, respectively.[57] Ga (I) and Ga (II) occupy two crystallographically inequivalent positions in the unit cell, which are the tetrahedral geometry and octahedral.[60] For oxygen ions, there are three crystallographically different positions in distorted cubic packing.

Similar to other metal oxides (d^0/d^{10} metal cations) that the top of the VB is made of the O 2p orbitals at the position of ca. +3 V vs. NHE, the β-Ga_2O_3 shows ultra-wide bandgap (around 4.9 eV) due to its negative CB potential.[60-61] The large bandgap makes it suitable in the application of solar-blind detectors because the absorption edge is from around 250 to 280 nm and extremely high transmittance.[62] Moreover, the large bandgap means a larger redox potential compared with TiO_2, so high reduction and oxidation ability of photogenerated carriers are expected.

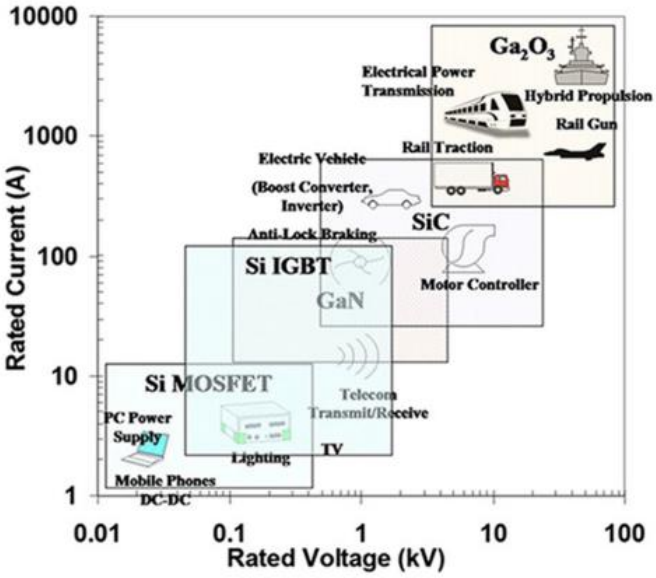

Figure 1.5 Applications of Si, SiC, GaN, and Ga_2O_3 in power electronic.[63]

Regarding the electric properties, this ultra-high bandgap makes it promising in power electronics compared to the GaN and SiC which are considered as the next-generation semiconductors as a result of the high critical breakdown electrical field shown in Figure 1.5.[63] The breakdown E of β-Ga_2O_3 is about 8 MV/cm which is nearly twice larger than that of GaN and SiC so that the size of the power devices could be easily decreased while improving the integration of modules.[42] The mobility was reported to be 200 $cm^2\ V^{-1}\ s^{-1}$.[64] Although the conductivity was limited by its large bandgap similar to other transparent semiconductors, some teams have reported that a thinner drift layer in high-frequency equipment using β-Ga_2O_3 could decrease parasitic capacitance because the wide bandgap compensates the low mobility.[65] It has been reported that the oxygen vacancies played a key role in the electric conductivity forming the free electrons during bulk β-Ga_2O_3.[66] The free electrons originate from the oxygen vacancies leading to the n-type conductivity.[67] Forming p-type β-Ga_2O_3 is very difficult because of the high energy required to active the acceptor impurities due to the large distance between acceptor levels and VB.[68] In addition, self-compensation produced by the donor impurities will also have a negative effect on the acceptor.[69] Although β-Ga_2O_3 has such advantages mentioned above, some disadvantages also

limit its application in some fields, such as the low thermal conductivity of 0.1 to 0.3 W cm^{-1} K^{-1}.[70]

The melt growth method has been applied to the fabrication of uniform bulk Ga_2O_3 with a large area, which is more cost-effective than that of some other wide bandgap semiconductor.[71] In the case of film deposition for the application in photocatalysis, photodetector or some other power electronics devices, pulse laser deposition (PLD), atomic layer deposition (ALD) and molecular beam epitaxy (MBE) are widely employed.[72-74] The applications using Ga_2O_3 will be introduced in the following part.

1.2.2 Application of Ga_2O_3

a. Gas sensors

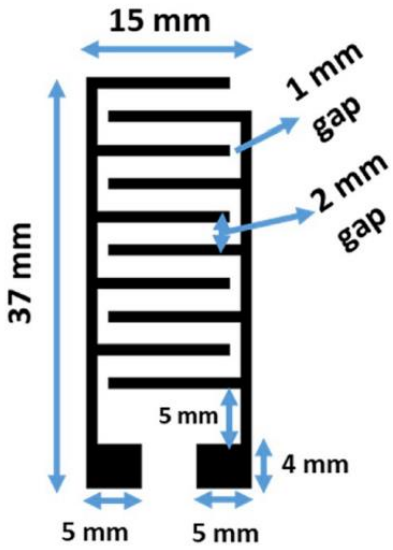

Figure 1.6 Ammonia sensing using β-Ga_2O_3 with IDE pattern.[75]

NH_3 is another kind of frequently used gas in industrial production and research field which is poisonous to people health and the environment.[76] Thus, monitoring the NH_3 concentration in the air becomes more important in recent years. Compared with some other materials used in the NH_3 detection, such as ZnO and SnO_2, β-Ga_2O_3 showed some unique properties mentioned above making it attractive in the NH_3

detection. Rekha Pilliadugula and N. Gopala Krishnan reported an NH_3 sensor fabricated by drop-casting β-Ga_2O_3 powder on glass. The substrate has been printed by the inter digitated electrode pattern (IDE) of silver (Ag) ink before the β-Ga_2O_3 casting as shown in Figure 1.6.[75] This structure showed favorable for sensing activities including the improved sensing responses and sensitivities at room temperature.

b. Water splitting

Artificial photosynthesis is an effective strategy to overcome the energy crisis and environmental problems, such as the renewable energy production and global warming originating from CO_2 emission. Besides the applications in power electronics and gas sensors, Ga_2O_3 also exhibit huge prospect in the artificial photosynthesis process including the H_2 evolution from water splitting, CO_2 conversion to CO, CH_4, HCOOH or some other hydrocarbons because of its negative CB potential which owns superior reduction ability in photoelectrochemical reactions.[77] On the other hand, the advantage of the high oxidation potential of the VB located at -7.75 eV vs. vacuum energy level makes it suitable in the photodecomposition and photodegradation of some organic pollutants.[38]

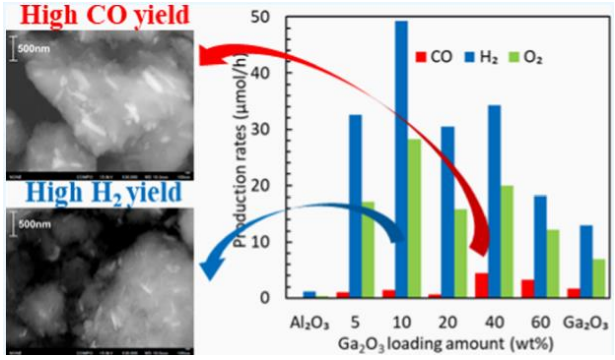

Figure 1.7 Water slitting and CO_2 reduction using Ga_2O_3 supported on Al_2O_3.[78]

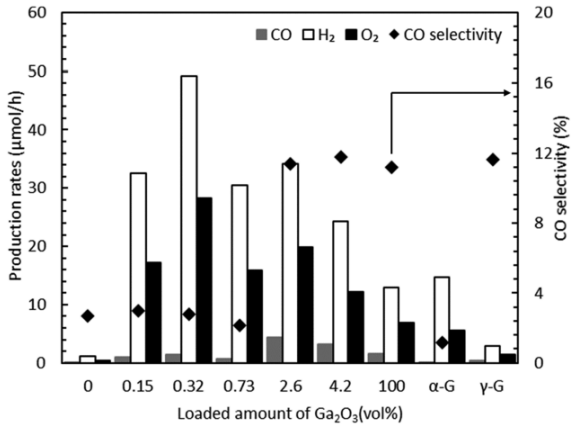

Figure 1.8 Production rate of water splitting and CO_2 reduction using Ga_2O_3/Al_2O_3.[78]

Tomoko Yoshida group achieved the CO_2 reduction to CO and water splitting using the structure of Ga_2O_3 particles on Al_2O_3 without any co-catalyst under UV light.[78] In this study, the impregnation method was applied to fabricate the Ga_2O_3 particles on Al_2O_3 by adding $Ga(NO_3)_3 \cdot 8H_2O$ and γ-Al_2O_3 into water following a calcination process. This structure showed a high performance in the water splitting and CO_2 reduction. The activity for water splitting and CO_2 reduction could be controlled by changing the amount of Ga_2O_3 loaded on Al_2O_3. It was found that in the case of lower Ga_2O_3 loaded sample, water splitting was preferred on the sites where nanometer-sized Ga_2O_3 rods were dispersed. CO_2 reduction was preferred to occur on sub-micrometer-sized Ga_2O_3 particles in high-load amount cases. In this research, there were no obvious effects of Al_2O_3 on the photocatalysis performance except for supporting the Ga_2O_3.

c. Benzene degradation

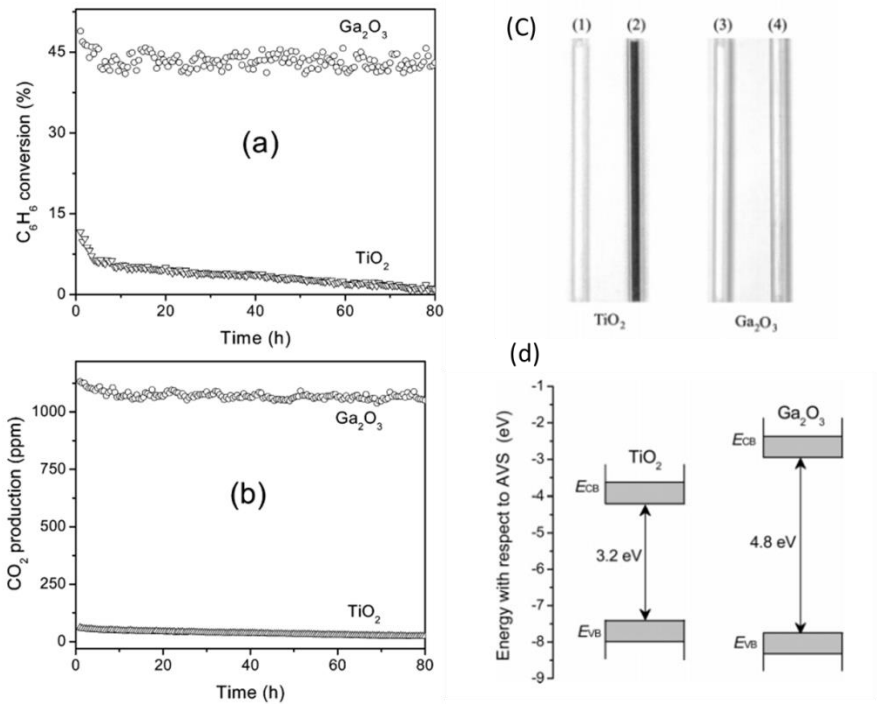

Figure 1.9 (a) The benzene conversion on Ga_2O_3; (b) CO_2 amount generated in the decomposition of benzene; (c) samples of TiO_2 and Ga_2O_3 before and after reaction; (d) energy level of TiO_2 and Ga_2O_3 vs. vacuum scale.[38]

Benzene is a common raw material in organic chemical synthesis which could be used to produce rubber and fiber.[79] However, benzene is volatile and toxic to people's body. The blood cells could be killed when people were exposed to conditions with a very low concentration of benzene. As a result, removing the benzene from the air effectively is full of challenges. Although the photodecomposition of benzene to CO_2 and H_2O could be achieved by TiO_2, the accumulation of the intermediate will limit this function. In 2006, high reactivity of degradation of benzene by β-Ga_2O_3 with porous structure in the air was reported by Xianzhi Fu *et al*. In this case, no noble metals were loaded on the β-Ga_2O_3. The pure Ga_2O_3 showed excellent performance on the benzene conversion with an efficiency of 42% much higher than that of Pt loaded TiO_2 under UV light shown in Figure 1.9. In addition, the pure β-Ga_2O_3 catalyst kept high stability even after the 80 h experiment.

d. CO_2 reduction

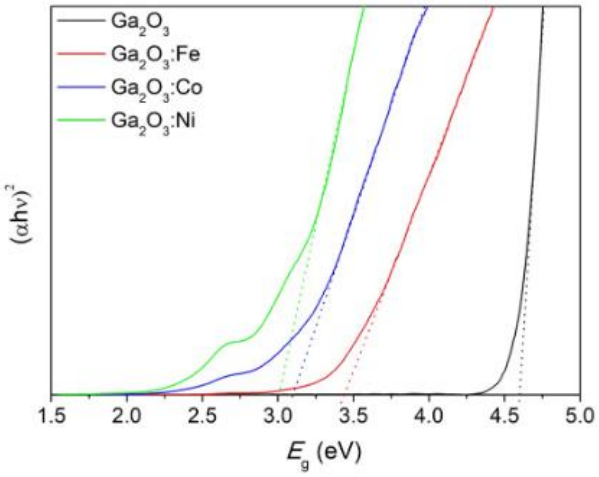

Figure 1.10 Bandgap of bare and transition metal doped Ga_2O_3.[80]

Although Ga_2O_3 has been widely applied in many fields, the large bandgap limits the use of visible light which accounts for most energy in the full solar spectrum. Doping is an effective method to adjust the bandgap so that it could fulfill various requirements for applications.[81] Yang tea successfully achieved the CO_2 reduction under visible irradiation by doping different kinds of transition metal in Ga_2O_3.[80] After doping the Fe^{3+}, Co^{2+} and Ni^{2+}, the optical bandgap of Ga_2O_3 was changed in a range from 3.0 to 3.5 eV which was much smaller than the intrinsic bandgap of Ga_2O_3. As a result, the CO_2 reduction to CO and the water reduction to H_2 under visible light were obtained with an evolution rate of 24.6 μmol/h and 13.1 μmol/h, respectively.

However, the doping method changes the band structure of Ga_2O_3, the CB shifts to a positive position weakening the advantage of high CB reduction potential of Ga_2O_3. Some other methods should be applied to achieve the visible response of Ga_2O_3 without changing its CB or VB position so that it could keep the high redox ability for photocatalysis. Recent years, many researches have focused on the plasmon effect of noble metal nanoparticles (NPs) in the visible light driven photo energy conversion field.[82-83] The basic properties and applications based on the plasmonic system would be introduced in the following section.

1.3 Localized Surface Plasmon Resonance

1.3.1 Basic knowledge of localized surface plasmon resonance

When the electromagnetic fields are coupled to oscillations of metal's electron plasma, electromagnetic excitations will occur propagating in a direction parallel to the interface of dielectric and metal which was called the surface plasmon polaritons (SPPs).[84] In the 1960s, Kretschmann et.al first demonstrated the optical excitations of surface plasmon through the attenuated total reflection.[85] When the frequency of incident light coincides with the electrons oscillating frequency, the resonant oscillation of conduction electrons occurred which was called the surface plasmon resonances (SPRs).[86] Plasmon here means the quanta of this coherent charge oscillation during the interaction between light and conduction electrons.[87] When the metal size was decreased to much smaller than the incident light wavelength, such as the nanometer scale, a dipole moment inside the particles would be induced by the incoming light.[88] When their frequencies match with each other, the resonance would arise and result in the large field amplification in the inner and outside near-field of metal particles as shown in Figure 1.11.[89] This localized resonance was called the localized surface plasmon resonance (LSPR).

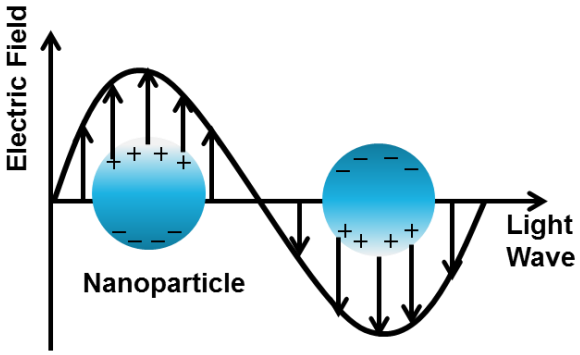

Figure 1.11 LSPR of metal nanoparticles.

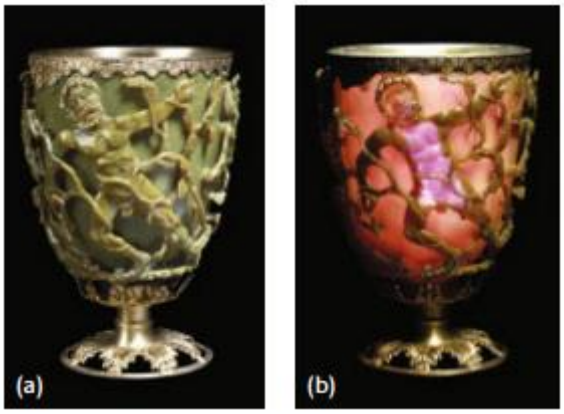

Figure 1.12 Ancient Roman Lycurgus cup.[90]

Although the mechanism of LSPR is clear until modern scientific study, ancient people have applied the LSPR effect to some art creations and daily life such as the Lycurgus cup by the Romans nearly 1600 years ago.[90] In this dichroic material, the colors are different when it was observed through the reflection and transmission shown in the glass picture in Figure 1.12. The LSPR effect could be described by the application of a simple model of quasi-static approximation as shown in the following Figure 1.13.[91]

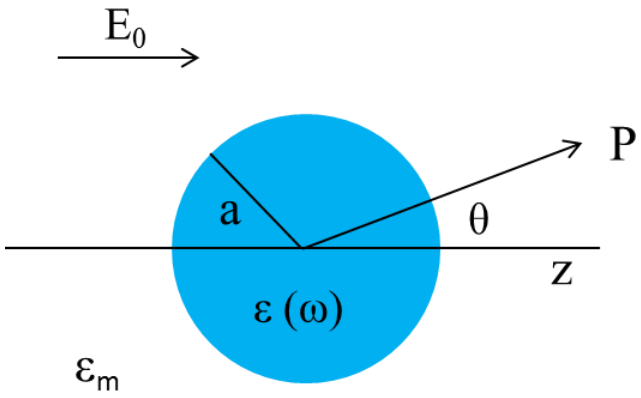

Figure 1.13 Illustration of metal sphere model into electrostatics field.

In this model, ε (ω) is the dielectric function of the metal sphere, a is the radius of the homogeneous sphere, P_l (cos θ) represents the Legendre Polynomials of an order of *l*, the angle between vector **r** and the z-axis is θ. According to the electrostatics

approach, the solution for Laplace equation to $\nabla^2 \Phi = 0$ could be written as the following:

$$\Phi(r,\theta) = \sum_{l=0}^{\infty}[A_l r^l + B_l r^{-(l+1)}] P_l(\cos\theta)$$

According to this solution equation, we could obtain the polarizability of:

$$\alpha = 4\pi a^3 \frac{\varepsilon-\varepsilon_m}{\varepsilon+2\varepsilon_m}$$

As a result, we could get the Frohlich condition under which the polarizability would have a resonant enhancement as following:

$$\mathrm{Re}[\varepsilon(\omega)] = -2\varepsilon_m$$

Under the condition, in the form of an electric dipole, metal nanoparticles would have a strong effect on incident light absorbing and scattering. It could be found that the LSPR frequency shows a negative relation with the dielectric constant of the surrounding medium. Based on this rule, we could design the plasmonic system according to the LSPR frequency we desire. Notably, this dipole mode is only strictly valid for extremely small particles. In 1908, Mie's theory based on the rigorous electrodynamic approach was developed to describe the case of larger size particles.[92]

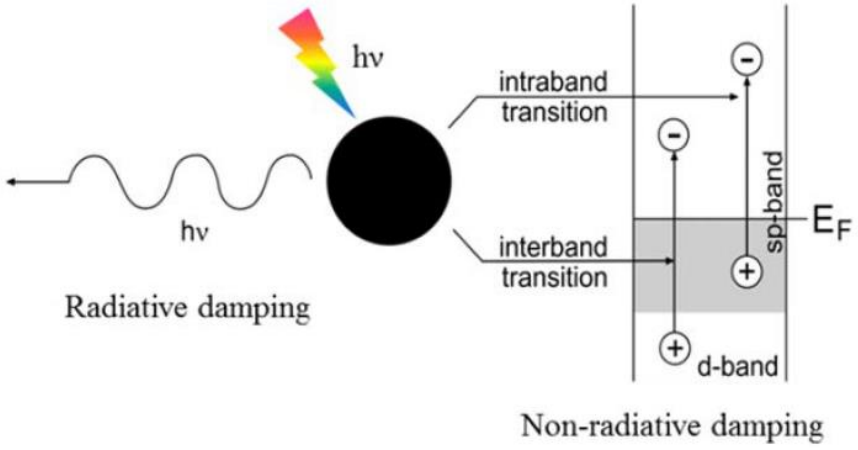

Figure 1.14 Schematic of two decay processes for LSPR energy.[89]

There are total two damping processes for LSPR energy of noble metal

nanoparticles: radiative and non-radiative processes as depicted by Figure 1.14.[89] For larger particles, the damping process is mainly dominated by radiative decay which is also called scattering. This is also the main reason for the dipole resonance weakening while increasing the particle size.[93] During the radiative decay, the particles plasmon directly transform into photons. For smaller particles, the main non-radiative damping process as a result of absorption would generate the carriers of electron/hole pairs via the Landan damping which is a pure quantum process.[94] The plasmon quantum could be transferred to hot carriers in a timescale from 1 to 100 fs.[95] During the absorption process, the single-electron states would be first excited by the surface plasmons. Then, there would be two channels for the electrons excitations: intraband transition with conduction band and the transition from d band to sp band which is called the interband excitation as illustrated in the schematic. These electrons could be excited above the fermi level as the hot carriers.[96] The non-radiative decay mechanism is a very important topic during the application of LSPR of noble metal-NPs in various optical and photoelectric fields.[97]

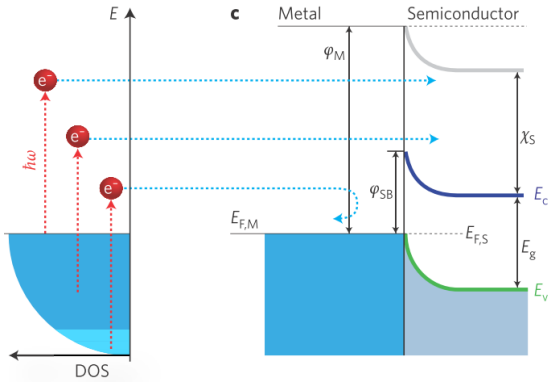

Figure 1.15 Hot electrons generation and injection into semiconductors by the Schottky barrier at the interface.[98]

To form the photo-generated circuit current, the whole process should be the carrier generation, transfer/separation and regeneration.[99] The Schottky barrier formed at the interface between metal nanoparticles and semiconductors which own a suitable work function is an effective strategy to capture the electron owning energy larger than the

barrier height. However, the hot electrons just generate in a time scale smaller than 100 fs through the e-e scattering process.[100] To achieve the electrons transfer in such a short time efficiently based on the electrons and electrons-accepting levels coupling, a large amount of states in CB is required. As shown in Figure 1.15,[98] the barrier could achieve the separation and injection of the hot carrier decreasing the recombination between electrons and holes.[101]

1.3.2 Fabrication of plasmonic particles and structures

Up to now, various methods have been studied to obtain the noble metal-NPs or nanostructures with different sizes and shapes including chemical synthesis and physical preparation. Here, the following section will introduce some classic methods for the fabrication of metal NPs and nanostructures.

a. Reduction of $HAuCl_4$

Au-NPs with small sizes have attracted much interest in various applications due to their excellent optical properties originating from LSPR. However, the fabrication of Au-NPs with a diameter smaller than 5 nm still faces lots of difficulties due to the aggregate phenomenon resulting from Van Der Waals interaction between very small particles.[102]

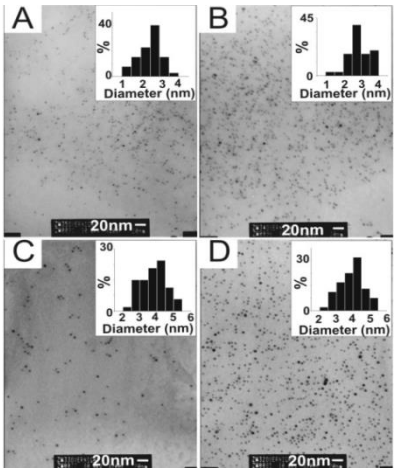

Figure 1.16 TEM of ATP-capped Au-NPs with different ATP molar ratios.[103]

To overcome the aggregation, capping ligand is a good way to protect the crystals

and generate small size particles. However, most of these capping ligands belong to organics which are not friendly to the environment and physically health. The synthesis routes to fabricate water soluble Au-NPs with the capping ligand of nucleotide were developed by M. A. Brook. The size could be controlled in a diameter range from 2 to 5 nm. In this study, $HAuCl_4$ was mixed with adenosine 5'-triphosphate as the gold source following by the addition of $NaBH_4$ solution so that $HAuCl_4$ was reduced to Au-NPs. According to the TEM, tunable Au-NPs size from 2 to 5 nm without serious aggregation was successfully obtained using this method as shown in Figure 1.16.

b. Seeded growth method

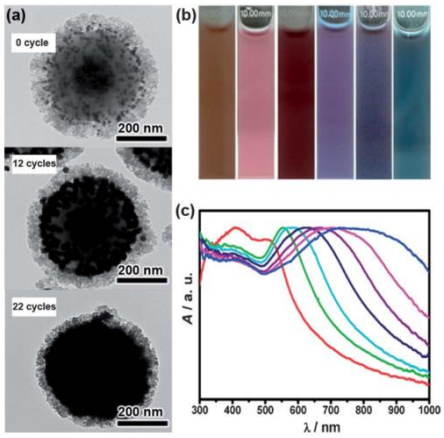

Figure 1.17 Seeded growth of Au nanoshell with sandwiched structure.[104]

Seeded growth was first proposed by Murphy *et al* to synthesize Au nanospheres with well-controlled size.[105] It is very easy to control the growth steps compared with the typical one-step method so that seed nucleation could be sustained. Also, the particle size could be changed in a wide range. Importantly, continuous growth was achieved by this growth method. Based on these advantages, Gao *et.al* reported the successful fabrication of Au nanoshell with sandwiched structure.[104] The Au salt was added into the reaction solution slowly to grow the Au-NPs by self-nucleation. Then the Au-NPs were sandwiched by a silica nanosphere and silica layer. These structures fabricated by seeded growth showed good tunable optical properties in a spectrum

range from visible to infrared light as shown in Figure 1.17.

c. High temperature annealing

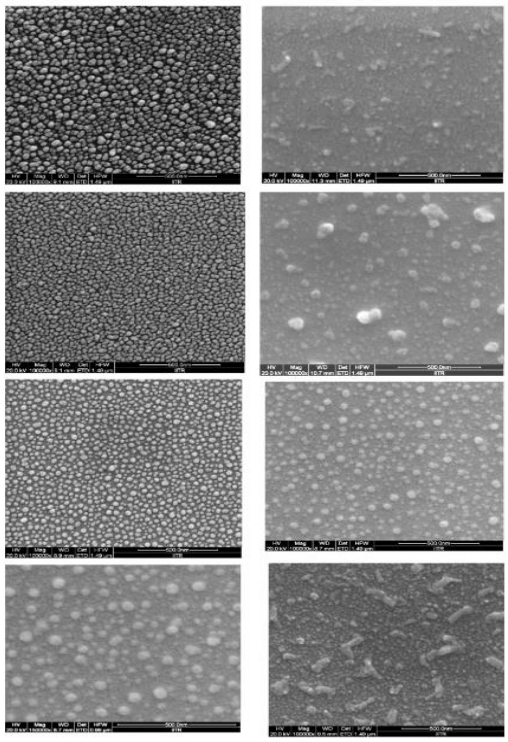

Figure 1.18 SEM of Ag nanoparticles by thermal annealing Ag film by evaporation under different heating temperatures from 50 to 400 ^{o}C.[106]

Although metal nanoparticles could be fabricated by chemical synthesis method, the thermal annealing process under high temperatures for the metal film deposited by vacuum equipment is an effective approach to achieve the load of nanoparticles with strong bonds with semiconductors. The particle size, shape and coverage could be tailored by the morphology of metal film and annealing conditions including the temperature, duration time and atmosphere.[107] As a result, the LSPR properties could be further modified due to the close relationship between LSPR and particle morphology. N.venugopal reported the Ag nanoparticles fabrication by thermally evaporating Ag film under different substrate temperatures. The Ag film deposited under low temperature showed an anisotropic morphology. With the temperature

increasing, the hill-like shape began to transfer to a valley hillock. Continue to increase the temperature, regular isotropic nanoparticles were formed and the shape transfer from spheroid to ellipsoidal occurred. Too high temperatures would lead to the generation of worm-like morphology on the surface.

d. Lithography pattern methods

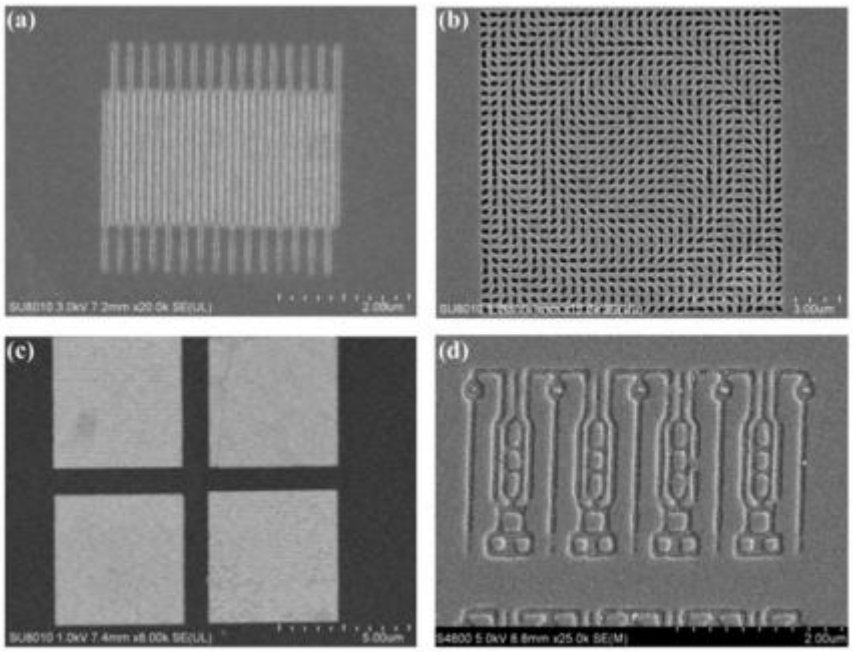

Figure 1.19 SEM of nanostructure fabricated by lithography method.[108]

Optical lithography is the most widely applied method in modern industry, especially in the semiconductors fields such as chips and power electronics. Shortening the light source wavelength by using deep ultraviolet (193 nm) or even extreme ultraviolet (13.5 nm) is an effective way to resolve diffraction-limited resolution in the optical lithography process.[108] For those features smaller than the light wavelength, optical lithography would become inaccessible. In this case, electron-beam-lithography (EBL) and focused-ion-beam (FIB) etching are two alternative methods to resolve the problem mentioned above.[109-110] As shown by Figure 1.19, it is easy to obtain the nanostructure or nanoarrays with the desired shape,

size and period by the lithography method using different masks or pattern procedures designed before the lithography. Therefore, researchers could investigate the various optical properties of LSRP with different nanostructures.

1.3.3 Application of LSPR in photo energy conversion

As mentioned above, the noble metal nanoparticles have tunable LSPR properties that are sensitive to the shape, size and period in nanostructures and the dielectric medium.[111] The light absorption could be achieved in the visible region by adjusting the morphology of metal nanoparticles. The LSPR-induced carrier separation after the generation of hot carriers has been widely reported.[112] This mechanism could successfully achieve the photo energy conversion in the visible region for those wide bandgap semiconductors without changing their band structures.

a. LSPR enhanced solar cells

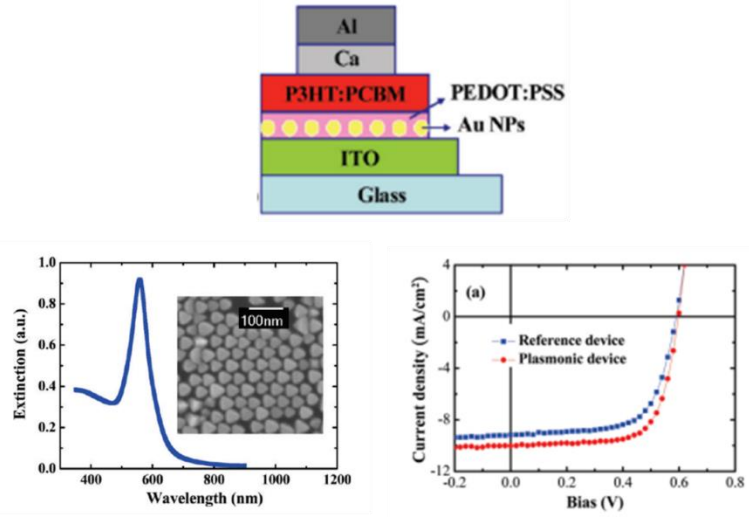

Figure 1.20 Schematic of Au NPs in the PEDOT:PSS layer and its J-V curve.[113]

Jyh-Lih Wu reported an improvement of solar energy conversion efficiency in organic solar cells by incorporating Au-NPs in the buffer layer as shown in the schematic (Figure 1.20).[113] Au-NPs were fabricated by the hydrothermal synthesis to form the octahedral structure using a mixture solution containing the $HAuCl_4 \cdot 3H_2O$, CTAB and $Na_3C_6H_5O_7 \cdot 2H_2O$. The Au-NPs showed a strong LSPR peak at 550 nm

with a size of around 45 nm which was very close to the absorption peak of the active layer consisting of P3HT/PCBM. Therefore, the light absorption efficiency was dramatically enhanced even though the thickness of the active layer was not such thick. Both the photocurrent and fill factor were increased with the same open circuit voltage meaning the interface between organics and electrodes was not destroyed.

b. LSPR assisted water splitting in visible region

The band structure of some wide bandgap semiconductors is appropriate to the overall water splitting due to their suitable CB and VB potentials such as TiO_2, $SrTiO_3$ and ZnO. However, the large bandgap also limits their application in visible light-driven water splitting because they are only active in the UV region. The LSPR-induced hot carrier generation and the separation by the Schottky junction was reported to be a strategy for the water splitting under visible irradiation using wide bandgap semiconductors.

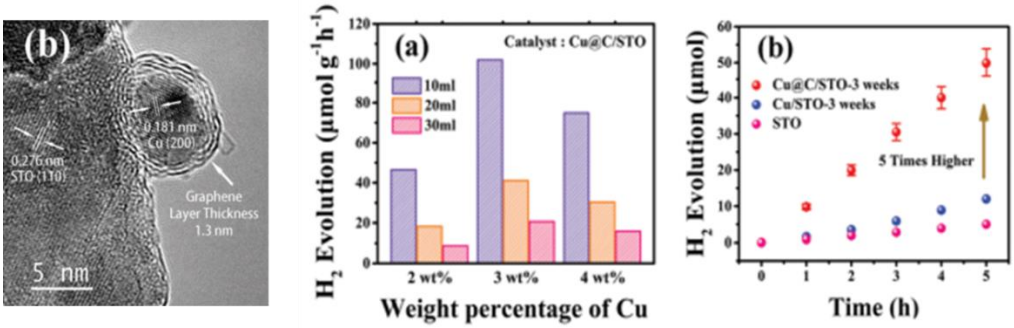

Figure 1.21 TEM of Cu@C/STO and the H_2 evolution using Cu@C/STO under visible light.[114]

Tong et.al reported an H_2 evolution under visible light using the photocatalyst which consists of Cu@C/STO. In this study, a tunable C cage was introduced to keep the Cu particles stable because it is easy to be oxidized by the oxygen and water in the air. The Cu@C/STO showed much better H_2 evolution performance than the pure STO catalyst (almost 5 times enhancement). Similar works based on the STO semiconductor assisted by LSPR of metal NPs were also reported by Trang et.al and Zhong et.al.[115]

c. LSPR enhanced CO_2 reduction under visible irradiation

CO_2 is the main reason for global warming which could cause series of climate problems. Thus, the transformation of CO_2 to other useful fuel or products that are similar to photosynthesis has drawn much interest. Many progresses have been achieved to reduce CO_2 to CO, CH_4 and CH_3OH by designing different structures or loading noble metal-NPs.[116]

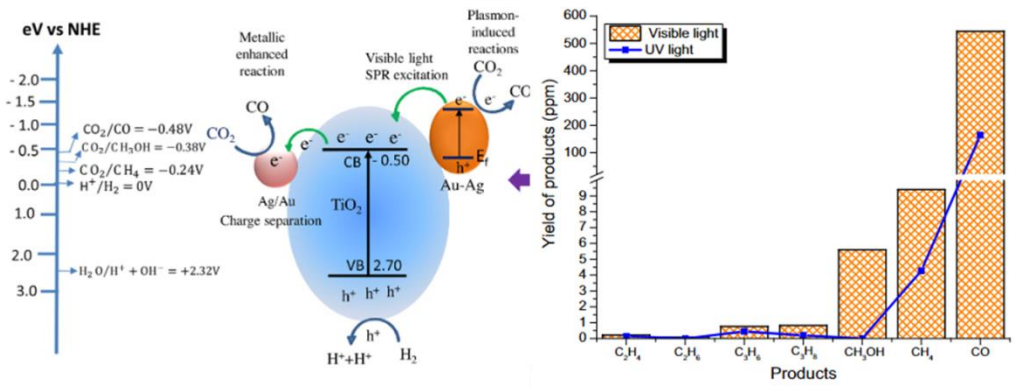

Figure 1.22 Mechanism of CO_2 reduction by Au/Ag-NPs loaded TiO_2 and the reduction products.[117]

Tahir M designed Au/Ag-NPs loaded TiO_2 nanowires to achieve CO_2 reduction under visible light.[117] The hydrothermal method was applied to fabricate the TiO_2 nanowires. Au/Ag-NPs were deposited on TiO_2 by chemical reduction and photo-deposition. As illustrated by the mechanism diagram in Figure 1.22, LSPR-excited hot electrons with higher energy from Au-Ag alloy NPs by visible light could be transferred to the CB of TiO_2. The Au/Ag-NPs with smaller size could promote the separation between electrons and holes due to the sink effect for electrons so that it owns a longer lifetime. This plasmonic structure showed high selectivity to generate the CO from CO_2 reduction. And the CO amount generated under visible light was 3.8 times more than that by UV irradiation which resulted from the LSPR effect of Au/Ag-NPs.

1.4 Overview of thesis

In this thesis, the LSPR-induced photocurrent generation in the visible region using wide bandgap semiconductor Ga_2O_3 that owns negative CB potential was investigated. This study mainly focused on a) the photocurrent generation on differently sized Au-NPs loaded Ga_2O_3, b) enhanced charges separation by an interfacial modification based on the holes trapping ability of thin TiO_2 layer, and c) further improvement in light absorption and PEC conversion efficiency by constructing the modal strong coupling between nanocavity mode and LSPR mode. In chapter 2, Au-NPs with different particle sizes loaded SC-Ga_2O_3 were fabricated by annealing different thickness Au film and the PEC properties were characterized. Chapter 3 introduced the interfacial modification on Au-NPs/SC-Ga_2O_3 by a thin layer of TiO_2. The deposition position of TiO_2 was explored. The structure consisting of Au-NPs partially inlaid by TiO_2 would not damage the electrons transfer from Au-NPs to SC-Ga_2O_3 while the holes-trapping ability was further enhanced by TiO_2, resulting in the improved photocurrent in the visible region. In chapter 4, an optimized Ga_2O_3 film with good semiconductor properties was obtained by the PLD method. A new method by depositing a TiN layer on Au-film under high deposition temperature was developed. Optical nanocavity was formed by depositing Ga_2O_3 film on TiN/Au-film. A tuning condition was achieved when the LSPR and cavity resonance wavelength overlapped overcoming the poor absorption of a single layer Au-NPs as described in chapter 2 and 3. Furthermore, water splitting in the visible region was accomplished at zero bias potential by the advantages of the negative CB potential of Ga_2O_3. Based on the results in these chapters, it demonstrated that the Ga_2O_3 owing negative CB potential shows huge promise in the PEC performance in the visible region, especially in that fields requiring negative reduction potential such as CO_2 reduction.

1.5 Reference

1. Nguyen, C. P.; Schinckus, C.; Su, T. D.; Chong, F. H. L., The Energy Consumption: The Global Contributions from Financial Development and Institutions. Environ Sci Pollut Res Int **2022**, 29, 18721-18740.

2. Coulibaly, S. K.; Erbao, C.; Metuge Mekongcho, T., Economic Globalization, Entrepreneurship, and Development. Technological Forecasting and Social Change **2018**, 127, 271-280.

3. Marra, A.; Colantonio, E., The Path to Renewable Energy Consumption in the European Union through Drivers and Barriers: A Panel Vector Autoregressive Approach. Socio-Economic Planning Sciences **2021**, 76, 100958.

4. Kreps, B. H., The Rising Costs of Fossil-Fuel Extraction: An Energy Crisis That Will Not Go Away. American Journal of Economics and Sociology **2020**, 79, 695-717.

5. Barbir, F.; Veziroglu, T.; Plassjr, H., Environmental Damage Due to Fossil Fuels Use. International Journal of Hydrogen Energy **1990**, 15, 739-749.

6. Perera, F. P., Multiple Threats to Child Health from Fossil Fuel Combustion: Impacts of Air Pollution and Climate Change. Environ Health Perspect **2017**, 125, 141-148.

7. Perera, F., Pollution from Fossil-Fuel Combustion Is the Leading Environmental Threat to Global Pediatric Health and Equity: Solutions Exist. Int J Environ Res Public Health **2017**, 15, 16.

8. Pumijumnong, N.; Palakit, K., Effects of Climate Variability on the Annual and Intra-Annual Ring Formation of Pinus Merkusii Growing in Central Thailand. Environment and Natural Resources Journal **2020**, 18, 234-248.

9. Nema, P.; Nema, S.; Roy, P., An Overview of Global Climate Changing in Current Scenario and Mitigation Action. Renewable and Sustainable Energy Reviews **2012**, 16, 2329-2336.

10. Sinha, R. K.; Chaturvedi, N. D., A Review on Carbon Emission Reduction in Industries and Planning Emission Limits. Renewable and Sustainable Energy Reviews **2019**, 114, 109304.

11. Jiang, S.; Li, Y.; Lu, Q.; Hong, Y.; Guan, D.; Xiong, Y.; Wang, S., Policy Assessments for the Carbon Emission Flows and Sustainability of Bitcoin Blockchain Operation in China. Nat Commun **2021**, 12, 1938.

12. Nathaniel, S. P.; Alam, M. S.; Murshed, M.; Mahmood, H.; Ahmad, P., The Roles of Nuclear Energy, Renewable Energy, and Economic Growth in the Abatement of Carbon Dioxide Emissions in the G7 Countries. Environ Sci Pollut Res Int **2021**, 28, 47957-47972.

13. Sahin, A., Progress and Recent Trends in Wind Energy. Progress in Energy and Combustion Science **2004**, 30, 501-543.

14. Kannan, N.; Vakeesan, D., Solar Energy for Future World: -A Review. Renewable and Sustainable Energy Reviews **2016**, 62, 1092-1105.

15. Tanaka, S.; Zabel, J., Valuing Nuclear Energy Risk: Evidence from the Impact of the Fukushima Crisis on U.S. House Prices. Journal of Environmental Economics and Management **2018**, 88, 411-426.

16. Rabaia, M. K. H.; Abdelkareem, M. A.; Sayed, E. T.; Elsaid, K.; Chae, K. J.; Wilberforce, T.; Olabi, A. G., Environmental Impacts of Solar Energy Systems: A Review. Sci Total Environ **2021**, 754, 141989.

17. Sobek, S.; Werle, S., Solar Pyrolysis of Waste Biomass: Part 1 Reactor Design. Renewable Energy **2019**, 143, 1939-1948.

18. Singh, G.; Kalam, A. P. J. A.; Singh, B. R., Recent Developments in Hybrid Solar Power Generation: A Review. International Journal of Engineering Research & Technology **2019**, 8, 1019-1031.

19. Hernández-Callejo, L.; Gallardo-Saavedra, S.; Alonso-Gómez, V., A Review of

Photovoltaic Systems: Design, Operation and Maintenance. Solar Energy **2019**, 188, 426-440.

20. Liu, Y., High-Efficiency Silicon Heterojunction Solar Cells: Materials, Devices and Applications. Materials Science and Engineering: R: Reports **2020**, 142, 100579.

21. Haschke, J.; Dupré, O.; Boccard, M.; Ballif, C., Silicon Heterojunction Solar Cells: Recent Technological Development and Practical Aspects-from Lab to Industry. Solar Energy Materials and Solar Cells **2018**, 187, 140-153.

22. Yan, D.; Cuevas, A.; Michel, J. I.; Zhang, C.; Wan, Y.; Zhang, X.; Bullock, J., Polysilicon Passivated Junctions: The Next Technology for Silicon Solar Cells? Joule **2021**, 5, 811-828.

23. Sobayel, K.; Shahinuzzaman, M.; Amin, N.; Karim, M. R.; Dar, M. A.; Gul, R.; Alghoul, M. A.; Sopian, K.; Hasan, A. K. M.; Akhtaruzzaman, M., Efficiency Enhancement of Cigs Solar Cell by Ws2 as Window Layer through Numerical Modelling Tool. Solar Energy **2020**, 207, 479-485.

24. Pal, K.; Singh, P.; Bhaduri, A.; Thapa, K. B., Current Challenges and Future Prospects for a Highly Efficient (>20%) Kesterite Czts Solar Cell: A Review. Solar Energy Materials and Solar Cells **2019**, 196, 138-156.

25. Kim, J. Y.; Lee, J. W.; Jung, H. S.; Shin, H.; Park, N. G., High-Efficiency Perovskite Solar Cells. Chem Rev **2020**, 120, 7867-7918.

26. Park, B. W.; Seok, S. I., Intrinsic Instability of Inorganic-Organic Hybrid Halide Perovskite Materials. Adv Mater **2019**, 31, e1805337.

27. Nguyen, V.-H., Towards Artificial Photosynthesis: Sustainable Hydrogen Utilization for Photocatalytic Reduction of CO_2 to High-Value Renewable Fuels. Chemical Engineering Journal **2020**, 402, 126184.

28. Roy, N.; Suzuki, N.; Terashima, C.; Fujishima, A., Recent Improvements in the Production of Solar Fuels: From CO_2 Reduction to Water Splitting and Artificial

Photosynthesis. Bulletin of the Chemical Society of Japan **2019**, 92, 178-192.

29. Ye, S.; Ding, C.; Liu, M.; Wang, A.; Huang, Q.; Li, C., Water Oxidation Catalysts for Artificial Photosynthesis. Adv Mater **2019**, 31, e1902069.

30. Islam, A.; Teo, S. H.; Awual, M. R.; Taufiq-Yap, Y. H., Assessment of Clean H_2 Energy Production from Water Using Novel Silicon Photocatalyst. Journal of Cleaner Production **2020**, 244, 118805.

31. Wang, Q.; Domen, K., Particulate Photocatalysts for Light-Driven Water Splitting: Mechanisms, Challenges, and Design Strategies. Chem Rev **2020**, 120, 919-985.

32. Saraswat, S. K.; Rodene, D. D.; Gupta, R. B., Recent Advancements in Semiconductor Materials for Photoelectrochemical Water Splitting for Hydrogen Production Using Visible Light. Renewable and Sustainable Energy Reviews **2018**, 89, 228-248.

33. Wang, K.; Huang, D.; Yu, L.; Feng, K.; Li, L.; Harada, T.; Ikeda, S.; Jiang, F., Promising Gese Nanosheet-Based Thin-Film Photocathode for Efficient and Stable Overall Solar Water Splitting. ACS Catalysis **2019**, 9, 3090-3097.

34. Fajrina, N.; Tahir, M., A Critical Review in Strategies to Improve Photocatalytic Water Splitting Towards Hydrogen Production. International Journal of Hydrogen Energy **2019**, 44, 540-577.

35. Hashimoto, K.; Irie, H.; Fujishima, A., TiO_2 photocatalysis: A Historical Overview and Future Prospects. Japanese Journal of Applied Physics **2005**, 44, 8269-8285.

36. Yang, Y.; Niu, S.; Han, D.; Liu, T.; Wang, G.; Li, Y., Progress in Developing Metal Oxide Nanomaterials for Photoelectrochemical Water Splitting. Advanced Energy Materials **2017**, 7, 1700555.

37. Wang, G.; Wang, H.; Ling, Y.; Tang, Y.; Yang, X.; Fitzmorris, R. C.; Wang, C.; Zhang, J. Z.; Li, Y., Hydrogen-Treated TiO_2 Nanowire Arrays for

Photoelectrochemical Water Splitting. Nano Lett **2011**, 11, 3026-33.

38. Hou, Y.; Wang, X.; Wu, L.; Ding, Z.; Fu, X., Efficient Decomposition of Benzene over a β-Ga_2O_3 Photocatalyst under Ambient Conditions. Environ Sci Technol **2006**, 40, 5799-803.

39. Sakata, Y.; Nakagawa, T.; Nagamatsu, Y.; Matsuda, Y.; Yasunaga, R.; Nakao, E.; Imamura, H., Photocatalytic Properties of Gallium Oxides Prepared by Precipitation Methods toward the Overall Splitting of H_2O. Journal of Catalysis **2014**, 310, 45-50.

40. Orita, M.; Ohta, H.; Hirano, M.; Hosono, H., Deep-Ultraviolet Transparent Conductive β-Ga_2O_3 Thin Films. Applied Physics Letters **2000**, 77, 4166-4168.

41. Rafique, S.; Han, L.; Zhao, H., Synthesis of Wide Bandgap β-Ga_2O_3 (Eg ~ 4.6-4.7 Ev) Thin Films on Sapphire by Low Pressure Chemical Vapor Deposition. physica status solidi (a) **2016**, 213, 1002-1009.

42. Yan, X.; Esqueda, I. S.; Ma, J.; Tice, J.; Wang, H., High Breakdown Electric Field in β-Ga_2O_3/Graphene Vertical Barristor Heterostructure. Applied Physics Letters **2018**, 112, 032101.

43. Wang, C.; Zhang, J.; Xu, S.; Zhang, C.; Feng, Q.; Zhang, Y.; Ning, J.; Zhao, S.; Zhou, H.; Hao, Y., Progress in State-of-the-Art Technologies of β-Ga_2O_3 Devices. Journal of Physics D: Applied Physics **2021**, 54, 243001.

44. Fiedler, A.; Schewski, R.; Galazka, Z.; Irmscher, K., Static Dielectric Constant of β-Ga_2O_3 Perpendicular to the Principal Planes (100), (010), and (001). ECS Journal of Solid State Science and Technology **2019**, 8, Q3083-Q3085.

45. Oh, S.; Yang, G.; Kim, J., Electrical Characteristics of Vertical Ni/β-Ga_2O_3 schottky Barrier Diodes at High Temperatures. ECS Journal of Solid State Science and Technology **2016**, 6, Q3022-Q3025.

46. Oh, S.; Kim, C.-K.; Kim, J., High Responsivity β-Ga_2O_3 Metal-Semiconductor–Metal Solar-Blind Photodetectors with Ultraviolet Transparent Graphene Electrodes.

ACS Photonics **2017**, 5, 1123-1128.

47. Higashiwaki, M.; Sasaki, K.; Kuramata, A.; Masui, T.; Yamakoshi, S., Gallium Oxide (Ga_2O_3) Metal-Semiconductor Field-Effect Transistors on Single-Crystal β-Ga_2O_3 (010) Substrates. Applied Physics Letters **2012**, 100, 013504.

48. Yao, Y.; Gangireddy, R.; Kim, J.; Das, K. K.; Davis, R. F.; Porter, L. M., Electrical Behavior of β-Ga_2O_3 Schottky Diodes with Different Schottky Metals. Journal of Vacuum Science & Technology B, Nanotechnology and Microelectronics: Materials, Processing, Measurement, and Phenomena **2017**, 35, 03D113.

49. Oshima, T.; Okuno, T.; Fujita, S., Ga_2O_3 thin Film Growth On c-Plane Sapphire Substrates by Molecular Beam Epitaxy for Deep-Ultraviolet Photodetectors. Japanese Journal of Applied Physics **2007**, 46, 7217-7220.

50. Liu, Z.; Yamazaki, T.; Shen, Y.; Kikuta, T.; Nakatani, N.; Li, Y., O_2 and CO Sensing of Ga_2O_3 Multiple Nanowire Gas Sensors. Sensors and Actuators B: Chemical **2008**, 129, 666-670.

51. Guo, D.; Guo, Q.; Chen, Z.; Wu, Z.; Li, P.; Tang, W., Review of Ga_2O_3-Based Optoelectronic Devices. Materials Today Physics **2019**, 11, 100157.

52. Kracht, M.; Karg, A.; Feneberg, M.; Bläsing, J.; Schörmann, J.; Goldhahn, R.; Eickhoff, M., Anisotropic Optical Properties of Metastable (0 1 -1 2) α-Ga_2O_3 Grown by Plasma-Assisted Molecular Beam Epitaxy. Physical Review Applied **2018**, 10, 024047.

53. Ahmadi, E.; Oshima, Y., Materials Issues and Devices of α- and β-Ga_2O_3. Journal of Applied Physics **2019**, 126, 160901.

54. Playford, H. Y.; Hannon, A. C.; Tucker, M. G.; Dawson, D. M.; Ashbrook, S. E.; Kastiban, R. J.; Sloan, J.; Walton, R. I., Characterization of Structural Disorder in γ-Ga_2O_3. The Journal of Physical Chemistry C **2014**, 118, 16188-16198.

55. Hayashi, H.; Huang, R.; Ikeno, H.; Oba, F.; Yoshioka, S.; Tanaka, I.; Sonoda, S.,

Room Temperature Ferromagnetism in Mn-Doped γ-Ga_2O_3 with Spinel Structure. Applied Physics Letters **2006**, 89, 181903.

56. Mezzadri, F.; Calestani, G.; Boschi, F.; Delmonte, D.; Bosi, M.; Fornari, R., Crystal Structure and Ferroelectric Properties of ε-Ga_2O_3 Films Grown on (0001)-Sapphire. Inorg Chem **2016**, 55, 12079-12084.

57. Matsuzaki, K.; Hiramatsu, H.; Nomura, K.; Yanagi, H.; Kamiya, T.; Hirano, M.; Hosono, H., Growth, Structure and Carrier Transport Properties of Ga_2O_3 Epitaxial Film Examined for Transparent Field-Effect Transistor. Thin Solid Films **2006**, 496, 37-41.

58. Víllora, E. G.; Shimamura, K.; Yoshikawa, Y.; Aoki, K.; Ichinose, N., Large-Size β-Ga_2O_3 Single Crystals and Wafers. Journal of Crystal Growth **2004**, 270, 420-426.

59. Castro-Fernández, P.; Blanco, M. V.; Verel, R.; Willinger, E.; Fedorov, A.; Abdala, P. M.; Müller, C. R., Atomic-Scale Insight into the Structure of Metastable γ-Ga_2O_3 Nanocrystals and Their Thermally-Driven Transformation to β-Ga_2O_3. The Journal of Physical Chemistry C **2020**, 124, 20578-20588.

60. Rafique, S.; Han, L.; Zhao, H., Ultrawide Bandgap β-Ga_2O_3 Thin Films Growths, Properties and Devices. ECS Transactions **2017**, 80, 203.

61. Maeda, K.; Domen, K., New Non-Oxide Photocatalysts Designed for Overall Water Splitting under Visible Light. The Journal of Physical Chemistry C **2007**, 111, 7851-7861.

62. Li, Y.; Tokizono, T.; Liao, M.; Zhong, M.; Koide, Y.; Yamada, I.; Delaunay, J.-J., Efficient Assembly of Bridged β-Ga_2O_3 Nanowires for Solar-Blind Photodetection. Advanced Functional Materials **2010**, 20, 3972-3978.

63. Biswas, M.; Nishinaka, H., Thermodynamically Metastable α-, ε-(or κ-), and γ-Ga_2O_3: From Material Growth to Device Applications. APL Materials **2022**, 10, 060701.

64. Ma, N.; Tanen, N.; Verma, A.; Guo, Z.; Luo, T.; Xing, H.; Jena, D., Intrinsic Electron Mobility Limits In β- Ga_2O_3. Applied Physics Letters **2016**, 109, 212101.

65. Xue, H.; He, Q.; Jian, G.; Long, S.; Pang, T.; Liu, M., An Overview of the Ultrawide Bandgap Ga_2O_3 Semiconductor-Based Schottky Barrier Diode for Power Electronics Application. Nanoscale Res Lett **2018**, 13, 290.

66. Mohamed, M.; Unger, I.; Janowitz, C.; Manzke, R.; Galazka, Z.; Uecker, R.; Fornari, R., The Surface Band Structure of β-Ga_2O_3. Journal of Physics: Conference Series **2011**, 286, 012027.

67. Sun, D.; Gao, Y.; Xue, J.; Zhao, J., Defect Stability and Electronic Structure of Doped β-Ga_2O_3: A Comprehensive Ab Initio Study. Journal of Alloys and Compounds **2019**, 794, 374-384.

68. Chikoidze, E., P-Type B-Gallium Oxide: A New Perspective for Power and Optoelectronic Devices. Materials Today Physics **2017**, 3, 118-126.

69. Guo, D.; Li, P.; Wu, Z.; Cui, W.; Zhao, X.; Lei, M.; Li, L.; Tang, W., Inhibition of Unintentional Extra Carriers by Mn Valence Change for High Insulating Devices. Sci Rep **2016**, 6, 24190.

70. Wang, B.; Xiao, M.; Knoll, J.; Buttay, C.; Sasaki, K.; Lu, G.-Q.; Dimarino, C.; Zhang, Y., Low Thermal Resistance (0.5 K/W) Ga_2O_3 Schottky Rectifiers with Double-Side Packaging. IEEE Electron Device Letters **2021**, 42, 1132-1135.

71. Higashiwaki, M.; Kuramata, A.; Murakami, H.; Kumagai, Y., State-of-the-Art Technologies of Gallium Oxide Power Devices. Journal of Physics D: Applied Physics **2017**, 50, 333002.

72. Comstock, D. J.; Elam, J. W., Atomic Layer Deposition of Ga_2O_3 Films Using Trimethylgallium and Ozone. Chemistry of Materials **2012**, 24, 4011-4018.

73. Sasaki, K.; Higashiwaki, M.; Kuramata, A.; Masui, T.; Yamakoshi, S., Mbe Grown Ga_2O_3 and Its Power Device Applications. Journal of Crystal Growth **2013**,

378, 591-595.

74. Hou, X., Review of Polymorphous Ga_2O_3 Materials and Their Solar-Blind Photodetector Applications. Journal of Physics D: Applied Physics **2020**, 54, 043001.

75. Pilliadugula, R.; Krishnan, N. G., Effect of Ph Dependent Morphology on Room Temperature Nh3 Sensing Performances of β-Ga_2O_3. Materials Science in Semiconductor Processing **2020**, 112, 105007.

76. Yu, X. F.; Li, Y. C.; Cheng, J. B.; Liu, Z. B.; Li, Q. Z.; Li, W. Z.; Yang, X.; Xiao, B., Monolayer Ti_2CO_2: A Promising Candidate for NH_3 Sensor or Capturer with High Sensitivity and Selectivity. ACS Appl Mater Interfaces **2015**, 7, 13707-13713.

77. Akatsuka, M.; Kawaguchi, Y.; Itoh, R.; Ozawa, A.; Yamamoto, M.; Tanabe, T.; Yoshida, T., Preparation of β-Ga_2O_3 Photocatalyst Highly Active for CO_2 Reduction with Water without Cocatalyst. Applied Catalysis B: Environmental **2020**, 262, 118247.

78. Ito, R.; Akatsuka, M.; Ozawa, A.; Kato, Y.; Kawaguchi, Y.; Yamamoto, M.; Tanabe, T.; Yoshida, T., Photocatalytic Activity of Ga_2O_3 Supported on Al_2O_3 for Water Splitting and CO_2 Reduction. ACS Omega **2019**, 4, 5451-5458.

79. Bahadar, H.; Mostafalou, S.; Abdollahi, M., Current Understandings and Perspectives on Non-Cancer Health Effects of Benzene: A Global Concern. Toxicol Appl Pharmacol **2014**, 276, 83-94.

80. Li, Q., Enhanced Activity of β-Ga_2O_3 by Substitution with Transition Metal for CO_2 Photoreduction under Visible Light Irradiation. Catalysis Communications **2019**, 120, 23-27.

81. Kudo, A.; Mikami, I., Photocatalytic Activities and Photophysical Properties of $Ga_{2-x}In_xO_3$ Solid Solution. Journal of the Chemical Society, Faraday Transactions **1998**, 94, 2929-2932.

82. Nishijima, Y.; Ueno, K.; Kotake, Y.; Murakoshi, K.; Inoue, H.; Misawa, H.,

Near-Infrared Plasmon-Assisted Water Oxidation. J Phys Chem Lett **2012**, 3, 1248-1252.

83. Liu, L.; Ouyang, S.; Ye, J., Gold-Nanorod-Photosensitized Titanium Dioxide with Wide-Range Visible-Light Harvesting Based on Localized Surface Plasmon Resonance. Angew Chem Int Ed Engl **2013**, 52, 6689-93.

84. Zhang, J.; Zhang, L.; Xu, W., Surface Plasmon Polaritons: Physics and Applications. Journal of Physics D: Applied Physics **2012**, 45, 113001.

85. Kretschmann, E.; Raether, H., Notizen: Radiative Decay of Non Radiative Surface Plasmons Excited by Light. Zeitschrift für Naturforschung A **1968**, 23, 2135-2136.

86. Tang, Y.; Zeng, X.; Liang, J., Surface Plasmon Resonance: An Introduction to a Surface Spectroscopy Technique. J Chem Educ **2010**, 87, 742-746.

87. Gieseking, R. L. M., Plasmons: Untangling the Classical, Experimental, and Quantum Mechanical Definitions. Mater Horiz **2022**, 9, 25-42.

88. Ghosh, S. K.; Pal, T., Interparticle Coupling Effect on the Surface Plasmon Resonance of Gold Nanoparticles: From Theory to Applications. Chem Rev **2007**, 107, 4797-862.

89. Thangamuthu, M.; Raziman, T. V.; Martin, O. J. F.; Tang, J., Review-Origin and Promotional Effects of Plasmonics in Photocatalysis. Journal of The Electrochemical Society **2022**, 169, 036512.

90. Freestone, I.; Meeks, N.; Sax, M.; Higgitt, C., The Lycurgus Cup-a Roman Nanotechnology. Gold Bulletin **2007**, 40, 270-277.

91. Maier, S. A., Plasmonics: Fundamentals and Applications. Springer: New York **2007**.

92. Horvath, H., Gustav Mie and the Scattering and Absorption of Light by Particles: Historic Developments and Basics. Journal of Quantitative Spectroscopy and

Radiative Transfer **2009**, 110, 787-799.

93. Sonnichsen, C.; Franzl, T.; Wilk, T.; von Plessen, G.; Feldmann, J.; Wilson, O.; Mulvaney, P., Drastic Reduction of Plasmon Damping in Gold Nanorods. Phys Rev Lett **2002**, 88, 077402.

94. Li, X.; Xiao, D.; Zhang, Z., Landau Damping of Quantum Plasmons in Metal Nanostructures. New Journal of Physics **2013**, 15, 023011.

95. Brongersma, M. L.; Halas, N. J.; Nordlander, P., Plasmon-Induced Hot Carrier Science and Technology. Nat Nanotechnol **2015**, 10, 25-34.

96. Wang, F.; Melosh, N. A., Plasmonic Energy Collection through Hot Carrier Extraction. Nano Lett **2011**, 11, 5426-5430.

97. Jian, C.-c.; Zhang, J.; He, W.; Ma, X., Au-Al Intermetallic Compounds: A Series of More Efficient Lspr Materials for Hot Carriers-Based Applications Than Noble Metal Au. Nano Energy **2021**, 82, 105763.

98. Ma, X. C.; Dai, Y.; Yu, L.; Huang, B. B., Energy Transfer in Plasmonic Photocatalytic Composites. Light Sci Appl **2016**, 5, e16017.

99. Tang, H.; Chen, C. J.; Huang, Z.; Bright, J.; Meng, G.; Liu, R. S.; Wu, N., Plasmonic Hot Electrons for Sensing, Photodetection, and Solar Energy Applications: A Perspective. J Chem Phys **2020**, 152, 220901.

100. Watanabe, K.; Menzel, D.; Nilius, N.; Freund, H. J., Photochemistry on Metal Nanoparticles. Chem Rev **2006**, 106, 4301-4320.

101. Dai, H.; Zhang, S.; Li, Y.; Lin, Y., Excellent Graphitic Carbon Nitride Nanosheets-Based Photoelectrochemical Platform Motivated by Schottky Barrier and Lspr Effect and Its Sensing Application. Analyst **2015**, 140, 3514-3520.

102. Bhargava, S. K.; Booth, J. M.; Agrawal, S.; Coloe, P.; Kar, G., Gold Nanoparticle Formation During Bromoaurate Reduction by Amino Acids. Langmuir **2005**, 21, 5949-5956.

103. Zhao, W.; Gonzaga, F.; Li, Y.; Brook, M. A., Highly Stabilized Nucleotide-Capped Small Gold Nanoparticles with Tunable Size. Advanced Materials **2007**, 19, 1766-1771.

104. Gao, C.; Goebl, J.; Yin, Y., Seeded Growth Route to Noble Metal Nanostructures. Journal of Materials Chemistry C **2013**, 1, 3898-3909.

105. Jana, N. R.; Gearheart, L.; Murphy, C. J., Seeding Growth for Size Control of 5-40 nm Diameter Gold Nanoparticles. Langmuir **2001**, 17, 6782-6786.

106. Venugopal, N.; Mitra, A., Influence of Temperature Dependent Morphology on Localized Surface Plasmon Resonance in Ultra-Thin Silver Island Films. Applied Surface Science **2013**, 285, 357-372.

107. Ebrahimpour, Z.; Mansour, N., Annealing Effects on Electrical Behavior of Gold Nanoparticle Film: Conversion of Ohmic to Non-Ohmic Conductivity. Applied Surface Science **2017**, 394, 240-247.

108. Wang, C.; Zhang, W.; Zhao, Z.; Wang, Y.; Gao, P.; Luo, Y.; Luo, X., Plasmonic Structures, Materials and Lenses for Optical Lithography Beyond the Diffraction Limit: A Review. Micromachines (Basel) **2016**, 7, 118.

109. Yang, J. K. W.; Cord, B.; Duan, H.; Berggren, K. K.; Klingfus, J.; Nam, S.-W.; Kim, K.-B.; Rooks, M. J., Understanding of Hydrogen Silsesquioxane Electron Resist for Sub-5-Nm-Half-Pitch Lithography. Journal of Vacuum Science & Technology B: Microelectronics and Nanometer Structures **2009**, 27, 2622-2627.

110. Wu, M. C.; Aziz, A.; Witt, J. D.; Hickey, M. C.; Ali, M.; Marrows, C. H.; Hickey, B. J.; Blamire, M. G., Structural and Functional Analysis of Nanopillar Spin Electronic Devices Fabricated by 3d Focused Ion Beam Lithography. Nanotechnology **2008**, 19, 485305.

111. Ryu, K. R.; Ha, J. W., Influence of Shell Thickness on the Refractive Index Sensitivity of Localized Surface Plasmon Resonance Inflection Points in Silver-Coated Gold Nanorods. RSC Adv **2020**, 10, 16827-16831.

112. Clavero, C., Plasmon-Induced Hot-Electron Generation at Nanoparticle/Metal-Oxide Interfaces for Photovoltaic and Photocatalytic Devices. Nature Photonics **2014**, 8, 95-103.

113. Wu, J. L.; Chen, F. C.; Hsiao, Y. S.; Chien, F. C.; Chen, P.; Kuo, C. H.; Huang, M. H.; Hsu, C. S., Surface Plasmonic Effects of Metallic Nanoparticles on the Performance of Polymer Bulk Heterojunction Solar Cells. ACS Nano **2011**, 5, 959-67.

114. Tong, L.; Ren, L.; Fu, A.; Wang, D.; Liu, L.; Ye, J., Copper Nanoparticles Selectively Encapsulated in an Ultrathin Carbon Cage Loaded on $SrTiO_3$ as Stable Photocatalysts for Visible-Light H_2 Evolution Via Water Splitting. Chem Commun (Camb) **2019**, 55, 12900-12903.

115. Trang, T. N. Q.; Tran Van, M.; Phan, T. B.; Thu, V. T. H., Spatially Controlled Photogenerated Charge Carriers Induced by $SrTiO_3$-Architectured Heterojunction Nanocubes for a Photocatalytic Hydrogen Evolution Reaction. ACS Applied Energy Materials **2021**, 4, 8910-8921.

116. Vu, N. N.; Kaliaguine, S.; Do, T. O., Plasmonic Photocatalysts for Sunlight-Driven Reduction of CO_2: Details, Developments, and Perspectives. ChemSusChem **2020**, 13, 3967-3991.

117. Tahir, M.; Tahir, B.; Amin, N. A. S., Synergistic Effect in Plasmonic Au/Ag Alloy Nps Co-Coated TiO_2 Nws toward Visible-Light Enhanced CO_2 Photoreduction to Fuels. Applied Catalysis B: Environmental **2017**, 204, 548-560.

Chapter 2

Plasmon Induced Photocurrent Generation on Single Crystal Ga_2O_3

2.1 Introduction

To release the increasing global environmental problems, artificial photosynthesis has drawn much attention.[1-2] In order to achieve efficient overall water splitting, one indispensable condition is that the CB of the semiconductor should be more negative than the reduction potential of H^+/H (0 V vs. RHE).[3] Ga_2O_3 is reported to own a negative CB (-1.0 to -1.5 V vs. RHE), which is promising for overall water splitting.[4-5] It is also expected that the reduction of carbon dioxide to CO or HCOOH could be achieved by the advantages of its negative CB potential.[6-8] However, the largely negative CB potential makes the bandgap of Ga_2O_3 too large to utilize the visible light in solar radiation.[9-10] Band engineering is a common method to adjust the absorption edge for lots of semiconductors.[11] It has been reported by Kudo *et al*. that doping In_2O_3 into β-Ga_2O_3 to form a solid solution could efficiently shift the absorption edge towards to longer wavelength maintaining the H_2 and O_2 evolution.[12] Although the absorption edge could be shifted to longer wavelengths by the doping method, the visible light energy is still insufficiently utilized. Importantly, a positive shift in the CB was generated by doping, leading to the decrease of reduction potential of Ga_2O_3. We aimed to search for a method achieving the use of visible light without changing the negative CB potential.

As discussed in chapter 1, LSPR induced charge generation and separation through the strong interaction between noble metal nanoparticles (Au, Ag) and visible light has drawn much attention.[2, 13] Hot carriers are generated upon LSPR excitation in the metal nanoparticles and separated by the Schottky junction formed at the interface

when settling metal nanoparticles on a semiconductor.[14-15] The hot carriers with sufficient energy higher than the barrier could be transferred to the CB of the semiconductor. And then these hot electrons could take part in the reduction reactions, such as H_2 evolution, while the holes will be captured at the surface states of the semiconductor and participate in the oxidation reactions.[16] Notably, the plasmon-induced electron transfer mechanism will not cause the CB of Ga_2O_3 to shift positively. In this study, plasmonic Au-NPs were loaded on the surface of single-crystal Ga_2O_3 (Au-NPs/SC-Ga_2O_3) to utilize visible light. The size effect of Au-NPs on the photoelectrochemical conversion efficiency of Au-NPs/SC-Ga_2O_3 was investigated.

2.2 Experiment Methods and Characterization

2.2.1 Au-NPs/SC-Ga_2O_3 photoanode fabrication

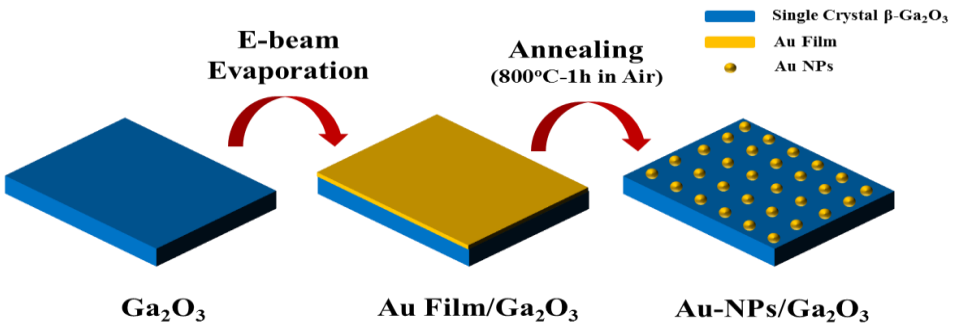

Figure 2.1 Schematic of Au-NPs loaded on SC-Ga_2O_3 photoanode.

The Sn doping single crystal β-Ga_2O_3 substrates with an orientation of (-2 0 1) used in this work were purchased from Novel Crystal Technology, Inc. As shown in Figure 2.1, after a rinsing process with acetone and methanol in an ultrasonic bath for 5min, respectively, a thin gold layer was deposited onto the substrates with a size of $9\times9\times0.7mm^3$ by e-beam evaporation under room temperature. The pressure of the deposition chamber before growth is around 2.0×10^{-6} Pa and the evaporation rate was

set at around 0.15 Å/s. Subsequently, to obtain the gold nanoparticles on the surface of single crystal β-Ga_2O_3, an annealing process under 800°C for 1h in an N_2 atmosphere was applied to achieve the load of Au-NPs as shown in Figure 2.1. To investigate the most proper particle size of Au-NPs for Ga_2O_3, series of sizes of Au-NPs were loaded on the surface of single crystal Ga_2O_3 by annealing Au film with different thicknesses.

2.2.2 Optical properties and morphology characterization

A photonic multichannel analyzer (PMA C7473; Hamamatsu Photonics) system operated within the wavelength range of 400-900 nm was applied to measure the optical spectra. The morphology of annealed Au nanoparticles on Ga_2O_3 with different particle size is identified by the field-emission scanning electron microscopy (FE-SEM, JSM-6700FT, JEOL) with a maximum resolution of 1 nm.

2.2.3 Photoelectrochemical measurement

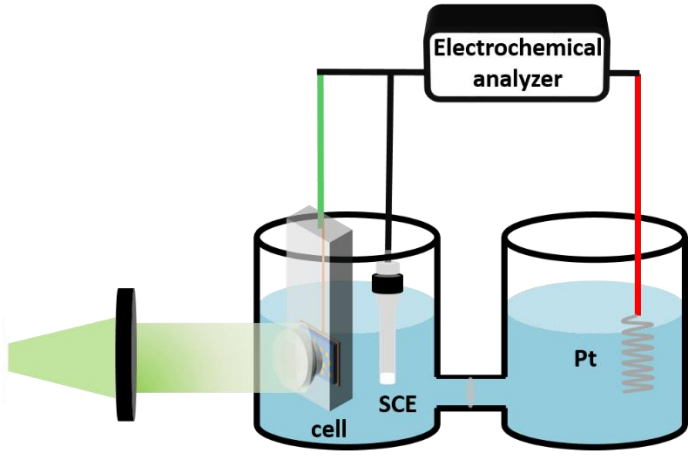

Figure 2.2 Schematic of the three-electrode photoeletrochemical cell for the IPCE measurement.

To obtain the ohmic contact, an In-Ga alloy with a weight ratio of 4:1 was coating on the backside and sidewall of the Ga_2O_3 substrates. Then the TiO_2/Au-NPs/Ga_2O_3 samples were attached to the cooper plate in the cell for measurement by silver paste. The contact position between the lid of the cell with a pinhole (diameter of 2.0 mm)

and the main parts were sealed by tape before being immersed in the electrolyte in case of water penetration. The cell was connected to an electrochemical analyzer (ALS/CH Instruments 852C, ALS) with a copper lead wire. A three-electrode system consisting of a platinum wire and a saturated calomel electrode (SCE) as the counter electrode and a reference electrode was applied to measure the *I-t* spectrum. In addition, the 0.1M $KClO_4$ aqueous solution without any electron donor was selected as the electrolyte. During the measurement of *I-t*, + 0.3 V potential vs. reference electrode was applied on the Au-NPs/Ga_2O_3 working electrode. The incident photon-to-current efficiency (IPCE) was calculated by the formula:

$$IPCE(\lambda) = \frac{1240 \times I(A/cm^2)}{\lambda(nm) \times P_{in}(W/cm^2)}$$

2.2.4 Numerical simulations

Full-field electromagnetic wave simulations were performed using the finite-difference time-domain (FDTD) method solver (FDTD Solutions, Lumerical). A plane wave source was launched and illuminated the structure along the -z direction. The ellipsoid sphere with various diameters of 10 nm, 15 nm, 22 nm and 50 nm in the *x* and *y* directions were used to model the Au-NPs. Accordingly, the z direction was set as 7 nm, 10 nm, 13 nm and 24 nm. The investigated structure was simulated using perfectly matched layers along the *z*-direction and periodic boundary conditions along *x*-and *y*-directions with the period of 15, 20, 35 and 80 nm, respectively. In the simulation, we used Johnson and Christy data for the Au refractive index.[17] The refractive indices of Ga_2O_3 were taken as 1.8, respectively.

2.3 Results and Discussion

2.3.1 Morphology of Au-NPs with different size on SC-Ga_2O_3

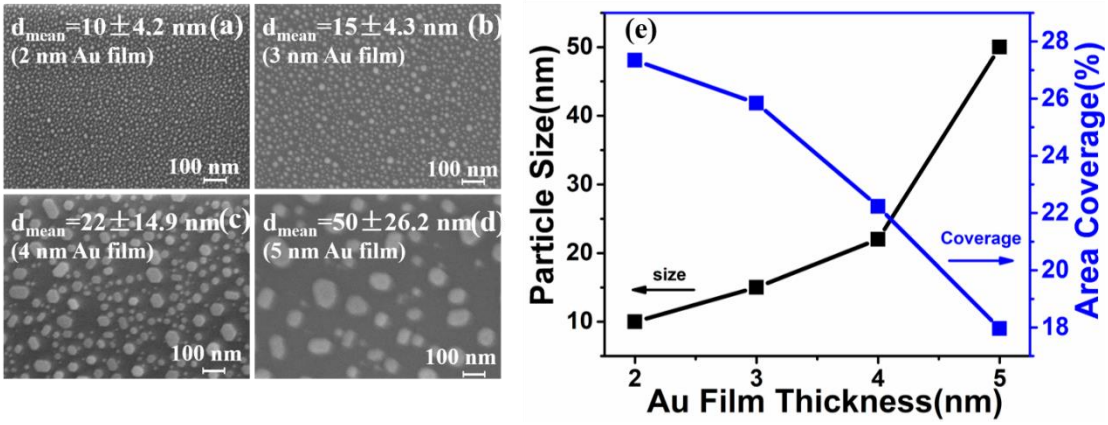

Figure 2.3 SEM images of different size Au-NPs loaded on SC-Ga_2O_3 by annealing (a) 2 nm, (b) 3nm, (c) 4 nm and (d) 5 nm Au film deposited by e-beam evaporation; (e) statistic size and the area coverage of Au-NPs with different size.

As the plasmonic properties of Au-NPs are very sensitive to the particle size, to find the most proper particle size of Au-NPs on Ga_2O_3, a series of Au films with a thickness from 2 nm to 5 nm were deposited on the surface of single crystal Ga_2O_3 following an annealing process.[18] Upon annealing process, it could be seen from the SEM images in Figure 2.3 that the Au-NPs size showed a dependence on the Au film thickness. Au-NPs got larger with the thickness of Au film increasing and the distribution of particles became more non-uniform when the thickness was larger than 4 nm Au film. And some tiny particles were observed in the gap among those large particles shown in Figure 2.3c and 2.3d. According to the particle analysis and size statistics, the average size Au-NPs calculated by ImageJ was 10, 15, 22 and 50 nm shown in the black line in Figure 2.3e, respectively.

2.3.2 Photocurrent generation on Au-NPs loaded SC-Ga_2O_3 with different particles size

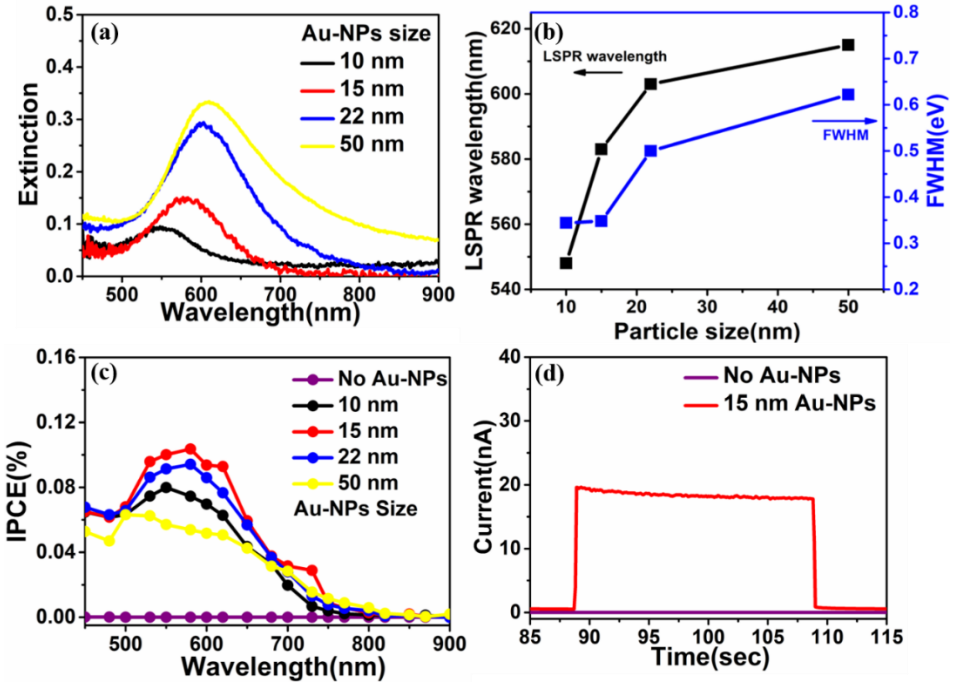

Figure 2.4 (a) Extinction, (b) Linewidth and LSPR wavelength and (c) IPCE spectra of differently sized Au-NPs loaded on Ga_2O_3; (d) I-t curve of SC-Ga_2O_3 with and without loading 15 nm Au-NPs under 600 nm irradiation.

Accordingly, as shown in Figure 2.4a and 2.4b, with the particle size increasing, the LSPR peak in the extinction spectrum showed an obvious red-shift from 550 nm to 610 nm. The full width at half maximum (FWHM) was also broadened with the particle size increasing as shown in Figure 2.4b. The photocurrent conversion efficiency on all Au-NP/Ga_2O_3 photoelectrodes was performed using a three-electrode system. IPCE spectrum calculated by the photocurrent was shown in Figure 2.4c. It could be found that at approximately 580 nm, obvious peaks were observed in the IPCE action spectra of Au-NPs/Ga_2O_3 photoelectrodes. Conversely, in the case of no Au-NPs loaded SC-Ga_2O_3, detectable photo-response was not observed on naked Ga_2O_3 in visible light region indicated by the purple plot in Figure 2.4c. When the Au-NP/Ga_2O_3 photoelectrodes were loaded with small particles (≤ 15 nm), the IPCE

spectra showed a closely similar shape to the extinction spectrum of Au-NPs. Based on the results, it demonstrated that LSPR of Au-NPs loaded on SC-Ga_2O_3 actually induced the photocurrent generation at visible wavelength. The best PEC performance was observed on a 15-nm Au-NP-loaded SC-Ga_2O_3 sample with a peak IPCE value of 0.11% at 580 nm, as shown in Figure 2.4c (red curve). A stable photocurrent was obtained at 600 nm irradiation on SC-Ga_2O_3 loaded by 15 nm Au-NPs with a value of 17 nA, as shown in Figure 2.4d. For the 10-nm Au-NP-loaded Ga_2O_3 sample, the IPCE was lower than the 15-nm Au-NPs/SC-Ga_2O_3 because of its low LSPR intensity. On the other hand, while the particle size got larger than 15 nm, the IPCEs also decreased.

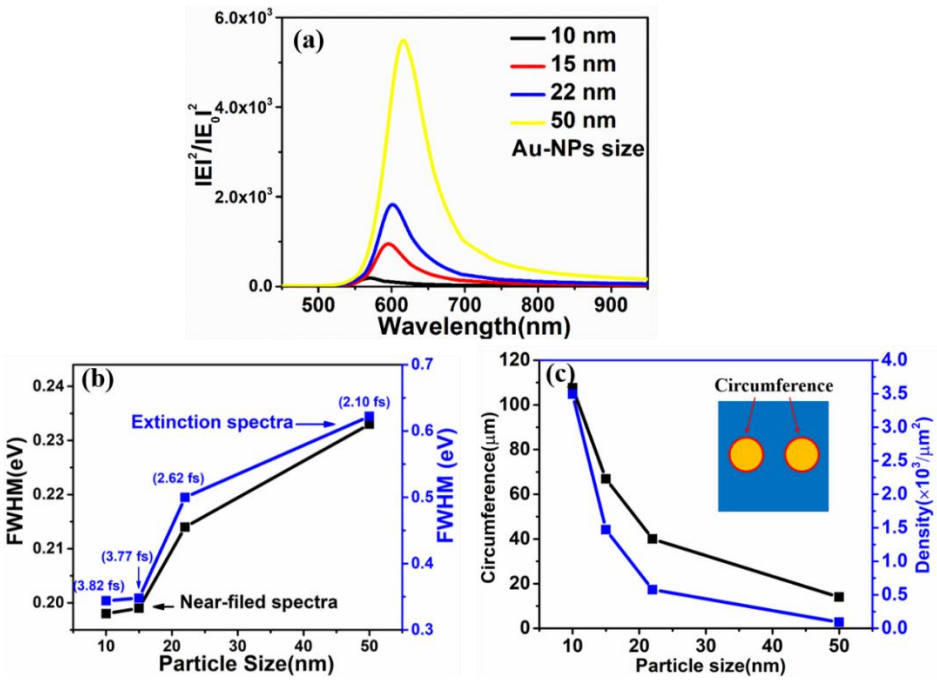

Figure 2.5 (a) Near-field spectrum of Au-NPs/SC-Ga_2O_3 interface with different Au-NPs size simulated by FDTD; (b) FWHM of near-field spectrum and dephasing time of different sized Au-NPs; (c) circumference of interface of Au-NPs/Ga_2O_3 and density of Au-NPs with different size.

For plasmonic systems, the LSPR decay mechanism played an important role in the energy conversion efficiency.[19] To investigate the reason for the IPCE decrease when the particle size was larger than 15 nm, the near-field spectrum of Au-NPs/SC-Ga_2O_3 interface with different Au-NPs sizes was calculated by FDTD shown in Figure 2.5. As we mentioned in the previous chapter, hot carriers were mainly generated through the non-radiative decay process.[20] However, the radiative decay would become the main pathway upon LSPR decay in larger particles that is not favorable for hot carrier generation.[21] According to the near-field enhancement spectrum in Figure 2.5, near-field enhancement spectra showed an obvious broadening trend with the FWHM increasing shown in Figure 2.5b when particle size became larger, which was consistent with extinction spectra. This broadening indicated a short dephasing time (see Figure 2.5b) of LSPR decay in the case of larger Au-NPs due to significant radiation damping which would suppress the hot carrier generation. In addition, the lower area coverage of larger Au-NPs as shown in Figure 2.3 would also reduce the interface of Au-NPs/SC-Ga_2O_3 (Figure 2.5c) where oxidation reaction with holes occurred, resulting in the IPCE decrease.

Therefore, 15 nm Au-NPs loaded SC-Ga_2O_3 showed the best performance for photocurrent generation at visible wavelengths based on the high LSPR intensity and long dephasing time. Therefore, 15 nm was chosen as the particle size of Au-NPs applied in the following sections.

2.4 Conclusion

In this work, we successfully achieved the photocurrent generation on SC-Ga_2O_3 with a large bandgap which is inactive in the visible region by loading Au-NPs. Light absorption was observed in visible after loading Au-NPs. 15 nm was the optimised particle size and 15 nm Au-NPs loaded SC-Ga_2O_3 showed the highest photo energy

conversion efficiency at around 580 nm with a peak IPCE of 0.11%. The low LSPR intensity of smaller Au-NPs would lead to the lower photocurrent generation. Larger particles would decrease the IPCE because the non-radiative decay process domains the LSPR damping suppressing hot carrier generation. We believe this new system has huge potential in the water splitting field and could be applied in various devices for photo energy conversion.

2.5 Reference

1. Boppella, R.; Kochuveedu, S. T.; Kim, H.; Jeong, M. J.; Marques Mota, F.; Park, J. H.; Kim, D. H., Plasmon-Sensitized Graphene/TiO_2 Inverse Opal Nanostructures with Enhanced Charge Collection Efficiency for Water Splitting. ACS Appl Mater Interfaces **2017**, 9, 7075-7083.

2. Zheng, Z.; Xie, W.; Huang, B.; Dai, Y., Plasmon-Enhanced Solar Water Splitting on Metal-Semiconductor Photocatalysts. Chemistry **2018**, 24, 18322-18333.

3. Saraswat, S. K.; Rodene, D. D.; Gupta, R. B., Recent Advancements in Semiconductor Materials for Photoelectrochemical Water Splitting for Hydrogen Production Using Visible Light. Renewable and Sustainable Energy Reviews **2018**, 89, 228-248.

4. Navarrete, M.; Cipagauta‐Díaz, S.; Gómez, R., Ga_2O_3/TiO_2 Semiconductors Free of Noble Metals for the Photocatalytic Hydrogen Production in a Water/Methanolmixture. Journal of Chemical Technology & Biotechnology **2019**, 94, 3457-3465.

5. Sakata, Y.; Matsuda, Y.; Nakagawa, T.; Yasunaga, R.; Imamura, H.; Teramura, K., Remarkable Improvement of the Photocatalytic Activity of Ga_2O_3 Towards the Overall Splitting of H_2O. ChemSusChem **2011**, 4, 181-184.

6. Akatsuka, M.; Kawaguchi, Y.; Itoh, R.; Ozawa, A.; Yamamoto, M.; Tanabe, T.; Yoshida, T., Preparation of Ga_2O_3 Photocatalyst Highly Active for CO_2 Reduction with Water without Cocatalyst. Applied Catalysis B: Environmental **2020**, 262.

7. Ito, R.; Akatsuka, M.; Ozawa, A.; Kato, Y.; Kawaguchi, Y.; Yamamoto, M.; Tanabe, T.; Yoshida, T., Photocatalytic Activity of Ga2o3 Supported on Al2o3 for Water Splitting and CO_2 Reduction. ACS Omega **2019**, 4, 5451-5458.

8. Kikkawa, S.; Teramura, K.; Asakura, H.; Hosokawa, S.; Tanaka, T., Development of Rh-Doped Ga_2O_3 Photocatalysts for Reduction of CO_2 by H_2O as an Electron

Donor at a More Than 300 Nm Wavelength. The Journal of Physical Chemistry C **2018**, 122, 21132-21139.

9. Kim, S.; Oh, S.; Kim, J., Ultrahigh Deep-UV Sensitivity in Graphene-Gated β-Ga_2O_3 Phototransistors. ACS Photonics **2019**, 6, 1026-1032.

10. Guo, D.; Guo, Q.; Chen, Z.; Wu, Z.; Li, P.; Tang, W., Review of Ga_2O_3-Based Optoelectronic Devices. Materials Today Physics **2019**, 11.

11. Li, Q., Enhanced Activity of β-Ga_2O_3 by Substitution with Transition Metal for CO_2 Photoreduction under Visible Light Irradiation. Catalysis Communications **2019**, 120, 23-27.

12. Kudo, A.; Mikami, I., Photocatalytic Activities and Photophysical Properties of $Ga_{2-x}In_xO_3$ Solid Solution. Journal of the Chemical Society, Faraday Transactions **1998**, 94, 2929-2932.

13. Shi, X.; Ueno, K.; Takabayashi, N.; Misawa, H., Plasmon-Enhanced Photocurrent Generation and Water Oxidation with a Gold Nanoisland-Loaded Titanium Dioxide Photoelectrode. The Journal of Physical Chemistry C **2012**, 117, 2494-2499.

14. Ma, X. C.; Dai, Y.; Yu, L.; Huang, B. B., Energy Transfer in Plasmonic Photocatalytic Composites. Light Sci Appl **2016**, 5, e16017.

15. Wu, K.; Chen, J.; McBride, J. R.; Lian, T., Charge Transfer. Efficient Hot-Electron Transfer by a Plasmon-Induced Interfacial Charge-Transfer Transition. Science **2015**, 349, 632-5.

16. Shi, X.; Ueno, K.; Oshikiri, T.; Sun, Q.; Sasaki, K.; Misawa, H., Enhanced Water Splitting under Modal Strong Coupling Conditions. Nat Nanotechnol **2018**, 13, 953-958.

17. Johnson, P. B.; Christy, R. W., Optical Constants of the Noble Metals. Physical Review B **1972**, 6, 4370-4379.

18. Bera, S.; Lee, J. E.; Rawal, S. B.; Lee, W. I., Size-Dependent Plasmonic Effects

of Au and Au@SiO_2 Nanoparticles in Photocatalytic CO_2 Conversion Reaction of Pt/TiO_2. Applied Catalysis B: Environmental **2016**, 199, 55-63.

19. Singh, M. P.; Strouse, G. F., Involvement of the Lspr Spectral Overlap for Energy Transfer between a Dye and Au Nanoparticle. J Am Chem Soc **2010**, 132, 9383-9391.

20. Manjavacas, A.; Liu, J. G.; Kulkarni, V.; Nordlander, P., Plasmon-Induced Hot Carriers in Metallic Nanoparticles. ACS Nano **2014**, 8, 7630-7638.

21. Sundararaman, R.; Narang, P.; Jermyn, A. S.; Goddard, W. A., 3rd; Atwater, H. A., Theoretical Predictions for Hot-Carrier Generation from Surface Plasmon Decay. Nat Commun **2014**, 5, 5788.

Chapter 3

Improvement of Plasmon Induced Photocurrent Generation on Au-NPs/Ga_2O_3 Based on Interfacial Modification by TiO_2 layer

3.1 Introduction

The photocurrent generation on SC-Ga_2O_3 has been achieved by the load of Au-NPs based on the LSPR induced hot carrier generation and separation in the visible region without changing the negative CB potential of Ga_2O_3.[1] Hot electrons injected into the CB of Ga_2O_3 could take part in the H_2 generation, while holes remained in the Au-NPs could oxidize water to generate O_2.[2-3] Although photocurrent generation was obtained in visible light on Au-NPs/SC-Ga_2O_3 photoanode in chapter 2, the photo energy conversion performance should be further improved. For plasmon-induced PEC systems, it is required to efficiently achieve water oxidation which is a rate-determining step. For the prober reason that the holes captured by the formation of OH and H^+ are slow because of a large potential need for water oxidization,[4-5] large numbers of holes remained at the interface would increase the recombination chances with hot electrons.[6] Interface between Au-NPs and Ga_2O_3 plays an important role during the separation of plasmon-induced carriers. As a result, the semiconductor with surface conditions that own excellent holes capture ability is required to modify the interfacial condition between Au-NPs and Ga_2O_3.

Recently, our team has demonstrated that in the case of $SrTiO_3$, water oxidation induced by the plasmon effect is highly sensitive to the surface states of the crystal facets.[7] Au-NPs loaded $SrTiO_3$ with a crystal facet that is terminated with TiO_2 layer exhibits good oxidation ability. In addition, Murakoshi *et al*. also reported that TiO_2

was beneficial for water oxidation by studying the intermediate species during plasmon-induced oxygen evolution.[8] Therefore, it is an effective way to improve the water oxidation ability of Au-NPs/Ga_2O_3 system by enhancing the hole-trapping ability at the interface of the Au-NPs/Ga_2O_3 based on the surface states of TiO_2.

Herein, an interfacial modification was proposed to improve the water oxidation reaction of the Au-NPs/Ga_2O_3 photoelectrode using a thin TiO_2 layer. To optimize the PEC performance, the deposition position of TiO_2 in the structure of Au-NPs/Ga_2O_3 was studied. Nanometre-scale TiO_2 thin film was deposited on the interface of Au-NPs/Ga_2O_3 by the ALD. Monitoring the photocurrent of the PEC reaction was applied to evaluate the photocatalytic reactivity. Due to the excellent hole-trapping ability of the TiO_2 thin film, when the Au-NPs were partially inlaid by TiO_2, the plasmon-generated holes could be efficiently trapped by the surface states at the interfacial boundary between the Au-NPs and TiO_2 layer, which successfully enhanced the water oxidation reactivity of the Au-NPs/Ga_2O_3 photoelectrode.

3.2 Experiment Methods and Characterization

3.2.1 TiO_2 modified Au-NPs/SC-Ga_2O_3 photoanode fabrication and structure characterization

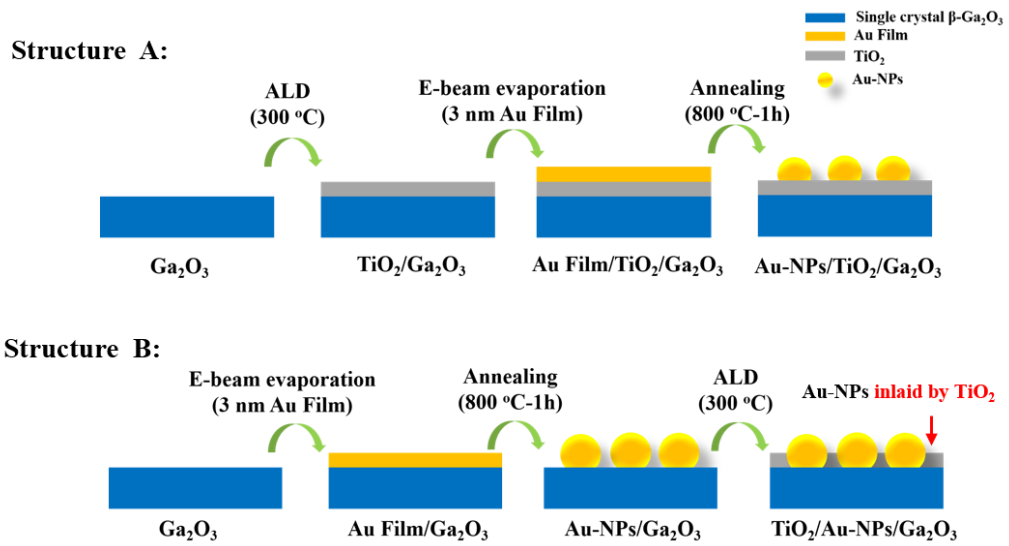

Figure 3.1 Schematics of the fabrication of Au-NPs/TiO_2/SC-Ga_2O_3 (structure A) and TiO_2/Au-NPs/SC-Ga_2O_3 (structure B).

As shown in the schematics in Figure 3.1, 3-nm Au film was deposited onto the substrates by e-beam evaporation at room temperature. The pressure of the deposition chamber before growth is around 2.0×10^{-6} Pa and the evaporation rate was set at around 0.15 Å/s. The TiO_2 layer with different thicknesses was deposited on the surface of Au NPs/Ga_2O_3 substrates by ALD under 300 °C using $TiCl_4$ and deionized water vapor as the Ti and O source with N_2 as the carrier gas and purge gas. Pulse time and purge time as set as 0.1 and 4 s, respectively.

In structure A, the TiO_2 layer was deposited by ALD before the load of Au-NPs by annealing 3 nm Au film on SC-Ga_2O_3. So the TiO_2 layer was located between Au-NPs and SC-Ga_2O_3 in structure A. While in structure B, Au-NPs were first loaded on the surface of Ga_2O_3 following by the deposition of a TiO_2 layer by ALD. Au-NPs were partially inlaid by TiO_2 layer in structure B. The thickness of TiO_2 was controlled by the deposition cycles with a deposition rate of 0.05 nm per cycle. The phase structure of Ga_2O_3 was checked by X-Ray diffraction (RIGAKU RINT-2000/PC) using Cu Kα

radiation. X-ray photoelectron spectrometer (XPS, JPS-9200, JEOL) was used to detect the valence of O, Ti and Ga.

3.2.2 Optical properties and morphology characterization

Optical reflectance and transmittance spectra were measured by a photonic multichannel analyzer (PMA C7473; Hamamatsu Photonics) system operated within the wavelength range of 400-900 nm. The morphology of annealed Au nanoparticles on Ga_2O_3 with different TiO_2 thickness is identified by the field-emission scanning electron microscopy (FE-SEM, JSM-6700FT, JEOL) with a maximum resolution of 1 nm. HR-TEM (JEOL ARM (200F) 200 kV FEG-STEM/TEM) with a resolution of 75 pm at an electron accelerating voltage of 200 kV was applied to check the cross-section of modified samples. Tauc plots calculated based on the transmittance spectra obtained by A UV-Vis spectrophotometer (UV-3100PC, SHIMADZU) were applied to estimate the bandgap of SC-Ga_2O_3. The surface morphology was identified by field-emission scanning electron microscopy (FE-SEM, JSM-6700FT, JEOL) with a maximum resolution of 1 nm. Additionally, ImageJ software was used to analyse the average particle size.

3.2.3 Photoelectrochemical measurement

The photocurrent and I-V curves were measured by the typical three-electrode PEC system as described in the previous chapter. The energy generated under light irradiation at 600 nm on the Ga_2O_3 photoanode, η_{photo}, was evaluated by being compared to an ideally nonpolarizable dark electrode as expressed in the formula:

$$\eta_{photo} = \frac{I_{max}(1.23\ V\ vs\ RHE - V_{max})}{P_{in}} \times 100\ (\%)$$

where I_{max} and V_{max} are the maximum output current and voltage, which generate the maximum electric power, respectively. P_{in} is the incident light intensity. In addition,

Mott-Schottky experiments were carried out at a constant frequency of 5000 Hz in a scan window of -1.5 to 1.0 V vs. SCE in the three-electrode system described above.

3.3 Results and Discussion

3.3.1 Effect of TiO_2 deposition position on the PEC performance of Au-NPs/SC-Ga_2O_3

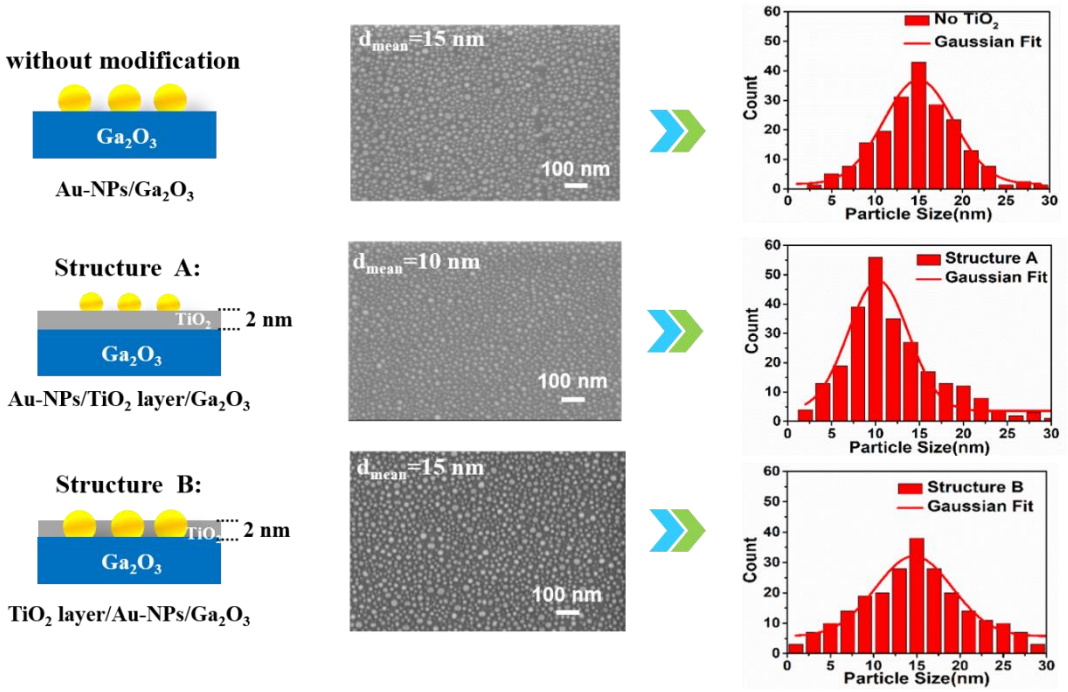

Figure 3.2 SEM and statistics size of Au-NPs on SC-Ga_2O_3 that was modified by 2 nm TiO_2 at different position.

In order to investigate the most suitable deposition position of TiO_2, 2 nm TiO_2 was deposited at different positions as shown in Figure 3.2. In structure A, the 2 nm TiO_2 layer was first deposited on the surface of Ga_2O_3 before the annealing process, so the Au-NPs were fully exposed to the air on the surface of TiO_2. While in structure B, the contact between Au-NPs and Ga_2O_3 was not changed and the Au-NPs were partially inlaid by a 2 nm TiO_2 layer. The morphology of Au-NPs showed obvious differences

in these two structures as shown in the SEM in Figure 3.2. When the Au-NPs were partially inlaid by the TiO_2 layer in structure B, the average particle size was around 15 nm which was almost the same as the Au-NPs without modification indicating that the final deposition of TiO_2 layer did not affect the morphology of Au-NPs. However, the particle size of Au-NPs in structure A was only 10 nm which was much smaller than the sample without modification and structure B. It was probably due to the different surface conditions for Au-NPs formation when the Au film was annealing under high temperatures. The difference in Au-NPs morphology would further influence the LSPR properties of Au-NPs as the discussion below.

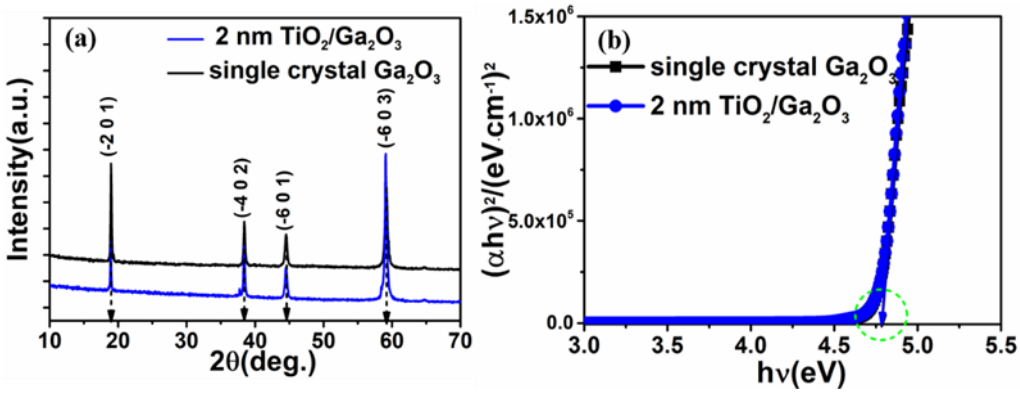

Figure 3.3 (a) XRD of SC-Ga_2O_3 with and without TiO_2 (2 nm); (b) Tauc plots of SC-Ga_2O_3 with and without TiO_2 (2 nm) calculated from the UV-Vis spectra.

Next, we checked the phase structure of Ga_2O_3 before and after the deposition of TiO_2. All the peaks in XRD result measured from 10° to 70° shown in Figure 3.3a are attributed to the diffraction peaks of β-Ga_2O_3.[9] No peaks shifting and broadening of Ga_2O_3 were observed after the deposition of TiO_2. Figure 3.3b shows the profile of $(\alpha hv)^2$ versus hv for the single crystal Ga_2O_3 with and without TiO_2 (2 nm) which is related to the equation:

$$\alpha hv = A(hv - E_g)^n$$

where A is a constant, n=1/2 for direct bandgap semiconductor, α is the absorption coefficient calculated by the transmittance, h is the Planck constant, v is the light frequency.[10] The E_g were estimated from the x-intercept of Figure 3.3b. It could be found that the bandgap (4.8 eV) of Ga_2O_3 estimated from the Tauc plots in Figure 3.3b kept the same before and after the deposition of 2 nm TiO_2.

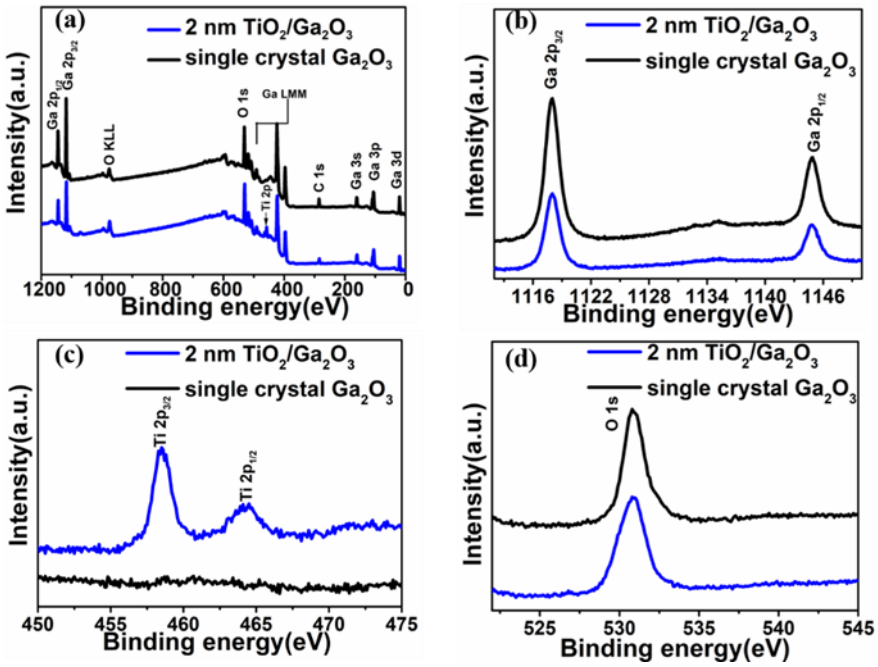

Figure 3.4 XPS spectra of SC-Ga_2O_3 with and without 2 nm TiO_2: (a) full survey spectra; (b) core level spectra for Ga 2p; (c) core level spectra for Ti 2p; (d) core level spectra for O 1s.

The elements' oxidation states were also measured by XPS as shown in Figure 3.4. The symmetrical peaks of Ga $2p_{1/2}$ at 1144.5 eV and Ga $2p_{3/2}$ at 1117.9 eV in Figure 3.4b were attributed to the Ga^{3+} in Ga_2O_3.[11] It was found in Figure 3.4c that two peaks of Ti $2p_{3/2}$ and Ti $2p_{1/2}$ at binding energies of 458.6 eV and 464.4 eV were observed after the deposition of TiO_2 indicating the presence of Ti^{4+} in TiO_2. It demonstrated that the TiO_2 was deposited on the Ga_2O_3.[12] Additionally, there were no changes in the binding energy and width of Ga 2p after the deposition of TiO_2. For the O 1s shown in

Figure 3.4d, a slight broadening at lower energy was observed without shifting of peak energy, resulting from the presence of O 1s peak of Ti-O (529.8 eV).[13] Based on the results above, it could be concluded that the crystal phase, band structure of Ga_2O_3 did not change after the deposition of TiO_2.

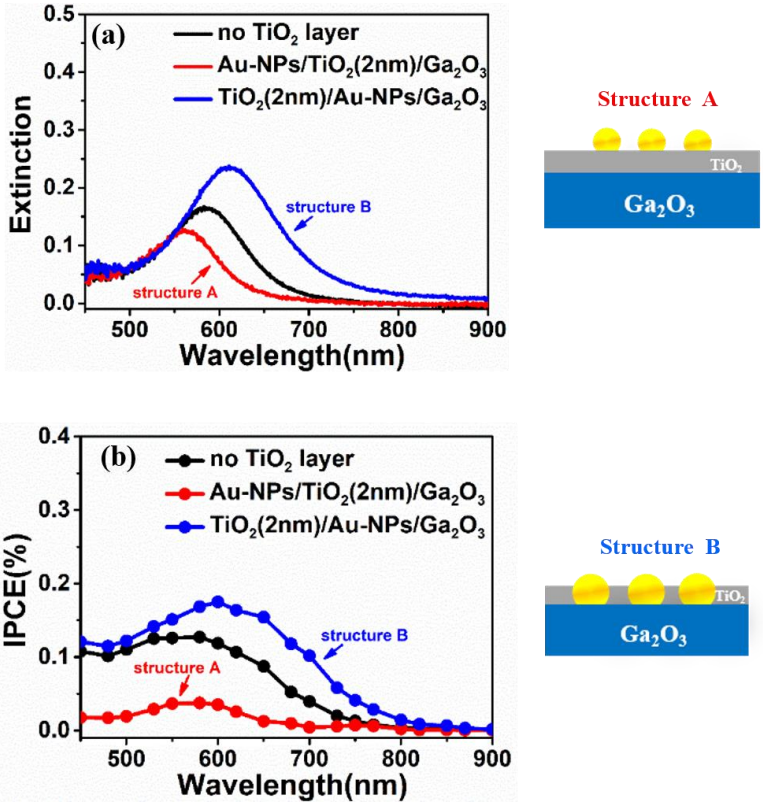

Figure 3.5 (a) Extinction spectra and (b) IPCE spectra of Au-NPs/SC-Ga_2O_3 (black), Au-NPs/TiO_2/SC-Ga_2O_3 (red) and TiO_2/Au-NPs/SC-Ga_2O_3 (blue).

As the Au-NPs showed different morphology in the two modification structures, correspondingly, the blue shift and weaker intensity of LSPR resonance wavelength in structure A compared with the Au-NPs/SC-Ga_2O_3 is due to the decrease of particle size shown in Figure 3.5a.[14] As the resonance position of noble metal nanoparticles showed a negative relation with the dielectric constant, samples using structure B had a redshift and higher intensity as a result of the refractive index increment of the

surrounding media from TiO_2.[15] Moreover, we compared the PEC performance of samples with and without interfacial modification in Figure 3.5b. The application of the TiO_2 layer between Au-NPs and Ga_2O_3 dramatically decreases the IPCE to one-third of the value without TiO_2. In contrast, it could be seen from the blue plot in Figure 3.5b that structure B showed an obvious improvement in photoelectrochemical conversion performance compared with the pure Au-NPs/Ga_2O_3 without modification.

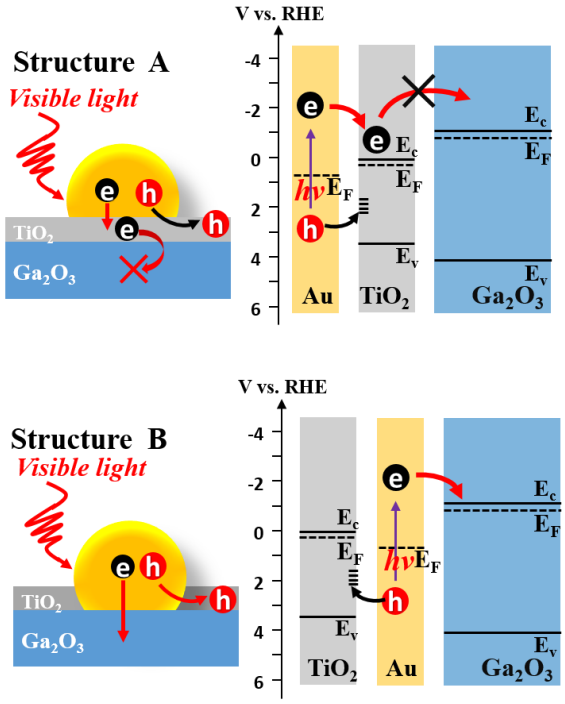

Figure 3.6 Schematic diagram of charge carrier transfer in Au-NPs/Ga_2O_3 with different TiO_2 layer modification position.

We speculated that, as shown in Figure 3.6, upon LSPR decay hot electrons in structure A would first be captured by the TiO_2 layer which is difficult for these hot electrons to transfer to Ga_2O_3 as a result of the more negative CB of Ga_2O_3 than TiO_2.[16] In addition, as discussed in the previous chapter, the lower LSPR intensity would also decrease the IPCE. Therefore, the application of a TiO_2 layer using

structure A has a poisonous effect on the PEC performance which makes the IPCE much lower. On the contrary, the contact between Au and Ga_2O_3 using structure B was not changed so that the electrons could be transferred to the CB of Ga_2O_3 smoothly and the holes were captured by the defective states at the TiO_2 interface decreasing the recombination. Therefore, structure B showed a much better performance compared with structure A. With this structure, the plasmon-generated electrons could transfer from Au-NPs to Ga_2O_3 at the interface of Au-NPs/Ga_2O_3, and the hot holes could be captured at the surface states of TiO_2, which might accelerate the water oxidation reaction.

3.3.2 Effect of TiO_2 thickness on the PEC performance of Au-NPs/SC-Ga_2O_3

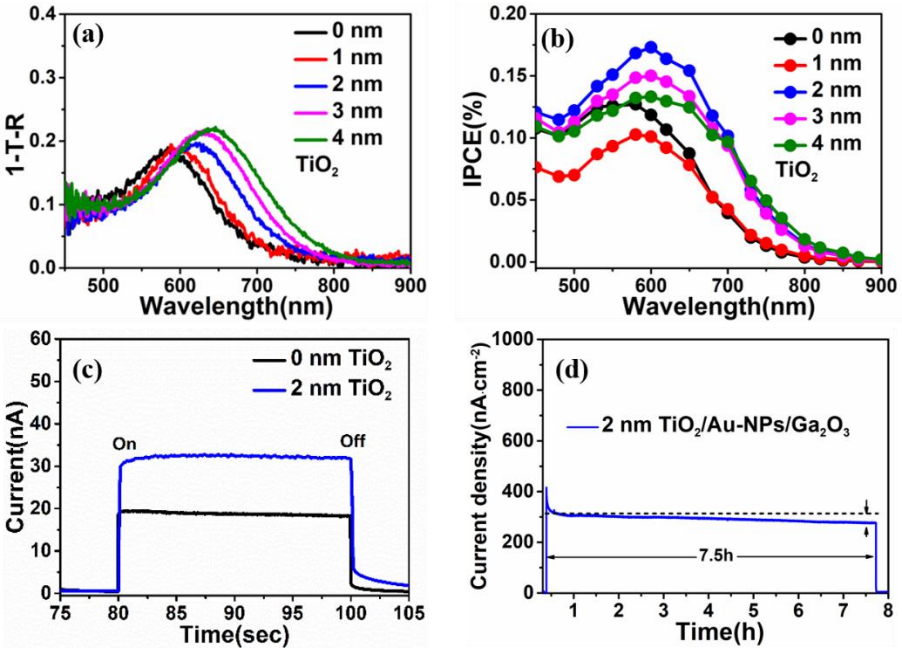

Figure 3.7 (a) Absorption spectra and (b) IPCE action spectra of Au-NPs/Ga_2O_3 modified with different thicknesses of TiO_2. (c) *I-t* characteristics Au-NPs/Ga_2O_3 with 0 and 2 nm TiO_2 under 600 nm irradiation; (d) Current density-time curve of 2-nm-TiO_2/Au-NPs/Ga_2O_3 under 600 nm light irradiation. The measurement conditions were identical to the photocurrent measurements in experiment section. The dash line meant the initial value of quasi-steady current density.

The absorption spectrum of Au-NPs was shown in Figure 3.7a which was calculated as the difference between the (1-T-R) spectrum substrate with Au-NPs and without Au-NPs, where R and T are the reflection and transmission, respectively. With the thickness of TiO_2 increasing, a redshift of the peak position of the LSPR band from 585 to 645 nm was observed. Due to the similar particle size and distribution of Au-NPs with different thicknesses of TiO_2, the redshift was mainly owing to the refractive index increase in the surrounding media after TiO_2 deposition.[15] In addition, the absorption value at the LSPR peak also increased as the thickness of the TiO_2 layer increased at a wavelength longer than 550 nm. In contrast, the almost same absorption at wavelengths shorter than 550 nm was only due to the interband transition of Au.[2] The PEC performance of these samples modified by different thicknesses of TiO_2 is presented in Figure 3.7b. When 1 nm TiO_2 layer was deposited, the IPCE was decreased compared with the Au-NPs/Ga_2O_3. Continue to increase the TiO_2 thickness to 2-4 nm, an obvious IPCE increase in all the TiO_2/Au-NPs/Ga_2O_3 photoelectrodes was presented in the visible region compared with that of the Au-NPs/Ga_2O_3 photoelectrode. It was noticeable that Au-NPs/Ga_2O_3 modified by 2 nm TiO_2 showed the maximum IPCE value, which achieved 0.17% at approximately 600 nm. Figure 3.7c showed the stable photocurrents of Au-NPs/Ga_2O_3 with and without 2 nm TiO_2 under 600 nm irradiation. The photocurrent of 2-nm-TiO_2/Au-NPs/Ga_2O_3 was approximately 1.5 times larger than that of Au-NPs/Ga_2O_3 without modification. The photocurrent after 7.5 hours irradiation maintained 90% of the initial value of quasi-steady photocurrent, indicating a good stability of 2-nm-TiO_2/Au-NPs/Ga_2O_3, as shown in Figure 3.7d. Based on the results above, it demonstrated that the interfacial modification by TiO_2 had an effective positive effect on improving the PEC performance of Au-NPs/Ga_2O_3 under visible light.

Furthermore, it should be noted that after the deposition of 2 nm TiO_2, the IPCE peak of 2-nm-TiO_2/Au-NPs/Ga_2O_3 was increased 1.5 times compared with pristine Au-NPs/Ga_2O_3. However, the absorption was increased by only 1.1 times at the peak LSPR wavelength. We suspected that it is mainly because of much better charge separation occurring at the interface of Au-NPs and Ga_2O_3, which originated from the good holes-capturing ability of TiO_2, as depicted in Figure 3.6. After the deposition of TiO_2, the plasmon-induced holes were captured efficiently by the surface states of TiO_2 for efficient water oxidation. Therefore, the hot electrons generated at the Au-NPs/Ga_2O_3 interface could be smoothly transferred to the CB of Ga_2O_3 due to the direct contact between Au and Ga_2O_3.

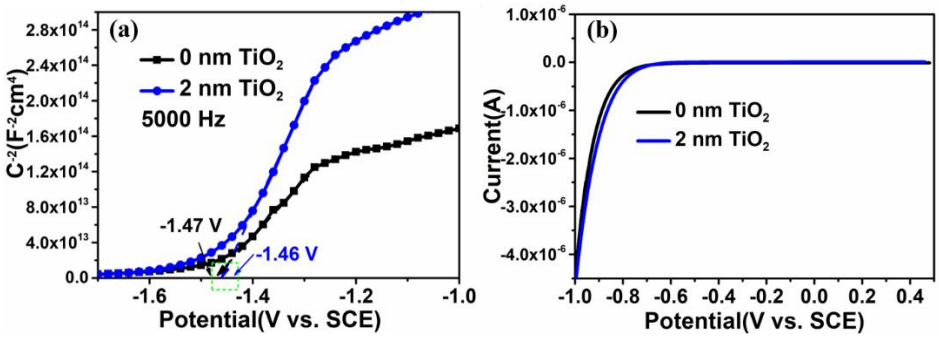

Figure 3.8 (a) A typical Mott–Schottky plot of Au-NPs/Ga_2O_3 without TiO_2 modification. (b) *I-V* characteristics of 2-nm-TiO_2/Au-NPs/Ga_2O_3 and Au-NPs/Ga_2O_3 measured in dark condition.

Based on the mechanism mentioned above, hot carriers should have enough energy to achieve the hot-electron injection and water oxidation. According to the Mott-Schottky measurement in Figure 3.8a, the flat-band potential of Au-NPs/Ga_2O_3 is estimated to be -1.47 V (vs. SCE at pH 7). Thus, the flat-band potential of Au-NPs loaded Ga_2O_3 could be concluded to be -0.81 V (vs. RHE) by the following formula[17]:

$$E\,(\mathrm{RHE}) = E\,(\mathrm{SCE}) + 0.244 + 0.059\times\mathrm{pH}$$

After the deposition of TiO_2, the flat-band potential shows a positive shift to -0.80 V

vs. RHE which is consistent with the onset potential shift in the I-V result shown in Figure 3.8b. Thus, to achieve both hot-electron injection and water oxidation simultaneously, irradiation energy should be larger than the energy barrier between the flat-band potential of Ga_2O_3 for hot-electron injection and the oxidation potential of water (+1.23 V vs. RHE) which is estimated as 2.03 eV (610 nm). As shown in Figure 3.7b, the wavelength of 600 nm is the peak wavelength of the IPCE spectrum with different thicknesses of TiO_2. As a result, the observation that the redshift of IPCE peaks of the TiO_2/Au-NPs/Ga_2O_3 is not such obvious compared with their red shift in the absorption spectra could be explained by the threshold of photon energy needed for exciting electron/hole separation at the Au-NPs/Ga_2O_3 interface.

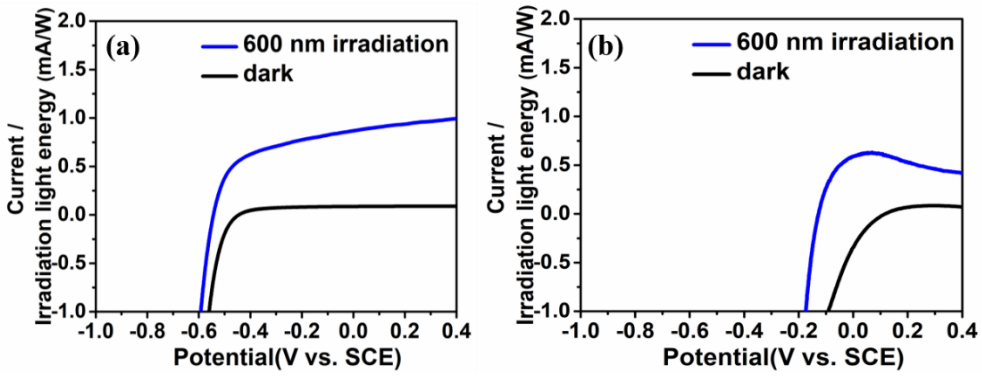

Figure 3.9 *I-V* characteristics of (a) 2-nm-TiO_2/Au-NPs/Ga_2O_3 and (b) Au-NPs on TiO_2 thin film with a thickness of 54 nm with and without light irradiation of the wavelength of 600 nm. The current is normalized by the irradiation light energy.

It could be found that the flat-band potential, for n-type semiconductors, as well as the CB potential is very negative. It suggested that the electron that was injected into the CB of Ga_2O_3 owned a highly negative potential energy. We compared the energy generated under light irradiation at 600 nm on the Ga_2O_3 and TiO_2 photoanode, η_{photo} which is the thermodynamic energy-conversion efficiency of the photoelectrode.[18] For 2-nm-TiO_2/Au-NPs/Ga_2O_3, the η_{photo} value under light irradiation at 600 nm was 0.06%

from the *I-V* characteristics shown in Figure 3.9a. However, the η_{photo} of Au-NPs/TiO_2-thin film was 0.03%, which was just half of that of TiO_2/Au-NPs/Ga_2O_3. This is mainly because the Au-NPs/TiO_2-thin film had an extremely negative onset potential. Therefore, the plasmonic Ga_2O_3 photoanode modified with the thin TiO_2 layer could simultaneously achieve water oxidation and hot-electron injection with a negative reduction potential under visible light irradiation.

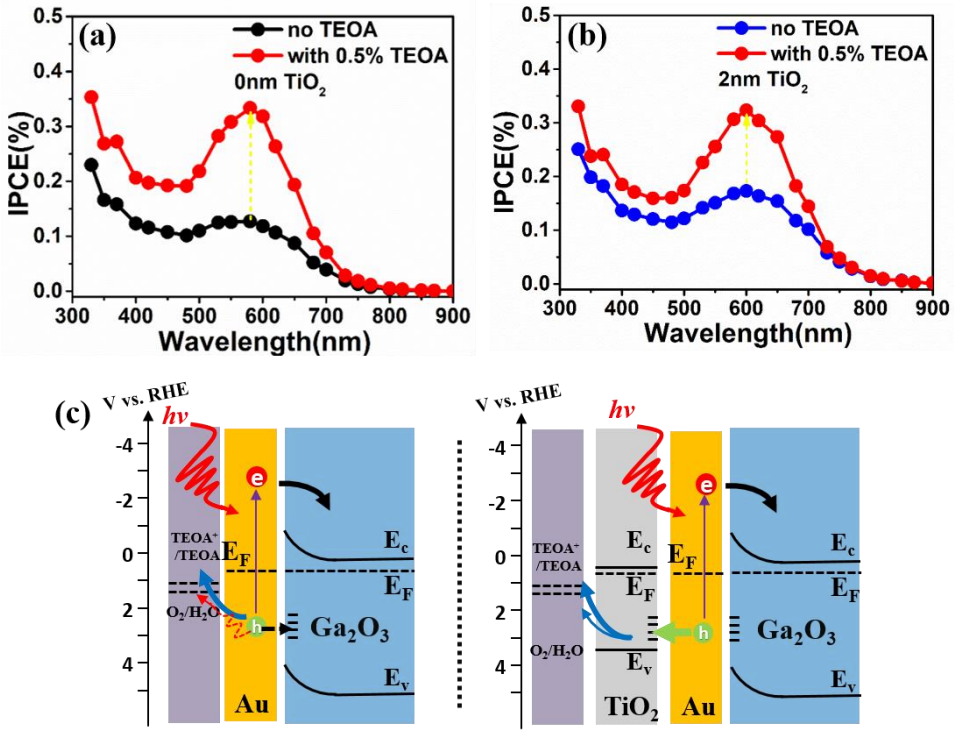

Figure 3.10 IPCE action spectra of (a) Au-NPs/Ga_2O_3 and (b) 2-nm-TiO_2/Au-NPs/Ga_2O_3 measured in a $KClO_4$ aqueous solution with and without TEOA. (c) Schematics of plasmon-induced charges transfer of Au-NPs/Ga_2O_3 and 2 nm-TiO_2/Au-NPs/Ga_2O_3. e and h indicate the electrons and holes, respectively.

To further confirm the holes trapping ability of the TiO_2 layer, triethanolamine (TEOA) was added into the electrolyte in the photocurrent measurement as the sacrificial holes scavengers due to its fast reaction kinetics based on one-electron

oxidation.[19] The IPCE spectrum of 2-nm-TiO_2/Au-NPs/Ga_2O_3 and Au-NPs/Ga_2O_3 measured in the electrolyte with TEOA and the enhancement of IPCE was shown in Figure 3.10a and 3.10b. It was difficult for Au-NPs/Ga_2O_3 without TiO_2 modification to achieve the water oxidation reaction by holes, as discussed above. While the TEOA was added into the electrolyte, the oxidation reactivity was dramatically increased even though the hole-trapping ability of the Ga_2O_3 surface was poor for Au-NPs/Ga_2O_3, as illustrated in Figure 3.10c. The high IPCE of 2-nm-TiO_2/Au-NPs/Ga_2O_3 without TEOA in Figure 3.10b indicated that the hot holes trapped at the surface states of 2-nm-TiO_2/Au-NPs/Ga_2O_3 oxidized water efficiently even without the addition of TEOA, as shown in Figure 3.10d.

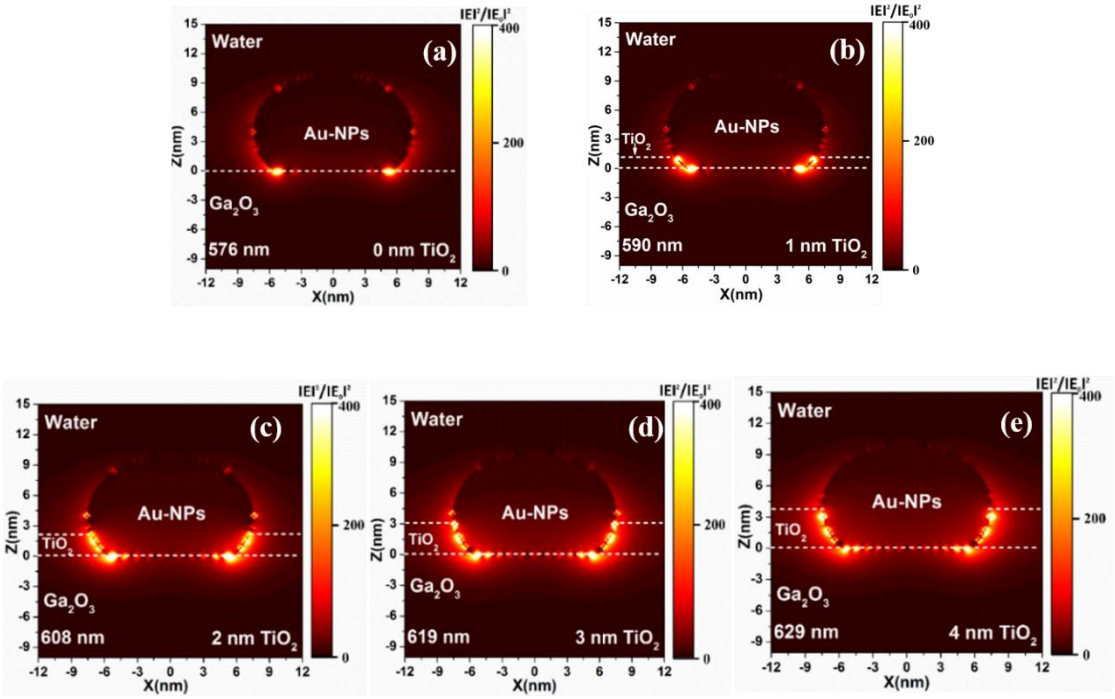

Figure 3.11 Near-field distributions of Au-NPs/Ga_2O_3 modified with (a) 0, (b) 1, (c) 2, (d) 3, and (e) 4-nm TiO_2 layers, which were calculated by an FDTD simulation.

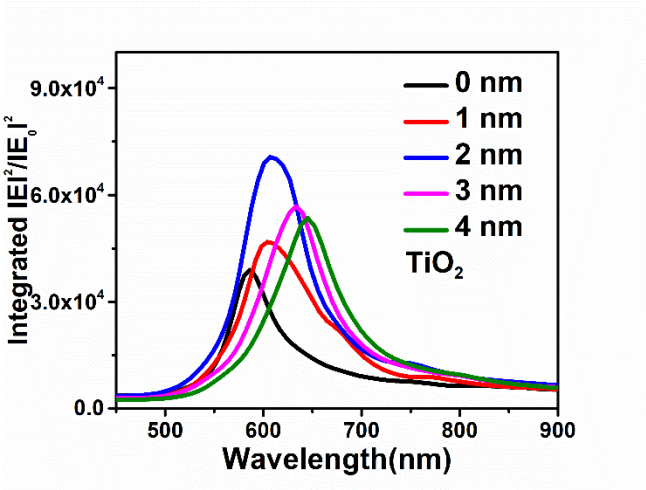

Figure 3.12 Near-field enhancement spectra at interface of Au-NPs/Ga_2O_3 modified with different thickness TiO_2 layers calculated by an FDTD simulation.

To understand the different PEC performance of TiO_2/Au-NPs/Ga_2O_3 with different thicknesses of the TiO_2 layer, we calculated the near-field distribution at the interface of TiO_2/Au-NPs/Ga_2O_3 that determined the plasmon-induced carrier generation by a finite-difference time-domain simulation. When Au-NPs/Ga_2O_3 was not modified by TiO_2, the hot spot of the near-field was located at the interface between Au-NPs and Ga_2O_3 represented by two bright spots in Figure 3.11a. After the deposition of 1 nm TiO_2, although the near field was enhanced, the IPCE was dropped as shown in Figure 3.7a. We speculated that the surface states of TiO_2 was not formed efficiently in 1 nm TiO_2, so that the holes-trapping of 1 nm TiO_2 was not as good as thicker TiO_2. The deposition of TiO_2 deceases the contact between water and Au-NPs/Ga_2O_3 resulting in the reduced IPCE. For 2-nm-TiO_2/Au-NPs/Ga_2O_3, the significantly improved near-field intensity was observed at the three-phase boundary of TiO_2/Au-NPs/Ga_2O_3 (Figure 3.11c). However, when the thickness of TiO_2 layer was further increased to 3 nm and 4 nm as shown in Figure 3.11d and e, the near-field intensity at the three-phase boundary decreased which was consistent with the calculation results in

Figure 3.12 by FDTD. Furthermore, holes trapped at the TiO_2/Au-NPs/Ga_2O_3 boundary should migrate to the surface of TiO_2 taking part in the water oxidation reaction. The increasing distance from the bottom to the surface of TiO_2 in the thick TiO_2 modification case would also harm the migration of holes to the surface of TiO_2 as a result of the extended migration path. Therefore, 2-nm TiO_2 interfacial-modified Au-NPs/Ga_2O_3 showed the best PEC improvement.

3.4 Conclusion

In this chapter, we successfully demonstrated the IPCE of Au-NPs/Ga_2O_3 was further improved by an interfacial modification through the deposition of a TiO_2 layer by the advantage of its good hole-trapping ability. It was beneficial to trap plasmon-induced holes at the interfacial boundary between Au-NPs and Ga_2O_3 by partially inlaying Au-NPs with the TiO_2 layer, leading to improved oxidation reactivity without damage to the efficient electron transfer. The highest IPCE improvement (1.5-times compared with that without TiO_2) in the visible region was obtained in the 2-nm-thick TiO_2 interfacial modification. The thermodynamic energy-conversion efficiency of the 2-nm-TiO_2/Au-NPs/Ga_2O_3 photoelectrode under light irradiation at 600 nm showed almost twice larger than that of the Au-NPs/TiO_2-thin film resulting from the extremely negative onset potential. Based on these, we demonstrated a novel plasmonic photoanode could own both a high ability for reduction, such as H_2 evolution, and oxidation ability for water oxidation based on the negative CB of Ga_2O_3 and the hole-trapping ability of TiO_2, respectively. It is expected that this interfacial modification has huge potential in artificial photosynthesis and could be applied in varied photon energy conversion fields and devices.

3.5 Reference

1. Wang, Y.; Shi, X.; Oshikiri, T.; Zu, S.; Ueno, K.; Misawa, H., Plasmon-Induced Electron Injection into the Large Negative Potential Conduction Band of Ga_2O_3 for Coupling with Water Oxidation. Nanoscale **2020**, 12, 22674-22679.

2. Shi, X.; Ueno, K.; Oshikiri, T.; Sun, Q.; Sasaki, K.; Misawa, H., Enhanced Water Splitting under Modal Strong Coupling Conditions. Nat Nanotechnol **2018**, 13, 953-958.

3. Zhong, Y.; Ueno, K.; Mori, Y.; Shi, X.; Oshikiri, T.; Murakoshi, K.; Inoue, H.; Misawa, H., Plasmon-Assisted Water Splitting Using Two Sides of the Same $SrTiO_3$ Single-Crystal Substrate: Conversion of Visible Light to Chemical Energy. Angew Chem Int Ed Engl **2014**, 53, 10350-10354.

4. Han, L.; Dong, S.; Wang, E., Transition-Metal (Co, Ni, and Fe)-Based Electrocatalysts for the Water Oxidation Reaction. Adv Mater **2016**, 28, 9266-9291.

5. Xie, G.; Zhang, K.; Guo, B.; Liu, Q.; Fang, L.; Gong, J. R., Graphene-Based Materials for Hydrogen Generation from Light-Driven Water Splitting. Adv Mater **2013**, 25, 3820-39.

6. Clavero, C., Plasmon-Induced Hot-Electron Generation at Nanoparticle/Metal-Oxide Interfaces for Photovoltaic and Photocatalytic Devices. Nature Photonics **2014**, 8, 95-103.

7. Shi, X.; Li, X.; Toda, T.; Oshikiri, T.; Ueno, K.; Suzuki, K.; Murakoshi, K.; Misawa, H., Interfacial Structure-Modulated Plasmon-Induced Water Oxidation on Strontium Titanate. ACS Applied Energy Materials **2020**, 3, 5675-5683.

8. Suzuki, K.; Li, X.; Wang, Y.; Nagasawa, F.; Murakoshi, K., Active Intermediates in Plasmon-Induced Water Oxidation at Au Nanodimer Structures on a Single Crystal of TiO_2. ACS Energy Letters **2020**, 5, 1252-1259.

9. Yu, F.-P.; Ou, S.-L.; Wuu, D.-S., Pulsed Laser Deposition of Gallium Oxide Films for High Performance Solar-Blind Photodetectors. Optical Materials Express **2015**, 5, 1240-1249.

10. Coulter, J. B.; Birnie, D. P., Assessing Tauc Plot Slope Quantification: ZnO Thin Films as a Model System. physica status solidi (b) **2018**, 255, 1700393.

11. Shang, Y.; Tang, K.; Chen, Z.; Zhang, Z.; Deng, J.; Hu, Y.; Gu, K.; Cao, M.; Wang, L.; Huang, J., Growth and Characterization of Ta-Doped Ga_2O_3 Films Deposited by Magnetron Sputtering. Materials Science in Semiconductor Processing **2021**, 134, 106040.

12. Bharti, B.; Kumar, S.; Lee, H. N.; Kumar, R., Formation of Oxygen Vacancies and Ti^{3+} State in TiO_2 Thin Film and Enhanced Optical Properties by Air Plasma Treatment. Sci Rep **2016**, 6, 32355.

13. Bagus, P. S.; Nelin, C. J.; Brundle, C. R.; Lahiri, N.; Ilton, E. S.; Rosso, K. M., Analysis of the Fe 2p XPS for Hematite Alpha Fe_2O_3: Consequences of Covalent Bonding and Orbital Splittings on Multiplet Splittings. J Chem Phys **2020**, 152, 014704.

14. Sonnichsen, C.; Franzl, T.; Wilk, T.; von Plessen, G.; Feldmann, J.; Wilson, O.; Mulvaney, P., Drastic Reduction of Plasmon Damping in Gold Nanorods. Phys Rev Lett **2002**, 88, 077402.

15. DeSantis, C. J.; Skrabalak, S. E., Size-Controlled Synthesis of Au/Pd Octopods with High Refractive Index Sensitivity. Langmuir **2012**, 28, 9055-62.

16. Navarrete, M.; Cipagauta‐Díaz, S.; Gómez, R., Ga_2O_3/TiO_2 Semiconductors Free of Noble Metals for the Photocatalytic Hydrogen Production in a Water/Methanolmixture. Journal of Chemical Technology & Biotechnology **2019**, 94, 3457-3465.

17. Wang, M.; Chang, Y. S.; Tsao, C. W.; Fang, M. J.; Hsu, Y. J.; Choy, K. L., Enhanced Photoelectrochemical Hydrogen Generation in Neutral Electrolyte Using Non-Vacuum Processed CIGS Photocathodes with an Earth-Abundant Cobalt Sulfide Catalyst. Chem Commun (Camb) **2019**, 55, 2465-2468.

18. Coridan, R. H.; Nielander, A. C.; Francis, S. A.; McDowell, M. T.; Dix, V.; Chatman, S. M.; Lewis, N. S., Methods for Comparing the Performance of Energy-Conversion Systems for Use in Solar Fuels and Solar Electricity Generation. Energy & Environmental Science **2015**, 8, 2886-2901.

19. Pellegrin, Y.; Odobel, F., Sacrificial Electron Donor Reagents for Solar Fuel Production. Comptes Rendus Chimie **2017**, 20, 283-295.

Chapter 4

Improved Water Splitting Efficiency of Au-NPs loaded Ga_2O_3 Thin Film in Visible under Strong Coupling Condition

4.1 Introduction

In previous chapters, we have demonstrated that, based on the LSPR effect and interfacial modification by TiO_2, TiO_2/Au-NPs/SC-Ga_2O_3 could achieve the generation of photocurrent in visible region.[1] However, the irradiated visible light could not be efficiently absorbed by a single layer Au-NPs on Ga_2O_3. Further improvement in light absorption is required to improve the photoelectrochemical conversion efficiency.

Our team has demonstrated a TiO_2 photoelectrode based on the modal strong coupling system between the LSPR mode of Au-NPs and Fabry-Pérot (F-P) cavity mode generated in very thin TiO_2 film deposited on Au film.[2] When the resonance wavelength of the F-P cavity was almost identical to LSPR, strong coupling with two new hybrid states was generated as indicated in Figure 4.1a, resulting in the improvement of light absorption and PEC conversion efficiency using water as an electron source.

Based on this concept, in this study, we fabricated a novel photoanode with a structure of TiO_2/Au-NPs/Ga_2O_3/titanium nitride (TiN)/Au-film (TAGA) with high reduction ability shown in Figure 4.1b under modal coupling conditions to improve the light absorption and performance in solar-driven water splitting under the visible irradiation. During the deposition of β-Ga_2O_3, a high deposition temperature is necessary to obtain the crystal phase of β-Ga_2O_3 owning excellent photocatalytic properties.[3] However, the stable deposition of β-Ga_2O_3 on Au-film under such high

deposition temperature was difficult. Thus, a new method was developed by depositing a thin TiN layer on Au film to improve the electrochemical property of Ga_2O_3 on Au film under high temperatures. Based on this method, a nanocavity was fabricated by depositing Ga_2O_3 film on TiN/Au-film at 600 ^oC successfully. The important role of partial inlaying of Au-NPs by TiO_2 layer was also confirmed which could improve the coupling strength and the charge separation of the hot carriers efficiently. Using the TAGA photoelectrode with modal strong coupling, water splitting was successfully achieved at zero bias potential under visible light irradiation, suggesting that this photoanode could help reduce substances requiring a negative CB potential higher than water.

4.2 Experiment Methods and Characterization

4.2.1 Fabrication of TAGA photoanode and characterization

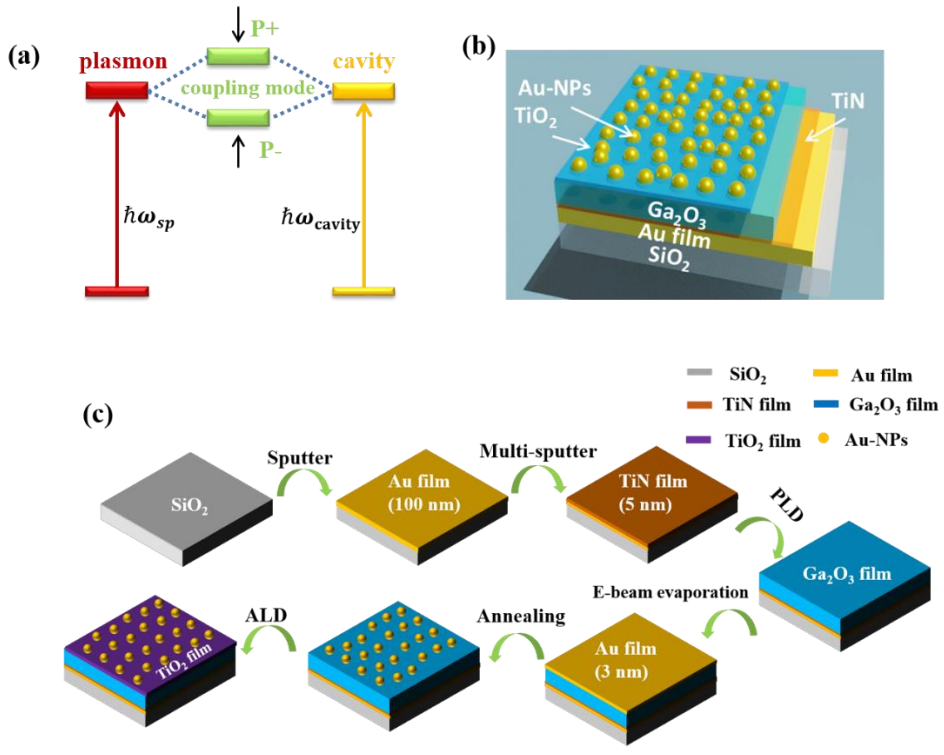

Figure 4.1 (a) Schematic diagram of energy splitting in strong coupling between the optical cavity

and LSPR of Au-NPs. ω_{sp} and ω_{cavity} represent the angular frequency of LSPR and cavity resonance, respectively; (b) Schematic diagram of TAGA structure; (c) Schematic of TAGA fabrication.

As shown in Figure 4.1c, 100 nm Au film was deposited by helicon sputtering (ULVAC, MPS-4000C1/HC1) on silica glass (SiO_2) with the size of 10×10×0.5 mm^3 which was rinsed with acetone and methanol under an ultrasonic bath for 5 min, respectively. Subsequently, the ultra-thin TiN layer (5 nm) was deposited on Au film. Sn doped β-Ga_2O_3 target used in pulsed laser deposition (PLD, PAC-LMBE) was fabricated by sintering mixture powder consisting of SnO_2 and β-Ga_2O_3 (Sn mole concentration of 0.5%) under 1400 ºC for 10 hours. Sn-doped β-Ga_2O_3 films with different thicknesses were deposited on the TiN/Au-film/SiO_2 substrate by controlling the pulse numbers under 600 ºC with an oxygen pressure of 0.1Pa. Laser energy and pulse frequency was set as 60 mJ and 5 Hz. To prevent the thin TiN film from oxidation, Ga_2O_3 film with a pulse number of 3000 was first deposited on TiN under the vacuum of 10^{-5} Pa without the introduction of oxygen. Then Au-NPs were loaded by annealing 3 nm Au film deposited by electron-beam evaporation (EIKO Engineering, EB-580S) on β-Ga_2O_3 film. The annealing temperature and duration time was 400 ºC and 2 hours, respectively. Finally, Au-NPs on Ga_2O_3 were inlaid by a 4 nm TiO_2 layer using a commercial hot-wall flow-type ALD reactor (SUNALETM R series, Picosun, Finland) under 300 ºC.

The phase structure of Sn-doped β-Ga_2O_3 powders and Ga_2O_3 films was investigated by X-ray diffraction (XRD, RIGAKU RINT-2000/PC) using Cu Kα radiation. Field-emission scanning electron microscopy (FE-SEM, JSM-6700FT, JEOL) with a maximum resolution of 1 nm was applied to identify the top-view morphology of TAGA. Optical reflectance and transmittance spectra were obtained by

a photonic multichannel analyser (PMA C7473, Hamamatsu Photonics) and spectroscopic reflectometer (Filmetrics, F20-UV). A UV-Vis spectrophotometer (UV-3100PC, SHIMADZU) was applied to measure the transmittance of Ga_2O_3 of film on sapphire and to estimate the optical bandgap by the Tauc plots.

4.2.2 Photoelectrochemical measurement

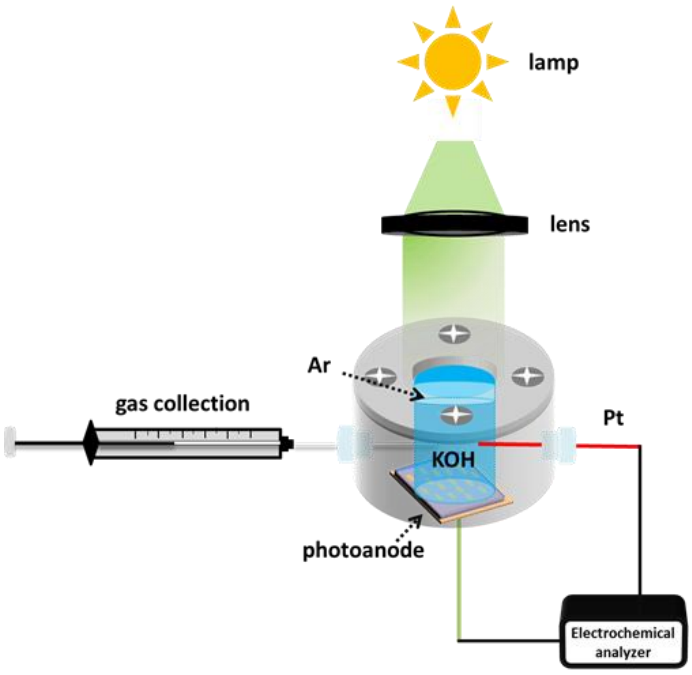

Figure 4.2 Schematic of O_2 evolution using TAGA in a two-electrode system.

Before the PEC measurement, the backside and sidewall of samples were coated by In-Ga alloy with a weight ratio of 4:1 to form an ohmic contact with the samples. Then the samples were connected to a copper plate in a Teflon reaction cell which has a pinhole with a diameter of 2.0 mm on the lid. Subsequently, this cell was connected to an electrochemical analyser (ALS/CH Instruments 852C, ALS) with a copper lead wire using a three-electrode system to measure the PEC performance. A platinum wire, a saturated calomel electrode (SCE) and 0.1M KOH aqueous solution were the counter electrode, reference electrode and electrolyte, respectively. During the *I-t*

measurement, a potential of + 0.3 V vs. SCE was applied to the working photoanode under the illumination of the Xe lamp. The IPCE was calculated by the formula in previous chapters.

A two-electrode system was applied to carry out the water splitting in our study in which the TAGA samples and Pt wire were the working electrode and counter electrode, respectively. To estimate the O_2 evolution amount from the oxidation of water determined by gas chromatography-mass spectrometry, 0.1M KOH aqueous prepared by the isotope and pure water (volume ratio $H_2{}^{18}O$: $H_2{}^{16}O$=1:6) was used as the electrolyte. Faraday efficiency was calculated according to the O_2 and total charge amount.

4.2.3 Numerical simulations

Finite-difference time-domain method (FDTD Solutions, Lumerical) was applied to calculate the near-field distribution and intensity. The plane beam with linear polarization is illuminated on the sample in normal incidence. The investigated structure was simulated using perfectly matched layers along the z-direction and periodic boundary conditions along the x-and y-directions with a period of 20 nm. The Au-NPs were simulated by the model of an ellipsoid sphere with a diameter of 15 nm, 15 nm and 10 nm in the x, y and z directions, respectively. In the simulation, the refractive index of Au was taken from the data of Johnson and Christy. The mesh size was set as 0.02 nm. Ga_2O_3 and TiO_2 were treated as dielectric materials with refractive indices of 1.9 and 2.4, respectively. In the near-field spectra simulation, the monitor was placed 1 nm above the interface of Au-NPs/Ga_2O_3. E and E_0 mean the electric field of the plasmonic field and incident light.

4.3 Results and Discussion

4.3.1 Fabrication of crystal phase of β-Ga_2O_3 film

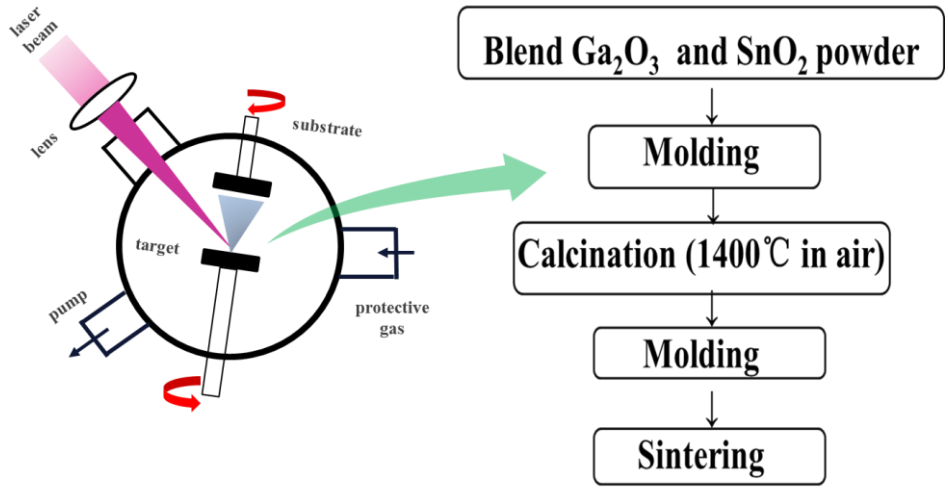

Figure 4.3 Schematics of PLD and fabrication of Sn doped Ga_2O_3 target.

To construct the optical nanocavity, a thin film should be deposited on the reflective layer. Therefore, Ga_2O_3 thin film with good optical and electric properties was the first factor that should be considered. In this study, PLD was employed to deposit the Ga_2O_3 thin film because of the advantages of stoichiometry transfer between target and substrate, high vacuum, tunable film properties, etc.[4] The SnO_2 doped Ga_2O_3 target was fabricated by sintering the molded mixture powder under high temperature shown in the experimental section and the schematic in Figure 4.3. To overcome the poor conductivity of pure Ga_2O_3, during the fabrication of the target, SnO_2 was applied to dope the powder. When the Sn^{4+} with a similar size to the Ga^{3+} was doped into the lattice of Ga_2O_3, the position of Ga^{3+} in the lattice would be occupied by Sn^{4+} resulting in the formation of a shallow donor energy level.[5] As a result, the charge density and conductivity could be improved and the Sn-doped Ga_2O_3 would exhibit n-type conductivity.

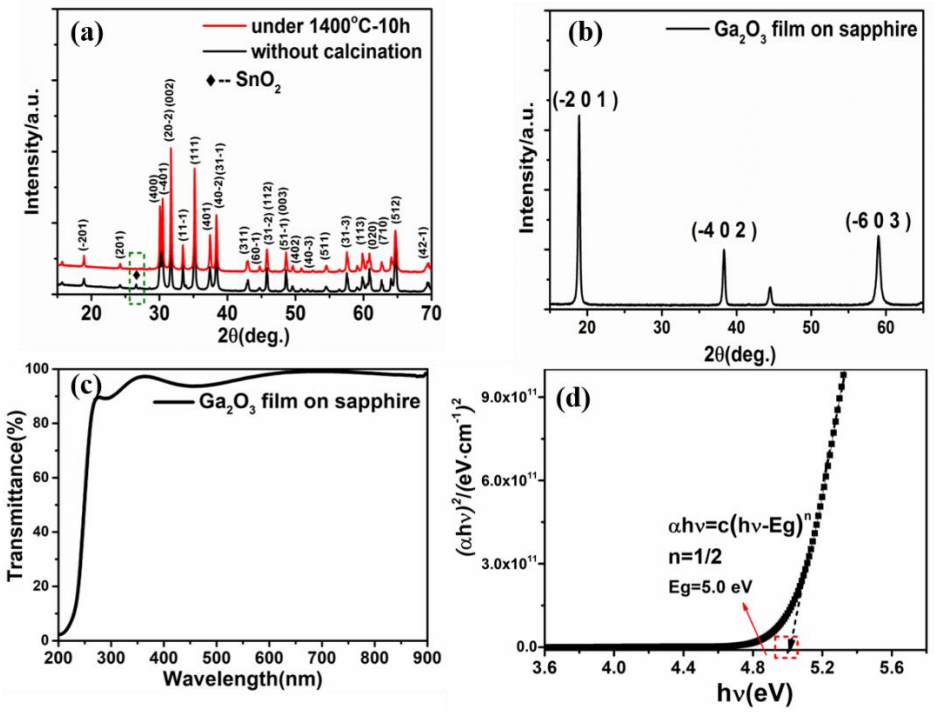

Figure 4.4 (a) XRD spectra of Ga_2O_3 powder doped by SnO_2; (b) XRD of Ga_2O_3 film on sapphire; (c) Transmittance spectrum of Ga_2O_3/sapphire; (d) Tauc plot of Ga_2O_3/sapphire. α represents the absorption coefficient of Ga_2O_3 deposited on sapphire.

To check whether the Sn^{4+} was fully diffused into the lattice of Ga_2O_3, the XRD of the mixed powder of Ga_2O_3 and SnO_2 was measured and shown in Figure 4.4a. After the calcination process under 1400 ^oC, the diffraction peak of SnO_2 disappeared shown in the red plot, demonstrating that the Sn^{4+} fully occupies the lattice position of Ga^{3+}. To obtain the Ga_2O_3 film with (-2 0 1) orientation owning the best conduction properties, sapphire (0 0 0 1) was applied as the substrate in the deposition.[6] According to Figure 4.4b, three sharp XRD diffraction peaks were observed for Ga_2O_3 film deposited on the sapphire, which was assigned to the monoclinic β-Ga_2O_3. It indicated that β-Ga_2O_3 film showed orientations similar to the single crystal structure under these deposition conditions. Figure 4.4c depicted the transmittance

measurement using UV-Vis, high transmittance (larger than 90%) in the wavelength range longer than 400 nm was obtained when Ga_2O_3 film was deposited on sapphire. Based on this transmittance, as a direct bandgap semiconductor (n=1/2), the optical Eg of Ga_2O_3 film was estimated to be 5.0 eV by the Tauc plot shown in Figure 4.4d, which was similar to the reference values.[7]

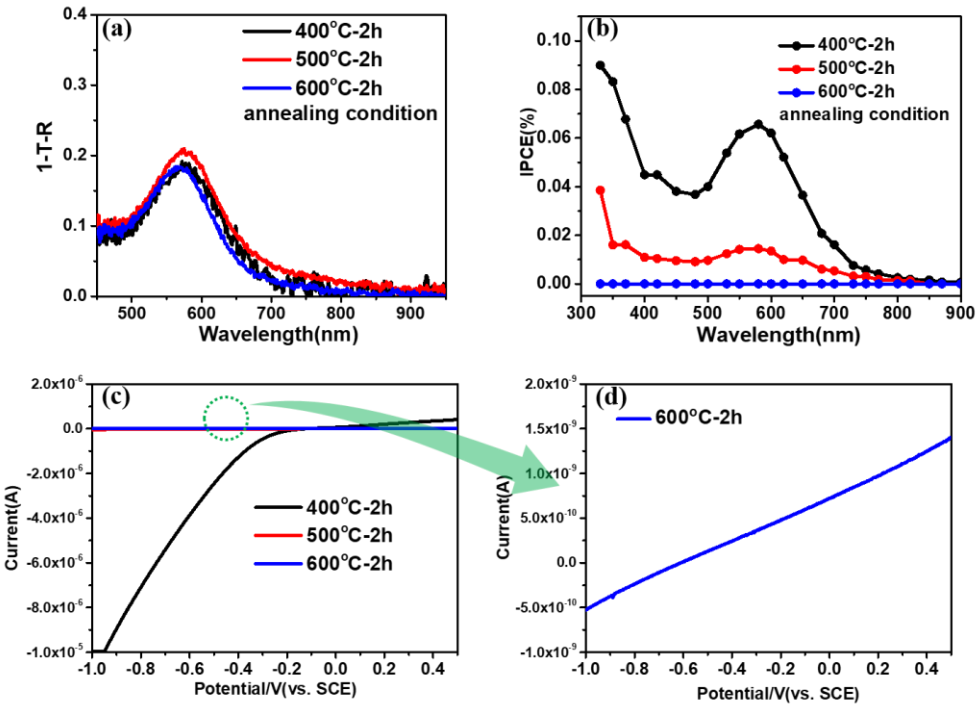

Figure 4.5 (a) Absorption spectra of Au-NPs/Ga_2O_3-film annealing under different temperature; (b) IPCE and (c) I-V spectra of Au-NPs/Ga_2O_3-film annealing under different temperature measured in 0.1 M $KClO_4$ solution; (d) I-V spectra of Au-NPs/Ga_2O_3-film annealing under 600 ^oC measured in 0.1 M $KClO_4$ solution.

In the case of Au-NPs/Ga_2O_3-film, the effect of annealing temperature on the PEC performance was investigated as shown in Figure 4.5. It could be found that all the Au-NPs loaded on Ga_2O_3-film owned similar absorption with a peak value of around 0.2 at 580 nm when the Au-NPs were obtained under different annealing temperatures.

However, the PEC conversion efficiency showed an obvious difference for these samples under different annealing temperatures. Under the annealing temperature of 400 ^{o}C, the Au-NPs/Ga_2O_3-film showed a peak IPCE of 0.07% at 600 nm measured in $KClO_4$ solution without the modification of TiO_2 layer. The IPCE has achieved the 70% of the IPCE measured using Au-NPs/SC-Ga_2O_3 (0.1% at 600 nm). I-V data of Au-NPs/Ga_2O_3-film under 400 ^{o}C in Figure 4.5c (black plot) also showed obvious semiconductor character. Both the IPCE and I-V results meant that the PLD-fabricated Ga_2O_3 thin film owned good electric properties.

However, with the increasing of annealing temperature to 500 ^{o}C or above, the IPCE of Au-NPs/Ga_2O_3-film dramatically dropped. When the annealing temperature reached 600 ^{o}C, the IPCE became zero even at a wavelength shorter than 400 nm which owns higher photon energy. A linear I-V of Au-NPs/Ga_2O_3-film under 600 ^{o}C was observed as shown in Figure 4.5d which meant very poor conductivity. It was reported that oxygen vacancies played an important role in determining the conductivity of Ga_2O_3-film during the deposition.[8] Too high oxygen concentration would suppress the carrier concentration during the deposition. Thus, the Ga_2O_3 film was deposited at a lower oxygen pressure under high temperatures. As a result, we speculated that, under a too high annealing temperature, the conductivity would probably be easily destroyed in the air atmosphere which owned very high oxygen concentration. As a result, Ga_2O_3-film only acted as a resistance under a high annealing temperature.

4.3.2 Positive effect of TiN layer on Ga_2O_3/Au-film

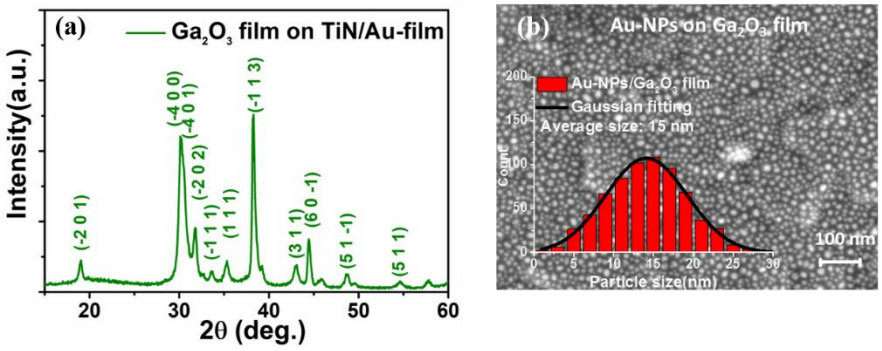

Figure 4.6 (a) XRD of Ga_2O_3 film deposited on TiN/Au-film; (b) Top-view SEM image of Au-NPs on Ga_2O_3 and the size analysis by Image J.

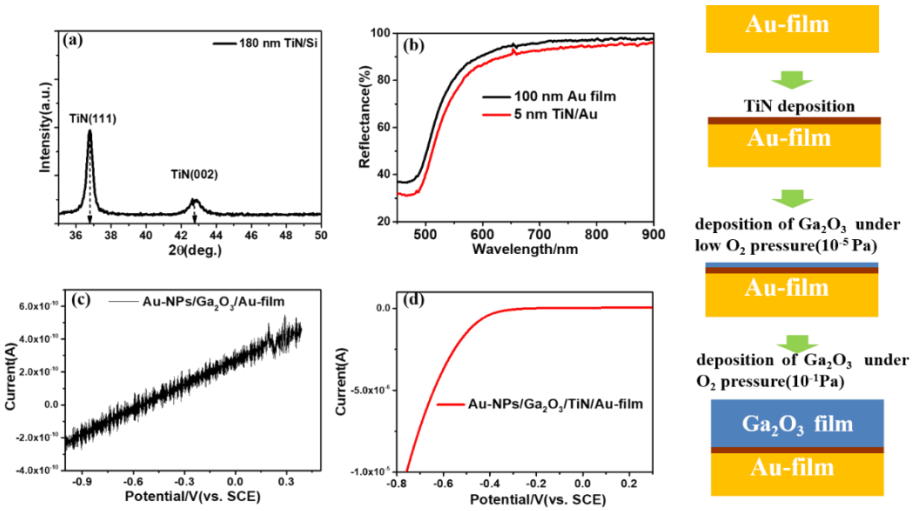

Figure 4.7 (a) XRD of TiN deposited on Si; (b) Reflectance spectra of Au film on SiO_2 with and without TiN film; (c) I-V curve of Au-NPs/Ga_2O_3/Au-film under dark conditions; (d) I-V curve of Au-NPs/Ga_2O_3/TiN/Au-film under dark conditions.

To construct the strong coupling between LSPR and nanocavity mode, Ga_2O_3-film was deposited on Au-film forming the nanocavity mode. However, when Ga_2O_3 was deposited directly on Au film, an undesired I-V relation was observed meaning poor semiconductor properties as shown in Figure 4.7c. In order to overcome the unstable deposition of Ga_2O_3 on Au-film, a method depositing a thin TiN layer on Au-film

before the deposition of Ga_2O_3-film under high deposition temperature was developed.

TiN was a kind of ceramic material owning high thermal stability and good electrical conductivity.[9-10] The diffraction peaks in the XRD result in Figure 4.7a were assigned to the TiN meaning that the TiN was synthesized through the multi-sputtering system using the metal Ti target and N_2 atmosphere under room temperature.[11] Moreover, the reflection of Au-film keeps as high as 85% after deposition of 5 nm-TiN, which is critical to be applied as a reflector to form a nanocavity. To prevent the thin TiN film from oxidation by an oxygen atmosphere under so high temperature, Ga_2O_3 film with 3000 pulses was first deposited on TiN under the vacuum degree of 10^{-5} Pa without the introducing of oxygen, as shown in Figure 4.7. Figure 4.6a showed the XRD results of Ga_2O_3-film deposited on the TiN/Au-film using the deposition conditions mentioned above. All the diffraction peaks were assigned to the β-Ga_2O_3 phase which was consistent with reference data.[6] As shown by the SEM image, the Au-NPs loaded on the Ga_2O_3-film by annealing Au film deposited by electron-beam evaporation under 400 ^oC showed a uniform distribution with an average diameter of 15 nm. The deviation of the size statistics of Au-NPs was calculated to be 4.9 nm. It could be found that I-V curve of Au-NPs/Ga_2O_3/TiN/Au-film (AGA) measured under dark conditions showing an obvious semiconductor character in Figure 4.7d was obtained after the addition of TiN between Ga_2O_3-film and Au-film.

4.3.3 Optical properties and PEC performance of TAGA under strong coupling conditions

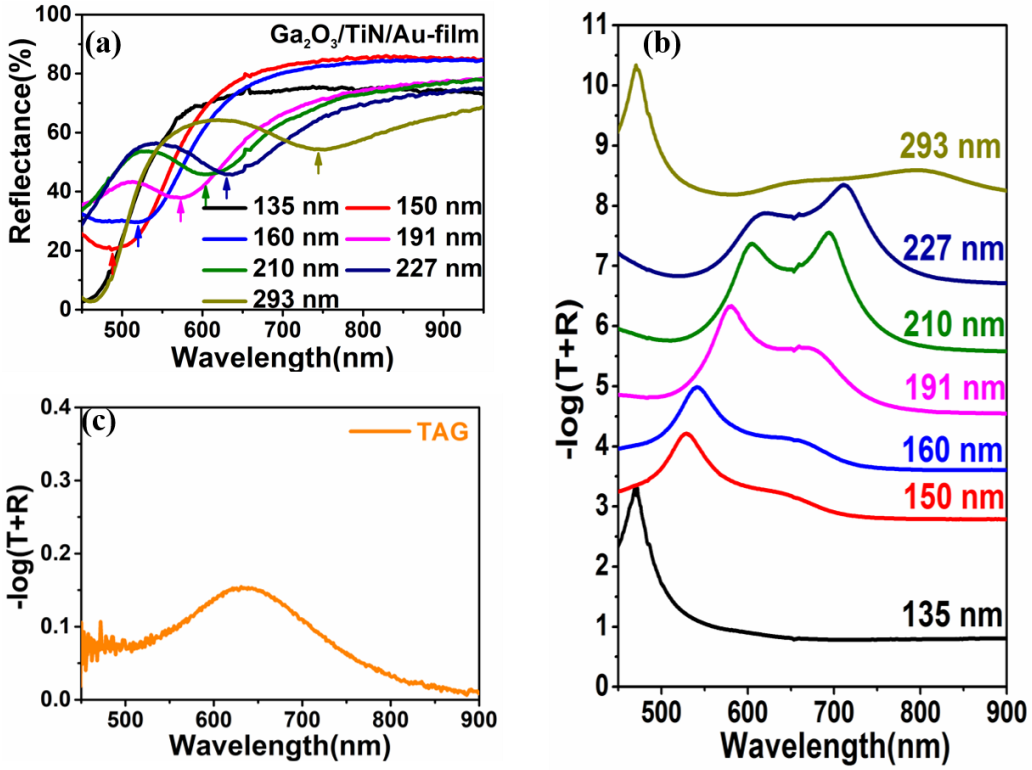

Figure 4.8 (a) Reflectance spectra of Ga_2O_3 on TiN/Au-film; (b) Absorption spectra of TAGA structure.; (c) Absorption of TiO_2/Au-NPs/Ga_2O_3 (210 nm)/sapphire. The thickness of TiO_2 in TAGA was 4 nm.

Based on the positive effect of TiN on the electrochemical properties of Ga_2O_3, different thicknesses of Ga_2O_3 film were deposited on the Au-film to adjust the cavity resonance wavelength. After the deposition of Ga_2O_3 film on the Au-film, an obvious cavity mode was observed in Figure 4.8a. The cavity resonance wavelength shifted from 450 nm to 740 nm when the thickness of Ga_2O_3 was increased from 135 nm to 293 nm. The absorption spectra of TAGA calculated by -log (T+R) with various thickness of Ga_2O_3 film was shown in Figure 4.8b, where T and R represented the transmittance and reflectance, respectively. It could be found that dual bands were not observed, only one absorption peak at 470 nm appeared when the thickness of Ga_2O_3 was 135 nm. That is because the cavity resonance wavelength was far away from the

LSPR band of Au-NPs on Ga_2O_3 film at around 635 nm as shown by the orange line in Figure 4.8c when the Ga_2O_3 film was deposited on the sapphire. With the thickness increasing from 150 nm, the cavity resonance wavelength began to shift close to the LSPR wavelength, two absorption peaks gradually appeared in Figure 4.8b. The tuning condition was formed when the thickness of Ga_2O_3 was around 210 nm with two distinct absorption peaks. When the thickness was further increased to 293 nm, the dual absorption bands disappeared gradually. Because of the similar refractive index between Ga_2O_3 (n=1.90) and sapphire (n=1.77),[12] no cavity and coupling was formed in TiO_2/Au-NPs/Ga_2O_3/sapphire (TAG) without Au-film in which the light absorption only originated from LSPR of single layer Au-NPs. Therefore, the visible light absorption of the TAGA sample was much higher than the TAG without coupling.

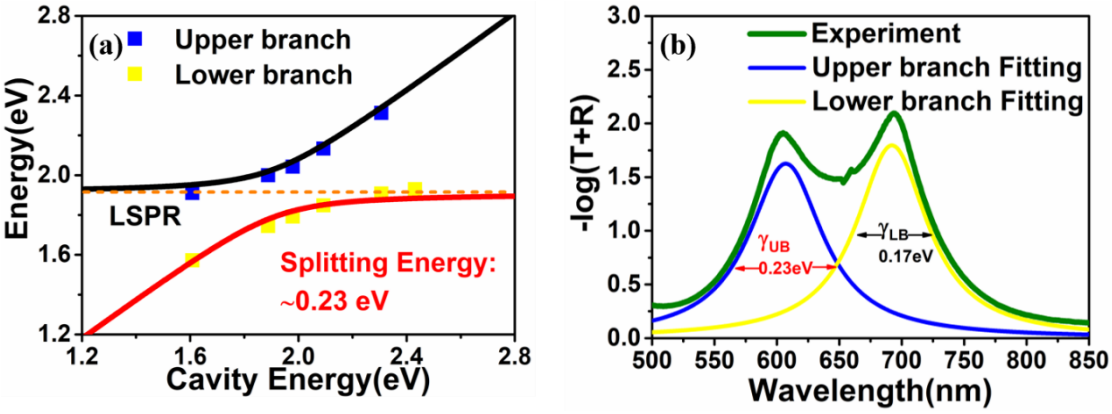

Figure 4.9 (a) Dispersion curve of TAGA; (b) Spectral separation of the absorption spectrum of TAGA with tuning structure by a Lorentz fitting.

To confirm whether this energy splitting of TAGA structure is a strong coupling, the dispersion curve of TAGA structure was shown in Figure 4.9a. The black and red lines were the fittings using a coupled harmonic oscillator model.[2] Lorentzian fittings were applied to calculate the peak energy of separated dual bands for TAGA structure

represented by blue (upper branch) and yellow (lower branch) squares in Figure 4.9a. According to the dispersion curve, the splitting energy of TAGA was 0.23 eV. For a strong coupling system, it should fulfill the following criterion:

$$\hbar\Omega > \sqrt{({\gamma_{UB}}^2 + {\gamma_{LB}}^2)/2}$$

Where, $\hbar\Omega$ is the splitting energy, γ_{UB} and γ_{LB} are the full widths at half maximum (FWHM) of the upper and lower branches, respectively.[13] The FWHM of upper and lower branches for TAGA sample under tuning condition separated by the Lorentzian fitting was 0.23 and 0.17 eV shown in Figure 4.9b, respectively. Therefore, the splitting energy was larger than the value of 0.20 eV calculated by the right side formula using γ_{UB} and γ_{LB}, indicating that the energy level splitting formed in TAGA fulfilled the strong coupling criterion.

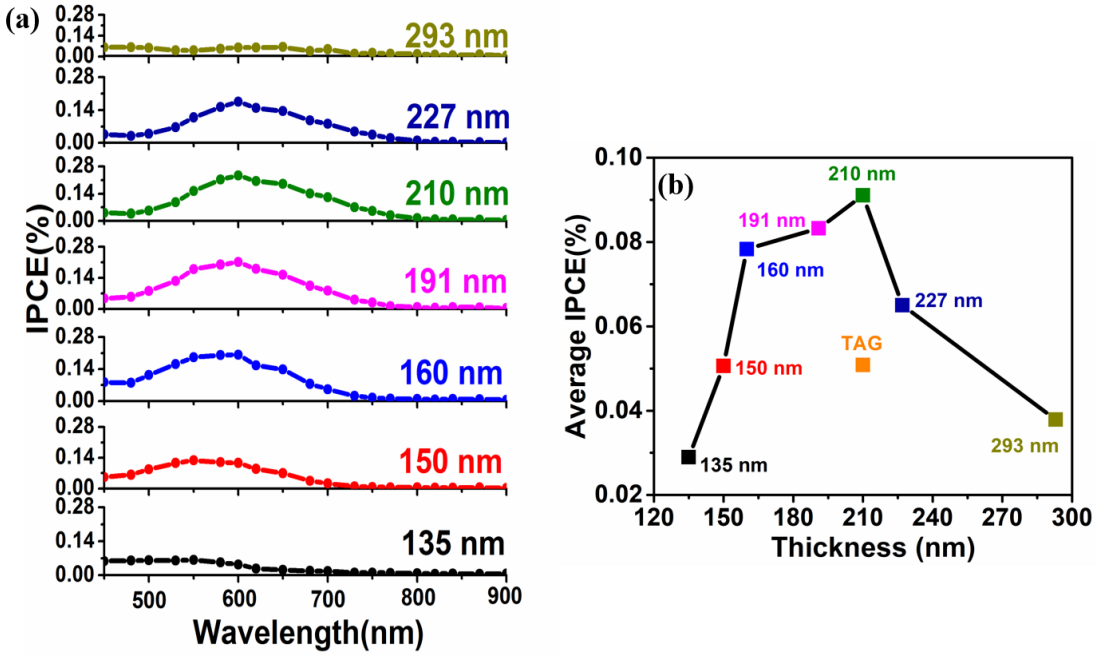

Figure 4.10 (a) IPCE spectra and (b) average IPCE of TAGA measured in 0.1M KOH solution.

The photocurrent was measured by a typical three-electrode electrochemical system

in a 0.1M KOH aqueous solution. The IPCE of TAGA samples with different Ga_2O_3 thickness was shown in Figure 4.10. It was found that average IPCE showed obvious enhancement when the cavity wavelength was close to the LSPR position. When the thickness was 210 nm, peak IPCE reached the maximum value of 0.24%.

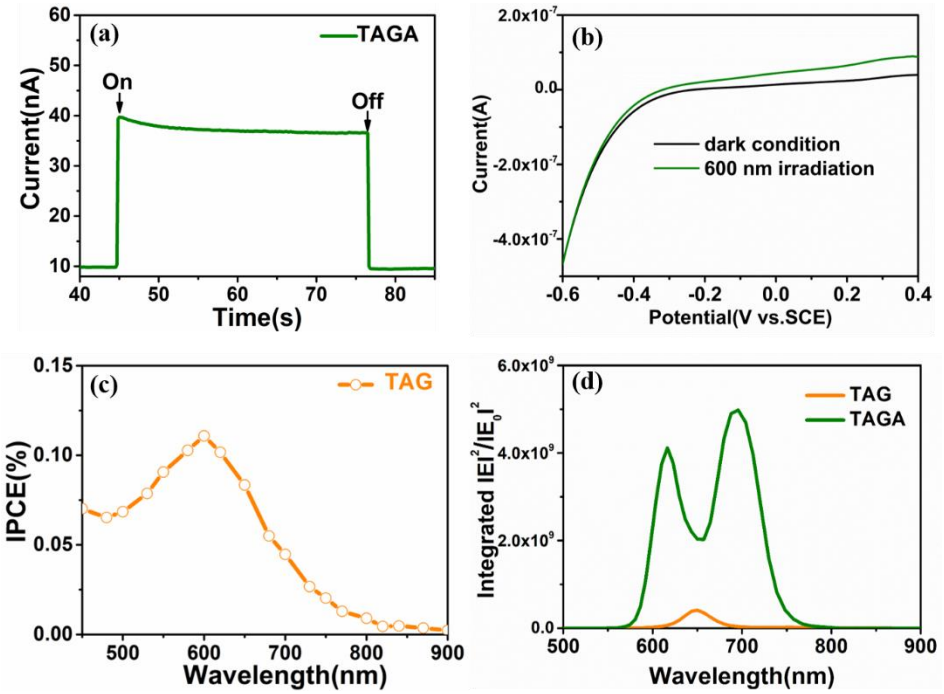

Figure 4.11 (a) I-t curve of TAGA under 600 nm irradiation, bias potential was applied as + 0.3 V vs SCE; (b) I-V curve of TAGA samples measured in 0.1M KOH solution under dark condition and 600 nm irradiation; (c) IPCE of TAG measured in 0.1 M KOH solution; (d) FDTD simulation of near-field spectra at the interface of Au-NPs/Ga_2O_3 in TAGA (green) and TAG (purple). The monitor position (black line) is 1 nm above the interface of Au-NPs/Ga_2O_3 shown in the schematic.

At the IPCE peak wavelength of 600 nm, the stable photocurrent of TAGA at tuning condition was 27 nA in Figure 4.11a which was consistent with the I-V results measured under dark and 600 nm irradiation shown in Figure 4.11b. To investigate the effect of strong coupling on the photocurrent generation as well as the electrons

injection, the IPCE of TAG sample that 210 nm Ga_2O_3 was also deposited on sapphire instead of TiN/Au-film are also calculated shown in Figure 4.11c. This IPCE of TAGA sample showed 2.4-fold larger than that of TAG without strong coupling, demonstrating that the light absorption of Au-NPs as well as the electrons injection significantly increased by strong coupling. According to FDTD simulation in Figure 4.11d, the near-filed intensity at the interface of Au-NPs/Ga_2O_3 in TAGA was dramatically increased compared with that of TAG which might contribute to the efficiently improved IPCE.[14] The lower IPCE enhancement than the absorption enhancement between TAGA and TAG is attributed to the difference on the crystallinity between Ga_2O_3 film deposited on TiN/Au-film and sapphire (see Figure 4.4b and Figure 4.6a). The Ga_2O_3 film deposited on sapphire showed an (-2 0 1) orientation similar to the SC-Ga_2O_3 which owns a good carriers transportation. However, The Ga_2O_3 film deposited on TiN/Au-film showed a poly-crystal structure meaning many grain boundaries in the crystal Ga_2O_3 film. These boundaries would have negative effect on the carrier transportation. As a result, The IPCE enhancement of TAGA compared with TAG is not as high as the absorption enhancement.

It could be found that the peak IPCE of TAGA with the application of strong coupling showed an enhancement compared with TiO_2/Au-NPs/SC-Ga_2O_3 with a peak IPCE of 0.17% as shown in chapter 3. TAGA owned superior performance in light absorption and photoelectric conversion efficiency than SC-Ga_2O_3 based sample, while the deposition of Ga_2O_3 film was relatively low cost compared with the application of SC-Ga_2O_3.

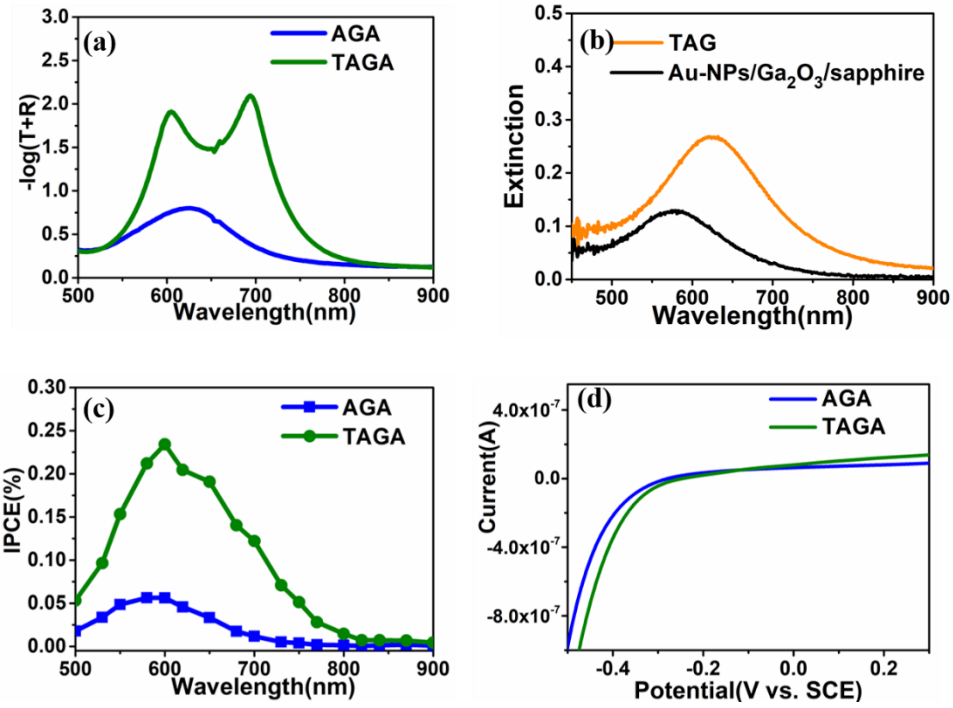

Figure 4.12 (a) Absorption spectra of TAGA and AGA; (b) Extinction spectra of Au-NPs/ Ga_2O_3/sapphire with and without 4-nm TiO_2; (c) IPCE of TAGA and AGA measured in 0.1M KOH solution; (d) I-V curve of TAGA and AGA measured in 0.1M KOH solution under dark condition.

In this study, the role of TiO_2 layer partially inlaying Au-NPs was also studied. Dual-band of absorption spectra did not occur after the load of Au-NPs for AGA samples with 210 nm Ga_2O_3 in Figure 4.12a, indicating that coupling condition was not formed. While Au-NPs were inlaid by 4 nm TiO_2 using ALD, two absorption peaks were observed and the absorption was efficiently increased in the visible region. This was attributed to the enhanced LSPR mode of Au-NPs after the deposition of TiO_2 layer shown in Figure 4.12b, resulting in the increased coupling strength. Furthermore, a better spatial overlap between cavity and LSPR mode could be obtained by the TiO_2 inlaying Au-NPs as illustrated in our previous study.[2] For TAGA structure, the IPCE peak after the deposition of TiO_2 was 4.2 times larger than that of

the AGA without TiO_2 as presented in Figure 4.12c. It is found that there is only one obvious peak in the IPCE spectra of TAGA, which was not consistent with the absorption spectra. An obvious IPCE peak of TAGA was located at 600 nm which is the same as absorption peak of upper branch. The electron excited by the short wavelength owns high energy would be efficiently injected into the conduction band of Ga_2O_3. A small peak at around 700 nm could also be found although it is not such high as the peak at 600 nm. According to the Marcus theory on electrons transfer, the electrons excited by longer wavelength owns lower energy, so the rate of these lower energy electron injection to the conduction band is smaller compared with electrons excited by shorter wavelength. Therefore, the IPCE peak at around 700 nm was not so strong. It should be noted that the CB potential of TiO_2 is more positive than Ga_2O_3, the deposition of TiO_2 probably influence the CB potential of Ga_2O_3. According to the I-V results in Figure 4.12d, the onset potential of TAGA only showed a slight shifting towards positive potential as compared with AGA. It demonstrated that after the 4-nm TiO_2 layer partially inlaid Au-NPs, the Ga_2O_3 in TAGA still kept a high reduction ability.

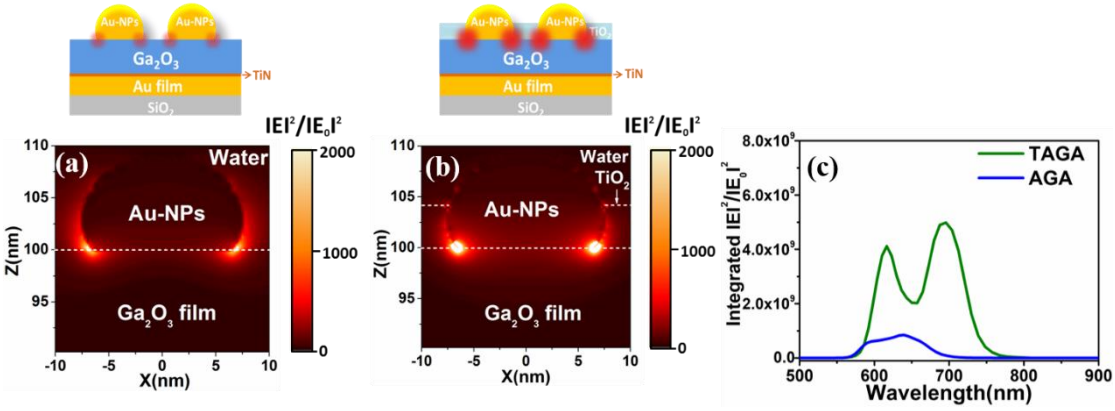

Figure 4.13 (a) Near-field distribution at 600 nm irradiation in (a) AGA and (b) TAGA (right) calculated by FDTD; (c) Near-field spectra at the interface of Au-NPs/Ga_2O_3 in TAGA and AGA calculated by FDTD.

As discussed above, TAGA at the tuning condition showed much higher near-field intensity compared with TAG. We also calculated the near-field distribution and intensity in TAGA and AGA by FDTD as depicted in Figure 4.13. It could be found that two bright spots were located at the interface of Au-NPs/Ga_2O_3 which were assigned to the near-field enhancement induced by LSPR. After the Au-NPs were inlaid by TiO_2, near-field at the interface of Au-NPs/Ga_2O_3 in TAGA showed a higher-intensity at the coupling condition compared with the AGA structure at the wavelength of 600 nm. Furthermore, a much higher integrated intensity of near-field enhancement at the interface of Au-NPs/Ga_2O_3 in TAGA was observed than AGA without TiO_2 shown in Figure 4.13c, leading to efficient electrons injection to the CB of Ga_2O_3. It should be noted that the near-field enhancements at the interface of Au-NPs/Ga_2O_3 in TAG are not as high as those in AGA (see Figure 4.11d and Figure 4.13c, the larger IPCE in TAG could be attributed to the good hole-trapping ability of the TiO_2 layer, which suppresses electron/hole recombination and promotes charge separation.[1]

Therefore, the TiO_2 layer partially inlaying Au-NPs played an important role in increasing the coupling strength between cavity mode and LSPR mode, as well as the charge separation so that the absorption and IPCE were dramatically improved without too much change in the negative CB potential of Ga_2O_3.

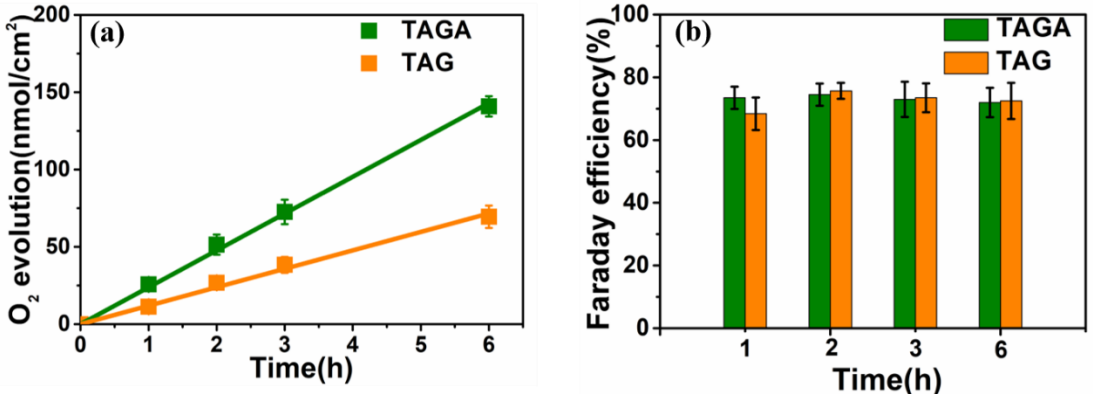

Figure 4.14 (a) O_2 evolution amount and (b) Faraday efficiency using TAGA and TAG photoanode illuminated by visible light (λ>450nm, 130 mW/cm^2) under zero bias potential. The lines are the linear fittings.

We performed the water splitting under visible light irradiation (λ>450nm) using TAGA measured in a two-electrode system. The generated gas was collected and then detected by gas chromatography-mass spectrometry as shown in Figure 4.14. It was found that O_2 evolved from the water oxidation was observed even when zero bias potential was applied between Pt electrode and TAGA photoanode. A linear relationship between the amount of O_2 and the reaction time was observed in O_2 evolution with an evolution rate of 23.9 nmol·h^{-1}·cm^{-2} depicted in Figure 4.14a. The average faraday efficiency of O_2 evolution using TAGA under different reaction time kept stable at around 76% as shown in Figure 4.14b. As no sacrificial electron donor or acceptor was used during the measurement, self-oxidation of the photoanode and side reaction was not found, the relatively low faraday efficiency of 76% probably results from the technical difficulty to collect all evolved O_2. Water splitting using TAG samples was also investigated at the same measurement conditions as TAGA. Similar faraday efficiency of O_2 evolution on TAG was observed shown in Figure 4.14b. However, under no coupling condition using TAG, the evolution rate (11.9 nmol·h^{-1}·cm^{-2}) was only half of that of TAGA. External potentials were always

applied in PEC reactions to further drive the related reduction reaction, such as in water splitting while the CB potential of semiconductors was insufficient.[15] In this case, the water splitting on TAGA at zero bias potential could be explained that the negative CB potential of Ga_2O_3 positively affects the reduction reaction on the cathode, resulting in the improvement of the whole water splitting reaction.[16] By advantage of the intrinsically negative CB potential, hot electrons injected into the CB of Ga_2O_3 and holes captured by the TiO_2 could take part in the redox reaction for the generation of H_2 and O_2 at zero bias potential.

4.4 Conclusion

In this study, a novel thin-film photoanode of TiO_2/Au-NPs/Ga_2O_3/TiN/Au-film with negative CB potential was developed towards zero bias water splitting under visible irradiation. The deposition of TiN between Ga_2O_3 and Au-film successfully improved the I-V character under high deposition temperature. Strong coupling was achieved when the cavity resonance wavelength of Ga_2O_3 on TiN/Au-film overlapped with the LSPR of Au-NPs partially inlaid by a thin TiO_2 layer. Both the visible light absorption and electron injection from Au-NPs to Ga_2O_3 were successfully enhanced by applying the strong coupling into the Ga_2O_3 system which is intrinsically visible light inactive. And the photoelectric conversion efficiency under strong coupling was obviously enhanced compared with that using SC-Ga_2O_3. Based on the advantage of the negative CB potential of Ga_2O_3, water splitting was successfully detected at zero bias potential. This result demonstrates that the Ga_2O_3 exhibits a huge prospect in relieving the global environmental problem, especially CO_2 reduction, based on its negative CB potential.

4.5 Reference

1. Maeda, K., Photocatalytic Water Splitting Using Semiconductor Particles: History and Recent Developments. Journal of Photochemistry and Photobiology C: Photochemistry Reviews **2011**, 12, 237-268.

2. Ran, J.; Jaroniec, M.; Qiao, S. Z., Cocatalysts in Semiconductor-Based Photocatalytic CO_2 Reduction: Achievements, Challenges, and Opportunities. Adv Mater **2018**, 30, 1704649.

3. Chen, S.; Liu, D.; Peng, T., Fundamentals and Recent Progress of Photocatalytic Nitrogen−Fixation Reaction over Semiconductors. Solar RRL **2020**, 5, 2000487.

4. Ge, M.; Li, Q.; Cao, C.; Huang, J.; Li, S.; Zhang, S.; Chen, Z.; Zhang, K.; Al-Deyab, S. S.; Lai, Y., One-Dimensional TiO_2 Nanotube Photocatalysts for Solar Water Splitting. Adv Sci **2017**, 4, 1600152.

5. Tao, R.; Li, X.; Li, X.; Shao, C.; Liu, Y., TiO_2/$SrTiO_3$/g-C_3N_4 Ternary Heterojunction Nanofibers: Gradient Energy Band, Cascade Charge Transfer, Enhanced Photocatalytic Hydrogen Evolution, and Nitrogen Fixation. Nanoscale **2020**, 12, 8320-8329.

6. Yang, Y.; Niu, S.; Han, D.; Liu, T.; Wang, G.; Li, Y., Progress in Developing Metal Oxide Nanomaterials for Photoelectrochemical Water Splitting. Advanced Energy Materials **2017**, 7, 1700555.

7. Choudhary, S.; Solanki, A.; Upadhyay, S.; Singh, N.; Satsangi, V. R.; Shrivastav, R.; Dass, S., Nanostructured CuO/$SrTiO_3$ Bilayered Thin Films for Photoelectrochemical Water Splitting. Journal of Solid State Electrochemistry **2013**, 17, 2531-2538.

8. Corma, A.; Garcia, H., Photocatalytic Reduction of CO_2 for Fuel Production: Possibilities and Challenges. Journal of Catalysis **2013**, 308, 168-175.

9. Akatsuka, M.; Kawaguchi, Y.; Itoh, R.; Ozawa, A.; Yamamoto, M.; Tanabe, T.;

Yoshida, T., Preparation of Ga_2O_3 Photocatalyst Highly Active for CO_2 Reduction with Water without Cocatalyst. Applied Catalysis B: Environmental **2020**, 262, 118247.

10. Oshima, T.; Kaminaga, K.; Mashiko, H.; Mukai, A.; Sasaki, K.; Masui, T.; Kuramata, A.; Yamakoshi, S.; Ohtomo, A., β-Ga_2O_3 single Crystal as a Photoelectrode for Water Splitting. Japanese Journal of Applied Physics **2013**, 52, 111102.

1. Wang, Y.; Shi, X.; Oshikiri, T.; Zu, S.; Ueno, K.; Misawa, H., Plasmon-Induced Electron Injection into the Large Negative Potential Conduction Band of Ga_2O_3 for Coupling with Water Oxidation. Nanoscale **2020**, 12, 22674-22679.

2. Shi, X.; Ueno, K.; Oshikiri, T.; Sun, Q.; Sasaki, K.; Misawa, H., Enhanced Water Splitting under Modal Strong Coupling Conditions. Nat Nanotechnol **2018**, 13, 953-958.

3. Matsuzaki, K.; Hiramatsu, H.; Nomura, K.; Yanagi, H.; Kamiya, T.; Hirano, M.; Hosono, H., Growth, Structure and Carrier Transport Properties of Ga_2O_3 Epitaxial Film Examined for Transparent Field-Effect Transistor. Thin Solid Films **2006**, 496, 37-41.

4. Smirnov, Y., Scalable Pulsed Laser Deposition of Transparent Rear Electrode for Perovskite Solar Cells. Advanced Materials Technologies **2021**, 6, 2000856.

5. Orita, M.; Ohta, H.; Hirano, M.; Hosono, H., Deep-Ultraviolet Transparent Conductive Ga_2O_3Thin Films. Applied Physics Letters **2000**, 77, 4166-4168.

6. Goyal, A.; Yadav, B. S.; Thakur, O. P.; Kapoor, A. K.; Muralidharan, R., Effect of Annealing on β-Ga_2O_3 Film Grown by Pulsed Laser Deposition Technique. Journal of Alloys and Compounds **2014**, 583, 214-219.

7. Oshima, T.; Kaminaga, K.; Mashiko, H.; Mukai, A.; Sasaki, K.; Masui, T.; Kuramata, A.; Yamakoshi, S.; Ohtomo, A., β-Ga_2O_3 single Crystal as a Photoelectrode for Water Splitting. Japanese Journal of Applied Physics **2013**, 52, 111102.

8. Yang, C.-C.; Huang, J.-Q.; Chen, K.-Y.; Chiu, P.-H.; Vu, H.-T.; Su, Y.-K., Effect of Oxygen Concentration Ratio on a Ga2o3-Based Resistive Random Access Memory. IEEE Access **2019**, 7, 175186-175191.

9. Hultman, L., Thermal Stability of Nitride Thin Films. Vacuum **2000**, 57, 1-30.

10. Steinmüller-Nethl, D.; Kovacs, R.; Gornik, E.; Rödhammer, P., Excitation of Surface Plasmons on Titanium Nitride Films: Determination of the Dielectric Function. Thin Solid Films **1994**, 237, 277-281.

11. Tang, S.; Cheng, Q.; Zhao, J.; Liang, J.; Liu, C.; Lan, Q.; Cao, Y.-C.; Liu, J., Preparation of Titanium Nitride Nanomaterials for Electrode and Application in Energy Storage. Results in Physics **2017**, 7, 1198-1201.

12. Qu, Y.; Kim, J.; Coburn, C.; Forrest, S. R., Efficient, Nonintrusive Outcoupling in Organic Light Emitting Devices Using Embedded Microlens Arrays. ACS Photonics **2018**, 5, 2453-2458.

13. Oshikiri, T.; Jo, H.; Shi, X.; Misawa, H., Boosting Hydrogen Evolution at Visible Light Wavelengths by Using a Photocathode with Modal Strong Coupling between Plasmons and a Fabry-Perot Nanocavity. Chemistry **2022**, 28, e202200288.

14. Suganami, Y.; Oshikiri, T.; Shi, X.; Misawa, H., Water Oxidation under Modal Ultrastrong Coupling Conditions Using Gold/Silver Alloy Nanoparticles and Fabry-Perot Nanocavities. Angew Chem Int Ed Engl **2021**, 60, 18438-18442.

15. Larson, S.; Zhao, Y., Tuning the Composition of Bi_xW_yO Nanorods Towards Zero Bias Pec Water Splitting. Nanotechnology **2016**, 27, 255401.

16. Fudo, E.; Tanaka, A.; Kominami, H., Effect of Conduction Band Potential on Cocatalyst-Free Plasmonic H_2 Evolution over Au Loaded on Sr^{2+}-Doped CeO_2. Catalysis Science & Technology **2019**, 9, 3047-3054.

Chapter 5

Conclusion and Future Prospect

5.1 Conclusion

In this thesis, we mainly focused on the photocurrent generation and water splitting in the visible region using wide bandgap semiconductor Ga_2O_3 with negative CB potential that is beneficial to reducing the water, or even CO_2. Based on the LSPR effect, the load of Au-NPs on the surface of Ga_2O_3 by annealing Au film successfully overcame the intrinsically inactive to visible light due to its large bandgap. Next, the interfacial modification in Au-NPs/SC-Ga_2O_3 by a TiO_2 layer which owns an excellent holes-trapping ability to improve the charges separation was investigated further enhancing the IPCE of Au-NPs/SC-Ga_2O_3. In order to resolve the poor light absorption of a single Au-NPs layer, modal strong coupling was introduced into the Au-NPs/Ga_2O_3-film system. Strong coupling was formed when the cavity resonance wavelength and LSPR wavelength matched each other, efficiently increasing the light absorption and IPCE in visible region. Finally, water splitting at zero bias potential was achieved based on the intrinsic negative CB potential of Ga_2O_3.

To confirm the most appropriate size of Au-NPs on SC-Ga_2O_3, series size of Au-NPs were loaded on SC-Ga_2O_3. After the load of Au-NPs with different size, obvious absorption, as well as the photocurrent generation was observed in visible region. 15-nm Au-NPs loaded SC-Ga_2O_3 showed the highest peak IPCE at 580 nm due to high LSPR intensity and long dephasing time.

In order to improve the charges separation at the interface of Au-NPs/SC-Ga_2O_3, an interfacial modification was applied based on the hole-trapping ability of TiO_2. The deposition of TiO_2 at the interface of Au-NPs/Ga_2O_3 would damage the electrons

transfer from Au-NPs to Ga_2O_3. The deposition of TiO_2 layer partially inlaying Au-NPs without destroying the contact between Au-NPs and Ga_2O_3 was a much better structure for the charges transfer. In this structure, the hot electrons would be smoothly injected into the CB of Ga_2O_3, while holes remained in the Au-NPs were trapped by TiO_2, so that the IPEC was further enhanced. This modification showed an obvious dependence on the thickness of TiO_2. Thicker TiO_2 would do harm to the generation and migration of the hot electron at the interface of Au-NPs/Ga_2O_3, having a negative effect on the IPCE improvement.

The plasmon induced photocurrent generation based on the low-cost Ga_2O_3 thin film deposited by PLD was further investigated. After the optimization of deposition conditions, the Ga_2O_3 thin film on sapphire with good electric properties was obtained. The IPCE of Au-NPs loaded Ga_2O_3 film was comparable with that using SC-Ga_2O_3.

Based on the fabrication of Ga_2O_3 thin film by PLD, strong coupling between LSPR and cavity mode was employed to increase the light absorption of Au-NPs and electrons injection. Before the deposition of Ga_2O_3 film on Au film to form nanocavity mode, a thin TiN layer was deposited on Au film before the deposition of Ga_2O_3 film to obtain the required I-V properties. The cavity mode with tunable resonance wavelength was formed in Ga_2O_3/TiN/Au-film with different thickness of Ga_2O_3. Strong coupling was achieved when the cavity resonance wavelength and LSPR wavelength of Au-NPs overlapped. Under the strong coupling conditions, light absorption and near field intensity, as well as IPCE was efficiently increased compared with that without coupling effect. TiO_2 inlaying Au-NPs played a critical role in increasing coupling strength and holes trapping. By advantage of the negative CB of Ga_2O_3, water splitting at zero bias potential was successfully achieved using TAGA under visible irradiation.

As a summary, in this thesis, we demonstrated the photocurrent generation and water splitting using Ga_2O_3 based photoanode with negative CB potential under the visible irradiation. The load of Au-NPs could efficiently achieve light absorption and photocurrent generation on wide bandgap Ga_2O_3 in the visible region. It was also demonstrated that the excellent holes-trapping ability of TiO_2 layer could further increase the charges separation through the interfacial modification on Au-NPs/Ga_2O_3 by partially inlaying Au-NPs by TiO_2. The strong coupling between the LSPR mode and nanocavity mode was an efficient strategy to increase the light absorption and electrons injection. Moreover, the zero bias potential water splitting was achieved based on the negative CB potential of Ga_2O_3.

5.2 Future Prospect

Based on results obtained in the present research, the light absorption and photocurrent generation in visible region has been achieved on wide bandgap semiconductor Ga_2O_3 relying on the LSPR effect of Au-NPs. Furthermore, water splitting at zero bias potential was observed over Ga_2O_3 based photoanode in visible region due to the negative CB potential of Ga_2O_3. According to the principles in PEC reactions, the negative CB potential is beneficial to the reduction reaction, especially the substances that require a negative reduction potential, such as CO_2. As a result, it is expected to achieve CO_2 reduction, even at zero bias potential using the Ga_2O_3 based photoanode under visible irradiation. In addition, the Schottky barrier at the interface of metallic-NPs and semiconductors is also another factor that should be considered in the carrier separation and injection. It is found that the Schottky junction barrier between Ga_2O_3 and Au-NPs is very high due to the large work function of Au and negative CB potential of Ga_2O_3. The IPCE is expected to be further enhanced when the Schottky junction barrier is reduced moderately so that photons with lower energy could be injected into the CB of Ga_2O_3. Furthermore, in a strong coupling system, splitting energy also plays an important role in the PEC performance. The quantum efficiency probably will be increased with larger spitting energy so that the IPCE is enhanced.

According to the views mentioned above, the future work is shown as below:

(1) The reaction cell will be designed with a suitable structure for CO_2 reduction. Also, the electrolyte and electrode should be investigated for the best selectivity during the CO_2 reduction process.

(2) It is expected that Al nanoparticles (Al-NPs) could be loaded on the Ga_2O_3

reducing the barrier height due to its low work function compared with Au. As Al is easily oxidized to Al_2O_3, solution method might be a good approach to load Al-NPs on Ga_2O_3 instead of annealing thin Al film.

(3) To control the LSPR properties, alloy metal NPs (such as Au-Ag, Au-Al) will be loaded on the surface of Ga_2O_3 film instead of the Au-NPs. Before the annealing process for the formation of alloy NPs, stack layers with different kind of metal are deposited on the surface of Ga_2O_3 film. The thickness ratio of these metal layers and annealing conditions shall be investigated to optimize the composition.

Publication List

1. Y. Wang, X. Shi, T. Oshikiri, S. Zu, K. Ueno, H. Misawa,

"Plasmon-induced electron injection into the large negative potential conduction band of Ga_2O_3 for coupling with water oxidation"

Nanoscale, **2020**, 12, 22674-22679.

2. Y. Wang, X. Shi, T. Oshikiri, H. Misawa,

"Improved water splitting efficiency of Au-NP-loaded Ga_2O_3 thin films in the visible region under strong coupling conditions"

Nanoscale Advances, **2023**, 5, 119-123.